Study of $\overline{K}$ - meson production in 6 Gev / c $K^{-}P$ interactions

by

Pratipkumar Chaudhuri

A Thesis presented for the degree of Doctor of Philosophy of the University of London

Department of Physics
Imperial College
London S.W.7

February 1967

ABSTRACT

This thesis is based on the results of a study of strange mesonic systems in a 6 Gev K^-P experiment with a liquid hydrogen bubble chamber. It includes a general introduction (chapter 1) and brief descriptions of the instrumentation (ch.2), data-processing (ch.3) and the theoretical background (ch.5) together with a discussion on the sources of systematic and random errors encountered (ch.4). The analysis of the data on some 2, 3 and 4 body final states involving a $\bar{K}$ meson is presented (chs. 6 & 7) and the conclusions from this and other similar experiments discussed (ch.8).

CONTENTS

PREFACE

The author joined the bubble chamber film analysis group at Imperial College in autumn 1963. He assisted the 4 Gev π^+P and the 3.5 Gev K^-P experiments then in progress at I.C. till summer '64 when the 6 Gev K^-P experiment was started. Then onwards he took part in the data-processing and the general analysis in this experiment and was, in particular, responsible for the analysis of final states involving a $\overline{K}$ meson, the results of which are presented in this thesis.

Chapter 1 Introduction

A K^-P experiment in a bubble chamber is, in general, a multipurpose one. A greater variety of interactions can be produced in a K^-N collision than in a πN or K^+N collision since the initial state has strangeness -1 and baryon no. 1. Thus, even apart from producing $\bar{K}$ mesons in the final state, it can produce baryons of negative strangeness in profusion, no associated production of other strange particles being necessary.

A great stimulus has been derived towards high energy K^-P experiments from the study of systematics of elementary particles with the help of group - theory. By 1962 the existence of a baryon, named Ω^-, of strangeness -3 and mass ~ 1.676 Gev had been predicted,[1] which could fill up the last vacancy in the $J^P = 3/2^+$ SU3 decuplet for baryons. Of all particles available as a beam for experiments, the K^- is most suitable for the production of this particle since the no. of strangeness +1 mesons to be created in association would be minimum. The Ω^- was looked for in a 3.5 Gev K^-P experiment by a British collaboration, the centre-of-mass energy being just sufficient to produce the Ω^- in the reaction $K^-P \rightarrow \Omega^-K^+K^o$. No such event was identified[2]. The next step was to try a higher energy and the outcome was the 6 Gev K^-P experiment.

No less important, however, is the study of various production mechanisms at high energy. The peripheral nature of high - energy

collisions - i.e. the tendency towards small four-momentum transfers to the final state particles with respect to the incoming particles in the centre of mass system - has been observed in various other experiments. It is normally explained as an one meson exchange process though baryons are included in special circumstances. It is of constant interest to study these processes at high energies. Added to this, there is always the obvious purpose of exploring the mass spectra of various particle combinations. The experimental physicist hopes for the welcome accident to occur - viz. for new resonances to show up. Under suitable circumstances one can go further and try to determine their quantum numbers.

At the time the present experiment was started, the theory of elementary particles was rapidly developing and quite encouraging. The pseudoscalar mesons i.e. (π, K,η and X^o), the vector mesons (ρ, K*, ω and φ) and the spin $\frac{1}{2}$ baryons (Σ , N, Ξ and Λ) formed SU3 octets while the $J^P = 3/2^+$ baryons (N*, Y* and Ξ^*) almost completed a decuplet. As mentioned before, only the iso-singlet member, the Ω^- , was missing and its properties had been predicted. The A_2 and f^o mesons were known to have spin 2 and positive parity but could not be definitely attributed to a unitary multiplet with too many members still missing.

Even more colour was added to the theoretical scene by postulating that particles are manifestations of the so-called Regge-trajectories i.e. lines on a continuous α - t plane. The

variables α and t associated with the trajectories appear as spin and square of the rest mass respectively, in the case of physically observed particles. In the Chew - Frautschi scheme, all particles taking part in strong interactions are postulated to lie on Regge-trajectories and thus each trajectory can give rise to a series of particles with their spins increasing by units of two.

The peripheral nature of high energy interactions received a fair amount of theoretical attention. Calculations had been made according to a 'one-meson-exchange' Feynmann diagram but this 'unadorned peripheral model' failed to give satisfactory quanti - tative fit to experimental data. The failure was explained as due to renormalisation effects introduced by the two vertices and propagator for the exchanged particle. To deal with these, Ferrari and Selleri introduced 'form-factors' which proved to be quite adequate. However, they contained most of the t-dependence (t representing square of the four-momentum transfer) of the observed differential cross-sections and the whole theory became rather unconstrained. The one-meson-exchange model came to need some support to survive.

With this unsettled climate in the theoretical world, there was a great thirst for high energy data, specially for two-body final states. In the field of K^-P interactions, the range of 1.0 to 3.0 Gev of beam momentum had been extensively covered by experiments done at Lawrence Radiation Lab. , Berkeley ,

Brookhaven National Lab. and C.E.R.N.. By the time the present experiment was started, results were obtained in the 3.5 Gev experiment by the British collaboration and experiments were being done at 4.6 and 5.0 Gev by B.N.L. and at 4.1 and 5.5 Gev by groups at Argonne National Lab. and Northwestern University. There were also the K^+P experiments done at 4.6 Gev (L.R.L.) and at 3, 3.5 and 5 Gev (C.E.R.N.) which greatly contributed to the world knowledge of K - physics.

However, by 1964 the only mesonic resonance of strangeness ± 1 to have been well - established was the K^*_{890}. Its spin and parity were known and it had been identified as the hypercharged member of the 1^- meson octet. Several other strange mesonic states were observed occasionally and not fully recognised as particles. Examples are the κ_{725}, $K^*_{c\,1215}$ and K^*_{1320}. The K^*_{1400}, however, after its discovery in '65 by the British collaboration quickly gained the status of an established resonance and, with its J^P determined to be 2^+, was hailed into the 2^+ meson octet.

The 'peripheral model' of high energy interactions had gained a substantial popularity through these experiments. Many processes appeared to go via a one particle exchange, which included baryon - exchange as well. In later experiments diffraction scattering at either vertex of the O P E Feynmann diagram was assumed to be responsible for some observed

enhancements in mass spectra. The identification of $A_1(1080)$ and $K^*(1320)$ as resonances became controversial.

With this background, the present experiment can be believed to have been useful in the study of strangeness -1 mesonic mass spectra. There have been many suggestive features in this experiment which unfortunately proved to be inconclusive because of low statistical significance. A conflict between greater purification and larger size of a sample has often been faced and a compromise has been forced.

Between June and November '64, about 500 K pictures were taken with the British National Hydrogen Bubble Chamber at the C.E.R.N. proton synchrotron. A previous exposure in an 81 cm. Saclay chamber had yielded about 60K pictures. In the analysis stage it was found that poor statistics made the data almost useless by itself and due to the much smaller size, the chamber proved to be very unsuitable for a 6 Gev K^- experiment. The data obtained from this exposure have not been used in this thesis. The film taken with the BNHBC was divided equally among six collaborating groups viz.

University of Birmingham

University of Glasgow

Imperial College, London

Max-Planck Institüt für Physik und

Astrophysik, Munich

University of Oxford

Rutherford High Energy Laboratory, Harwell.

The findings of this experiment have been reported in the following articles published as yet:

K^{o} production channels in 6 Gev $K^{-}P$ interactions - presented at the Oxford Int. Conf. on Elem. Particles, '65.

Y^{*} production in $K^{-}P$ interactions at 6.0 Gev/c - do.

Ω^{-} production by 6 Gev K^{-}mesons - do. (Also presented in Physics Letters, 19, 2, '65.)

Quasi two body final states in 6 Gev $K^{-}P$ interactions - presented at the XIIIth. Int. Conf. on High Energy Physics, Berkeley, '66.

$\bar{K}\pi$ and $\bar{K}\pi\pi$ systems produced in the reactions $K^{-}P \rightarrow \bar{K}^{o}P\pi^{-}\pi^{o}$ and $K^{-}P \rightarrow \bar{K}^{o}n\pi^{+}\pi^{-}$ at 6 Gev/c - do.

Chapter 2 Instrumentation - Beam, bubble chamber, scanning and measuring machines.

The apparatus required in a bubble chamber experiment is essentially the following:

The beam i.e. an assembly of magnets, electrostatic fields, slits etc. to provide a flux of the required particles at the desired momentum with the least amount of impurity.

The bubble chamber with which photographs of interactions are taken.

Scanning machines which are essentially projectors used in examining the film and searching visually for interesting 'events' or interactions.

Measuring machines to digitize points on the film in a form suitable for further processing.

Although not directly related to the physics of the experiment, one other piece of apparatus absolutely essential to a modern bubble chamber experiment is the electronic computer.

The rest of this chapter would be devoted to descriptions of the instruments used in the present experiment.

The beam

The 6 Gev K^- particles were provided by a general purpose beam constructed at the C.E.R.N. proton synchrotron, known as the 0 2 beam.[3] It was designed to produce fairly pure beams of $P,\bar{P},K$ and π s of upto about 15 Gev momentum for use in experiments with the BNHBC. It had the option of electrostatic and radio-frequency separation, the electrostatic method being used in the present experiment.

Fig. 2.1 shows the beam layout. Secondary particles are produced by allowing the 25 Gev circulating beam in the P.S. to hit an aluminium target. The target was placed inside one of the P.S. magnet units. The angle of production for negative secondaries was essentially zero. This is an advantage since the secondaries are produced at high energies with a strong forward peak in the angular distribution.

The beam may be looked upon as consisting of three parts. In the first part, the solid angle acceptance is defined by the collimators 3-4. The momentum bite is also defined by the bending magnets 7-8 and the collimator 10. The main function of the second part is to carry out mass separation in three electrostatic separators of total length about 30 metres. In the rest of the beam the angular acceptance and the momentum bite are redefined and the beam is steered into the bubble chamber. A pulsed bending magnet sweeps the beam across the

chamber width.

A system of scintillation and cerenkov counters counted the total no. of particles and the no. of unwanted particles passing through the chamber and displayed them on the data panel.

The bubble chamber

Essentially, a bubble chamber is a vessel containing a transparent superheated liquid. It is provided with arrangements for illumination and at least one transparent window to allow photographs to be taken. A charged particle passing through the superheated liquid produces ionisation and initiates boiling along its track. The chamber is photographed soon after the bubbles are formed and the tracks are seen as strings of tiny bubbles. The chamber liquid acts as the target material as well for producing interactions. The chamber is usually placed in a magnetic field so that the tracks of charged particles are curved and their momenta can be measured by measuring the curvatures.

The British National Hydrogen Bubble Chamber used in the present experiment is described in details elsewhere[4] and only some of the important features would be mentioned here. The general arrangement is shown in fig. 2.2 .

The important parameters are:

Length	150 cms.	Wt.of magnet	300 tons
Width	50 "	Magnetic field	13.5 Kgauss
Depth	45 "	Film used	35mm. unperforated.

The chamber employs three cameras, each operating independently. The length is divided into three parts for illumination, each being illuminated by three ring-shaped flash tubes and a condenser system. The flash tubes produce real images around the three camera lenses and a scattering angle of only about 2° is required for light scattered from the bubbles to reach the camera.

The chamber vessel is suspended inside a steel vacuum tank and is surrounded by a hydrogen shield cooled to liquid hydrogen temperature and a nitrogen shield with pipes circulating liquid nitrogen. A gas phase expansion system is employed. The expansion takes place from the top through 48 pipes distributed uniformly over the top surface of the chamber to ~~ascertain~~ ensure a uni-axial flow of the liquid during expansion.

The cameras photographed a data panel along with the chamber. It contained book-keeping information like date, frame no. etc. as well as the counts for total no. and no. of unwanted particles.

Altogether, the chamber proved to be reasonably satisfactory for the present experiment. Only about 12% of

the neutral 'K's produced in the first 65% of the chamber were found to decay outside the fiducial volume in which decaying neutrals were accepted as well-measurable. The aspect ratio of 3:1 was a desirable feature as well since secondary particles are produced strongly forwards in the laboratory. Therefore, the best use of the chamber volume could be made with an oblong chamber.

Scanning tables

A scanning table is, in principle, a projector with enough accuracy to allow rough quantitative measurements and fast but simple-to-handle film drives. It should have sufficiently good resolution to show individual bubbles in the projected image. The machines used at I.C. use commercially available enlarging lenses which have proved to be quite adequate. A pair of plain mirrors reflects the light rays to form a focussed image on a horizontal table. They also keep the machines to manageable dimensions. A vacuum pump sucks the film down against a glass plate while the picture is being studied, to ensure good focussing and also to stop it from sliding away.

All three views can be projected at once and their relative positions adjusted. This is useful in comparing a stereo-pair to obtain information about the depth of a point in chamber.

Measuring machines

The three measuring machines used at Imperial College were each of a slightly different type but of comparable measuring accuracy.

The most elaborate one is a 'National Measuring Machine' and its optics are described in ref. (5). It has the film-carrying stage and the projecting lenses moving at right angles to each other for mechanical stability. The measuring channel is served by a mercury lamp. The green part of its spectrum is used to provide a 30X view of the measured part of the film for the measurer. The blue-violet part forms a similar image at a photo-electric detector used for automatic track-following. A tungsten lamp gives a 9X stationery view of the whole frame for viewing only. The digitizing is done with Moiré fringes.

A second machine was a less elaborate version of the previous one and had no high magnification view. The third was much less sophisticated, had no track-following arrangements and the movements of the film carrying stage were digitized in both x and y directions, still with Moiré fringes.

At a later stage, a semi-automatic device to guide the machines to fiduciaries and apices to be measured was attached to the first two machines described above.

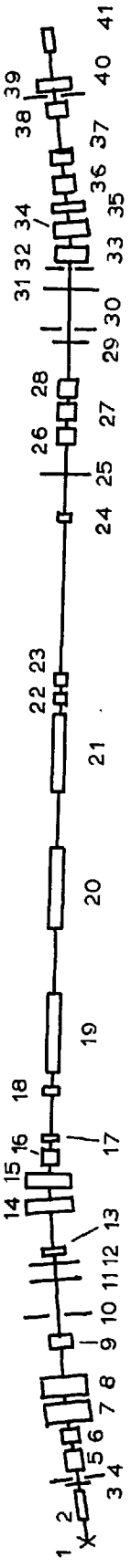

FIG. 2.1

THE O2 BEAM

2m. quadrupoles	5,6,16,26,27, 28,36,37
1m. quadrupoles	9,13,17,22,23,24
½m. quadrupole	18
2m. bending magnets	7,8,14,15, 33,34
1m. bending magnets	35,40
Pulsed magnet	38
Horizontal collimators	4,10,30, 32,39
Vertical collimators	3,11,12, 25,29,31
Electrostatic separators	19,20,21
Target	1
Beam pipe	2
Bubble chamber	41

FIG. 2.2

Layout of
the B.N.H.B.C.

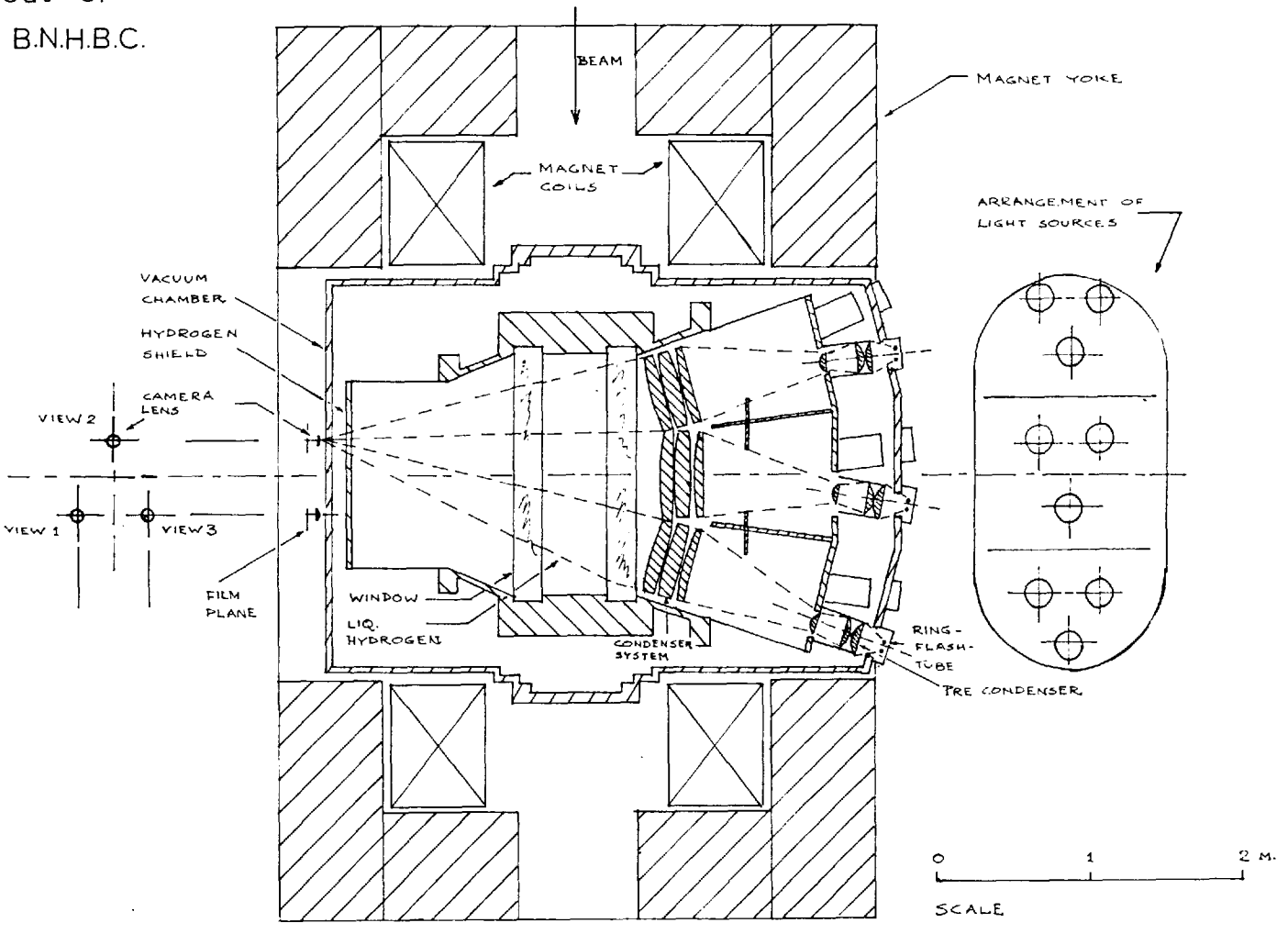

Chapter 3 General flow and data - processing

A total of about 50,000 photographs (i.e. stereo - triplets were analysed at Imperial College and, as in other typical bubble chamber experiments, this required a system for mass data handling. The system used evolved mainly from that used in a previous 3.5 Gev K^-P experiment by the British collaboration including an I.C. group.

The general flow in this experiment is shown in fig. 3.1. The essential stages are :

(a) Scanning

(b) Measuring

(c) Computing through Geometry and Kinematics

(d) Compilation and Statistical analysis of the data.

The different steps involved will be discussed in some details in the rest of this chapter.

Scanning

The 3-view film was scanned twice independently to reduce scanning losses and misidentifications. Different topologies were named with three numbers, according to a widespread convention, as $i\,j^{\pm}k$ where

i = total no. of charged outgoing tracks,

j = total no. of these tracks with charged secondary particle decays or 'kinks', the sign denoting the charge of the decaying particle and

k = total no. of neutral strange particle or 'V^o' decays associated.

All topologies including 'tau' decays i.e. decay of a beam track into three charged tracks were scanned for, except stops and θ decays of the beam tracks. Two rectangles were defined on the central view, called view 2, and are shown as A and B on fig. 3.2. Events with one or no visible strange particle decay were accepted only if the following were satisfied: (1) The beam enters through the base of A

(2) The production vertex must lie within A

(3) The decay vertex of the neutral or charged strange particle must lie within B.

These events were termed 'common' events. The 'rare' events with two or more associated strange particle decays were accepted over the visible region of the chamber. The purpose of accepting common events only over a limited region was to have a good standard of measurability and also to avoid small potential decay lengths of decaying strange particles. The latter was necessary to avoid large weights on individual events, details about which are discussed in chapter 4.

Associated electron pairs, 'Dalitz pairs' or e^+e^- pairs arising from the γe^+e^- decay mode of the π^o, interactions

of secondary tracks giving rise to decaying strange particles, 'π-μ-e's, stopping secondary tracks and other features helping the identification of events were noted down at the scanning stage. The criteria for accepting V^os as associated were made rather lenient for safety. Any V^o with the line joining the production vertex and the decay vertex passing in between the charged prongs was accepted as associated and any rejection made at a later stage on the basis of the results of kinematic fitting.

The distinction between electron pairs and V^os was made with the following criteria:

1) An electron pair must have no distinguishable opening angle on any view.

2) If at least one track has a momentum less than 140 Mev and appears to be minimum ionising, it is classed as an electron pair. On the other hand, if any of the prongs is more than minimum ionising, it is classed as a V^o.

It is found that the above criteria have a strong bias against fast Λs when the Λ decays in its own rest frame with the proton going backwards with respect to the direction of flight. In this case the opening angle remains sufficiently small in the lab. system to simulate an electron pair for a wide range in the centre of mass decay angle. However, in this particular situation the momenta of the positive and

negative decay tracks obey the relation $p_+/p_- \approx 3$. One added criterion was therefore used - unless inconsistent in ionisation, an object looking like an e.p. would be accepted as a V^o if the condition $p_+/p_- \neq 3$ is satisfied.

The first two independent scans were done on views 1 and 2 and views 2 and 3 respectively. A third compared the results of these two, solved any discrepancies and made out scan cards. The scan cards contained information like frame and event nos. of the event, approximate position in the chamber, a rough sketch of the event showing labels of tracks and vertices, possible alternative origins of V^os and any relevant information for the physicist or the measurer. Besides being a record of the event, the scan cards served the essential purpose of communication between the physicist and the measurer.

Measuring

The process of measuring was carried out more or less mechanically by measurers and little physics was involved. It consists of measuring points on tracks or at vertices by setting some kind of fiducial mark on them and labelling them according to instructions on the scan cards. Stopping tracks were measured with a special label for identification. Common events were measured on all three views only, the event being rejected if it was not possible to do so. No such restriction was put on rare events. The output of the measuring machines was

in the form of punched paper tape ready for computation.

Computation

The process of computation can be subdivided into several steps:

(1) Paper tape to magnetic tape conversion - This conversion was done on an IBM 1401 computer with an attached paper tape reader. An event took about 4 seconds to be read from paper tape and written character by character onto magnetic tape. Conversion to magnetic tape in the earliest stage had the advantage that all subsequent computation could be done on the IBM 7090 which obviously meant neater and quicker processing.

(2) Conversion into input format for the JOKING system - A fortran 2 programme called PING (Programme for Input into Nirns Geometry), running on the IBM 7090 read the paper tape image mag. tape and wrote out a BCD tape in the format required by the Joking Geometry. It also produced diagnostics for faulty measurements, e.g. with mispunches, wrong labelling etc., some of which could be corrected by editing the paper tape and reprocessed. 'Ping'ing took about 3 seconds per event.

(3) Geometrical reconstruction and kinematic fitting - These were done with the JOKING (JOint KINematics and Geometry) system which used the Ping output as the input. The geometry

programme produced a binary 'library' tape containing book - keeping information and measured values of variables associated with each event with the errors. Similar but less detailed information was written onto the paper output produced. For badly measured events, diagnostics about the faults were produced and the library contained only the book-keeping information. In a special version of this programme developed at I.C., a partial geometry was produced for events with only some tracks badly measured. This library, together with new measurements of previously failed tracks could be treated by this version to produce a complete library for the event.

The kinematics part of the Joking system read the library produced by the geometry programme and produced a new library tape in the same format but containing the results of fitting as well. This tape could be used either to try other hypotheses on the same events or to produce another tape in the format demanded by the Statistics programme. Some details of the geometry and kinematics programmes would be discussed below.

The geometry programme :

The aim of the geometry programme is to utilise the measurements made on film on fiducial marks, tracks and vertices and provide the later stages of processing with estimates of vertex coordinates, angles and momenta of the tracks with the associated errors.

The path of a charged particle in an ionising medium and a magnetic field is approximately a helix. The deviation from a perfect helix arises from the slowing down by ionisation loss of energy. The ionisation loss and, therefore, the rate of change of momentum depends on the mass of the particle. The final space curve fitted to the measurements has mass dependent parameters as a result. A huge amount of algebra is involved in the theory of reconstruction of an event in space and only the steps will be briefly discussed.

The measured positions of the fiduciaries are first compared with fed-in values. The rotation and shrinkages in the x and y directions required to bring the measured points on fiduciaries to the standard positions are calculated and applied to the other coordinates measured. This corrects for any misalignment of the x and y directions of the measuring machine and in the chamber, linear distortions as film shrinkage, etc. .

Vertex positions can be calculated in two independent ways. Firstly, the rays corresponding to the measured points at vertices are produced back to the film plane on three views as also a point (x,y,z) in the chamber. The vertex position can be found by minimising the sum of squares of the distances of the projected images of (x,y,z) on three views from the points where the rays meet the film plane on corresponding

views. Alternatively, after the tracks have been reconstructed, one can minimise the sum of squares of distances of a point in space from the tracks meeting at that vertex.

In practice, both the methods are used. The quantity minimised is

$$M = \sum_{i=1}^{NV} \left(\frac{d_i^v}{s_v \text{ st.}} \right)^2 + \sum_{i=1}^{NV.NT} \left(\frac{d_i^t}{s_t \text{ st.}} \right)^2$$

where d_i^v = distance between projected image of (x,y,z) on film plane and the foot of ray corresponding to measured point at vertex on ith. view,

d_i^t = distance between the space point (x,y,z) and the ith. track at the vertex,

NT = total no. of tracks at the vertex,

NV = no. of views on which vertex is measured,

s_v = standard error in vertex measurement (fed in) and

s_t = standard error in setting on track. (fed in)

This minimisation is done by an iterative method. In this process the quantities $1/s_v^2$ and $1/s_t^2$ are used as weights and after the determination of x,y,z it is checked whether the use of standard values of s_v and s_t is permitted in this particular case or not. New values of s_v and s_t are calculated as

$$s_v^2 = \sum_i \frac{d_i^{v\,2}}{2.NV - 3} \qquad \text{and} \qquad s_t^2 = \sum_i \frac{d_i^{t\,2}}{NV.NT}$$

If now it is found that

$s_{v\,calc.}^2 / s_{v\,st.}^2 > \beta$ and/or

$s_{t\,calc.}^2 / s_{t\,st.}^2 > \beta$ where β is a specified quantity, then the use of standard s_v, s_t in the iteration previously described is considered unsatisfactory and is re-done after replacing the standard values of s_v and s_t by the calculated ones. This recalculation is required for only few events with unusually large measurement errors on vertices.

For the reconstruction of tracks, the conversion of points to rays is done in the normal manner. As a check for badly measured points, a parabola, or in the case of sufficiently straight tracks, a straight line is fitted to the (x,y) points on the $z = 0$ plane (i.e. the front glass - liquid interface). Points lying more than a maximum distance away from this fitted curve or straight line are rejected and the fit repeated.

The first stage in the three-dimensional reconstruction of the event is to find corresponding points. When a point in the chamber is viewed by two cameras, the line joining the points x_1, y_1 and x_2, y_2 i.e. the points where the rays cut the z=o plane, is parallel to the line joining the two camera lenses. If three views are measured, a best view is chosen depending on the projected length of the track on this view and the stereo-angles for pairs formed with the other two views.

For the points measured on the main view chosen, corresponding points are found on the other two views by interpolation.

At this stage, the x,y and z coordinates of several points on each track are known and a space curve can be fitted. This process is divided into two parts - a circle or parabola or straight line is fitted to the x-y coordinates and then a z-fit is done with the z coordinate linearly increasing with the angle the track turns through.

The two stage fitting just described produces a mass independent helix fit without slowing down correction. A serious defect of this fit is that the errors in the parameters involved are very complicated functions of the measurement errors made on film and are almost impossible to calculate. As such, a different method is used which uses the fit made so far as a starting value. The helix formed in space in the bubble chamber is projected back on to the film plane on all three views. The rays are also projected similarly and the best fit is found by minimising Σd_i^2 where d_i = distance of the point where the ith.ray cuts the film plane from the projected image of the helix. The summation extends over all measured points on all views.

The helix finally fitted to space points has mass dependent corrections and the fits are done for proton, K and π masses.

Certain other facilities are built into the programme. It can find the momentum of stopping tracks from the range. For all vertices with three charged tracks a test for coplanarity was done and if it was satisfied, a flag was set in the library for the event to communicate the information to the kinematics programme.

The kinematics programme :

The aim of kinematic fitting is to adjust the measured values of track variables, i.e. momenta and angles, to satisfy the constraints of energy-momentum conservation by the method of least squares. The procedure is dealt with in details in refs. 6-7.

The method of least squares is applicable only when the variables have gaussian distributions. The Joking system uses the centre-of-track values of $1/p$, $\tan\lambda$ and φ as the variables where p, λ and φ stand for momentum, dip and azimuth respectively. These are the quantities most likely to behave as gaussian.

Energy-momentum conservation gives the following constraints at any vertex:

$$\Sigma \pm E_i = 0$$

$$\Sigma \pm P_i \sin\lambda_i . \sin\varphi_i = 0$$

$$\Sigma \pm P_i \sin\lambda_i . \cos\varphi_i = 0$$

$$\Sigma \pm P_i \cos\varphi\lambda_i = 0 \quad ,$$

where the positive signs are taken for the outgoing tracks and the negatives for the incoming ones. If x_i stands for all the variables in a fit then the error matrix G_{ij} is defined by $G_{ij}^{-1} = \langle \delta x_i^m . \delta x_j^m \rangle$, the brackets representing the expected value. Inter-track correlations are ignored in the calculations so that the matrix G^{-1} consists of a string of 3 X 3 matrices along the diagonal. The quantity

$$\Sigma\Sigma \quad (x_i - x_i^m)\, G_{ij}\, (x_j - x_j^m)$$

has to be minimised to find the fitted values of the variables in such a way as to obey the constraint equations as well. This is done by minimising instead

$$M = \sum_{i,j=1}^{I} (x_i - x_i^m)\, G_{ij}\, (x_j - x_j^m) + 2 \sum_{l=1}^{L} a_l f_l(\underline{x})$$

where a_l = undetermined multiplier

f_l = value of the lth. constraint

I = total no. of variables

L = total no. of constraint equations for the fit.

This is, in fact, equivalent to solving the L constraint equations for L of the variables and then minimising a X^2 involving I - L variables. This is unpractical since the constraint equations are non-linear and one solves the I + L simultaneous equations:

$$\frac{\delta M}{\delta x_i} = 0, \quad i=1 \text{ to } I$$

$$\frac{\delta M}{\delta a_i} = 0, \quad i=1 \text{ to } L .$$

These give the $I+L$ simultaneous equations -

$$\sum_j G_{ij}(x_j - x_j^m) + \sum_l a_l F_{il}(\underline{x}) = 0, \quad i=1,I$$

$$f_l(\underline{x}) = 0, \quad l=1,l$$

where $F_{il}(\underline{x}) = \dfrac{\partial f_l(\underline{x})}{\partial x_i}$.

These equations are solved iteratively. If $\underline{x}^n$ = value of the vector $\underline{x}$ at the nth. stage of iteration, then assuming that $F_{il}(\underline{x})$ is a slowly varying function of $\underline{x}$ so that $F_{il}(\underline{x}^n)$ is a sufficiently good approximation of $F_{il}(\underline{x}^r)$, $\underline{x}^r$ being the required root, the first eqn. can be written as

$$\Sigma G_{ij}(x_j - x_j^m) + \Sigma a_l F_{il}(\underline{x}^n) = 0.$$

A first order Taylor expansion of the second equation around $\underline{x} = \underline{x}^n$ gives $f_l(\underline{x}^n) + \Sigma F_{il}(\underline{x}^n)(x_i - x_i^n) = 0.$

The two sets of simultaneous equations can be written in matrix form as $G(\underline{x} - \underline{x}_m) + F.\underline{a} = 0$

$$\underline{f} + F^t(\underline{x} - \underline{x}_m) = 0 \text{ , where } F^t = \text{transpose of } F.$$

From these,

$$\underline{x} = \underline{x}_m - G^{-1}.F(\underline{x}^n).H^{-1}.(\underline{x}^n).\ \underline{b}(\underline{x}^n)$$

where $H = F^t\ G^{-1}\ F$

$\underline{b} = F^t(\underline{x}_m - \underline{x}^n) + \underline{f}$, $\underline{x}_m$ here being the measured values.

This is linear equation in $\underline{x}$ and the quantities on the right can be calculated. The value thus obtained for $\underline{x}$ can be used $\underline{x}^{n+1}$ for the next iteration. For the starting values one uses

$$\underline{x}^o = \underline{x}_m$$

$$\underline{a}^o = o\,.$$

There are two obvious problems. The process of iteration should be terminated when there is no more any significant change in $\underline{x}^n$ and also there should be an error exit for wrong hypotheses as quickly as possible. At each stage of iteration a X^2 is calculated which is a measure of the stretching that has already been done on the variables. Iteration is terminated if the sum of squares of constraint unbalances drops below a specified value and also the proportional change in X^2 since the last iteration is sufficiently small.

On the other hand, a fit is rejected if, for example, X^2 is too large at the stationery value or the constraint unbalance increases more than a specified no. of times. However, these criteria are still not perfect. Cases have been observed in this experiment, for example, where the X^2 oscillates through the stationery value and even though the constraint unbalance becomes essentially zero at some stage, the programme fails to detect that an acceptable fit has been reached. As a result, it rejects the correct hypothesis which is apparent by the fact that the hypothesis is fitted without any trouble to a slightly different measurement of the same event.

An important function of the fitting process is to improve the quality of measurements. The errors on the fitted quantities are smaller than the measurement errors. The reason, stated

qualitatively, is that kinematic fitting utilises the added information of energy-momentum conservation.

A set of quantities called stretches is calculated by the kinematics programme for studying systematic errors. The stretch in a variable x_i is defined as

$$S(x_i) = \frac{x_i^{fitted} - x_i^{m}}{< x_i^{fitted} - x_i^{m} >_{rms}} .$$

If there are no systematic errors in the measurement of a variable and if the errors are correctly estimated, the corresponding stretch would have a normal distribution.

A part of the kinematics programme also calculated effective masses and various angles associated with different particle combinations.

The kinematics library was run through a programme called Inco which picked up selected fits and wrote another binary tape called the data summary tape. This contained essentially the vertex coordinates and the vertex values of the track variables in a compact form.

(4) Statistical analysis -

This was done mainly with the Statistics programme which read fitted information about the events from the data summary tape. It could plot histograms and 2-D scatter diagrams to display effective masses of different particle combinations,

their c.m. production angles and other interesting angles, 4-momentum transfers etc. . The calculated angles, shown in fig. 3.3, can be defined as follows:

$$\cos\alpha = \underline{r}_c \cdot \underline{b}$$

$$\cos\beta = \underline{r}_c \cdot \underline{d}_r$$

$$\cos(\theta \text{ or } S_1) = \underline{b}_r \cdot \underline{d}_r$$

$$\cos S_2 = \underline{n} \cdot \underline{d}_r$$

$$\cos S_3 = (\underline{b}_r \times \underline{n}) \cdot \underline{d}_r \,/\, |\underline{b}_r \times \underline{n}|$$

$$\varphi = \tan^{-1}(\cos S_2 / \cos S_3)$$

where all the vectors are unit vectors in the following directions:

$\underline{r}_c$ - resonance line of flight in c.of m.

$\underline{b}$ - beam dirn. in lab. or c.m.

$\underline{b}_r$ - beam dirn. in the resonance c. of m.

$\underline{d}_r$ - line of flight of decay product in the resonance c. of m.

$\underline{n}$ - normal to production plane i.e. $\underline{b} \times \underline{r}_c / |\underline{b} \times \underline{r}_c|$.

The programme had facilities for making selections on the basis of effective masses, production angles of particle combinations etc. . It could deal with the weighting of events if a V-decay was involved.

The main feature of this programme was that it read in the minimum amount of data and calculated effective masses etc. as it read through the data summary tape. With a computer

of the speed of the IBM 7090 the tape reading took a considerable fraction of the total operating time which is a good reason for favouring a compact data summary tape. This, however, reduced the flexibility of the programme. At the same time, by occupying a large space in the computer memory, it made it difficult to deal with events having many tracks.

Statistical methods

Most of the information that a typical bubble chamber experiment aims at obtaining, can only be derived from the observation of a large no. of events of the same type. Once such a number of events has accumulated, one looks at the distributions of various physical quantities and compares them with expected ones on the basis of certain hypotheses. Any significant deviation of the observed distribution from the expected one indicates some special mechanism. The 'significance' is important because statistical fluctuations always produce some deviation. It can be assessed by statistical means alone. An assortment of statistical methods used in this experiment would be discussed in this section.

The data are often presented in the form of histograms and scatter-plots. In general, the no. of events in a bin or a given

area follows a binomial distribution

$$P(n) = {}^{N}C_{n} \cdot p^{n} \cdot (1-p)^{N-n}$$

where N = total no. of events

p = hypothetical mean of the fraction of events in the bin.

The observed no. of events, n, has mean and variance given by

$$\bar{n} = N \cdot p$$

$$Var(n) = N.p.(1-p).$$

If n/N is taken as an estimate of p, then $Var(n) = n(1-\frac{n}{N})$. If $n << N$, $Var(n) = n$. If n' events are observed where n are expected, $(n' - n)/\sqrt{n}$ can be taken as a normal variable and the standard method of confidence limits can be used.

Physical parameters are often estimated by fitting curves to observed distributions. One standard way available is the maximum likelihood method which has the advantage that complicated curves present no problem. If an event is described by I coordinates $\underline{x}_i$, i=1,I and the function to be fitted is $f(\underline{x}_i, \underline{a}_j, j=1,J)$ with J parameters, then the likelihood function is defined as $F = \Pi f(\underline{a}_j, \underline{x}_i)$, the product running over all observations i.e. events. The best values of the parameters $\underline{a}_j$ are found by searching for the maximum of F in the J-dimensional parameter space. Near the maximum, the function F behaves as multi-gaussian with respect to the parameters $\underline{a}_j$ and the errors in the estimates of these parameters are found very simply by measuring the width of the peak with respect to

these parameters.

In the case of fitting an exponential to a set of numbers t_i of the form $\frac{dn}{dt} = N \cdot a \cdot \exp(-a.t)$, the maximum likelihood method boils down to $a = 1/\bar{t}$, $\Delta a = a\sqrt{\frac{1.4}{N}}$, N being the total no. of events.

The maximum likelihood method has been coded in fortran in a routine called MALIK which has been used in this experiment.

The correlation between two variables can be studied qualitatively with the help of the 'product-moment-correlation-coefficient' defined as $r_{xy} = \frac{\Sigma_i (x_i-\bar{x})(y_i-\bar{y})}{n \cdot \sigma_x \cdot \sigma_y}$ where

σ_x, σ_y = standard deviations of the variables x and y with arithmetic means $\bar{x}$ and $\bar{y}$ and

n = total no. of pairs of x and y values.

The distribution of r is, in general, asymmetric and its error cannot be found directly. The quantity $z = \frac{1}{2} \log_e \frac{1+r}{1-r}$ is distributed as gaussian variable with mean zero and standard deviation $\sqrt{1/n-3}$. The errors in r can be inferred from σ_z.[8]

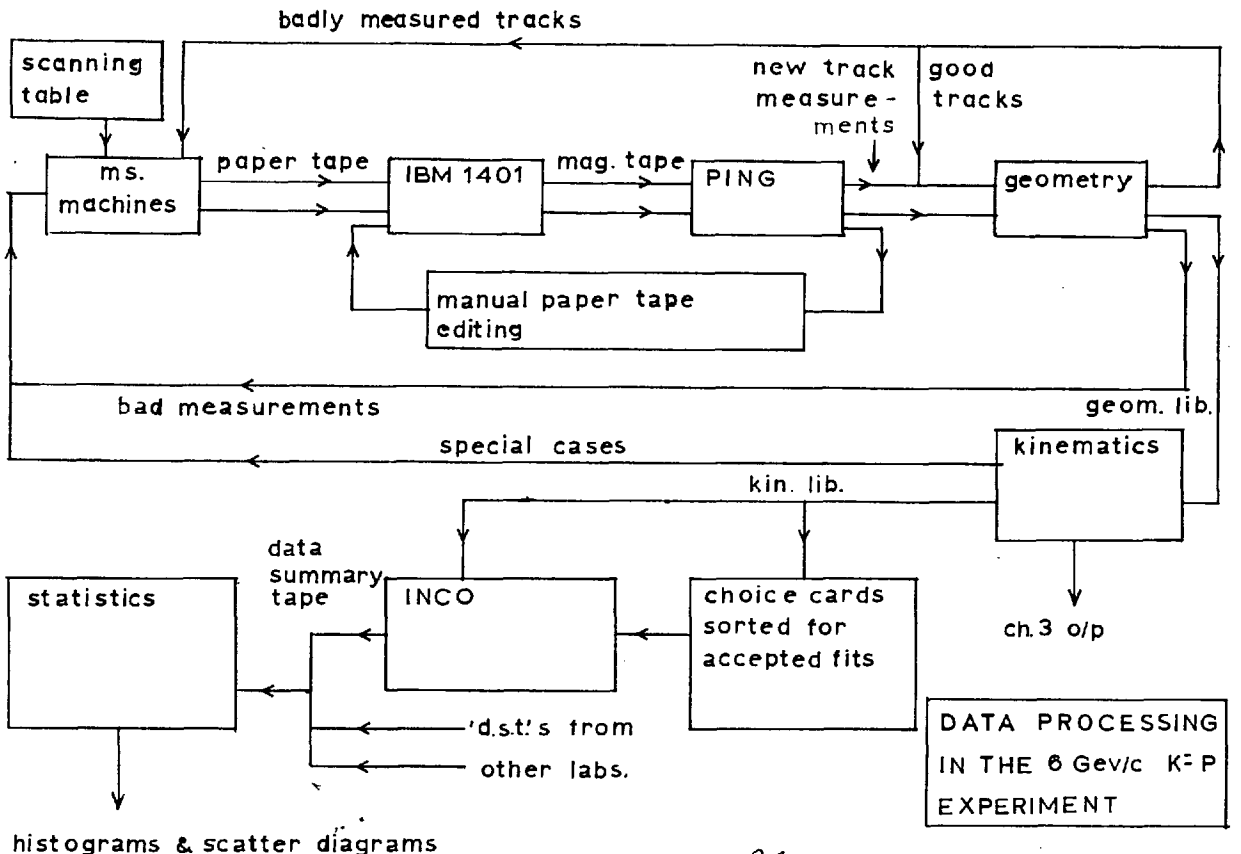
badly measured tracks
scanning table
new track measure-ments
good tracks
ms. machines
paper tape
IBM 1401
mag. tape
PING
geometry
manual paper tape editing
bad measurements
geom. lib.
special cases
kinematics
kin. lib.
data summary tape
statistics
INCO
choice cards sorted for accepted fits
ch.3 o/p
'd.s.t.'s from
other labs.
DATA PROCESSING IN THE 6 Gev/c K⁻P EXPERIMENT
histograms & scatter diagrams

FIG. 3.1.

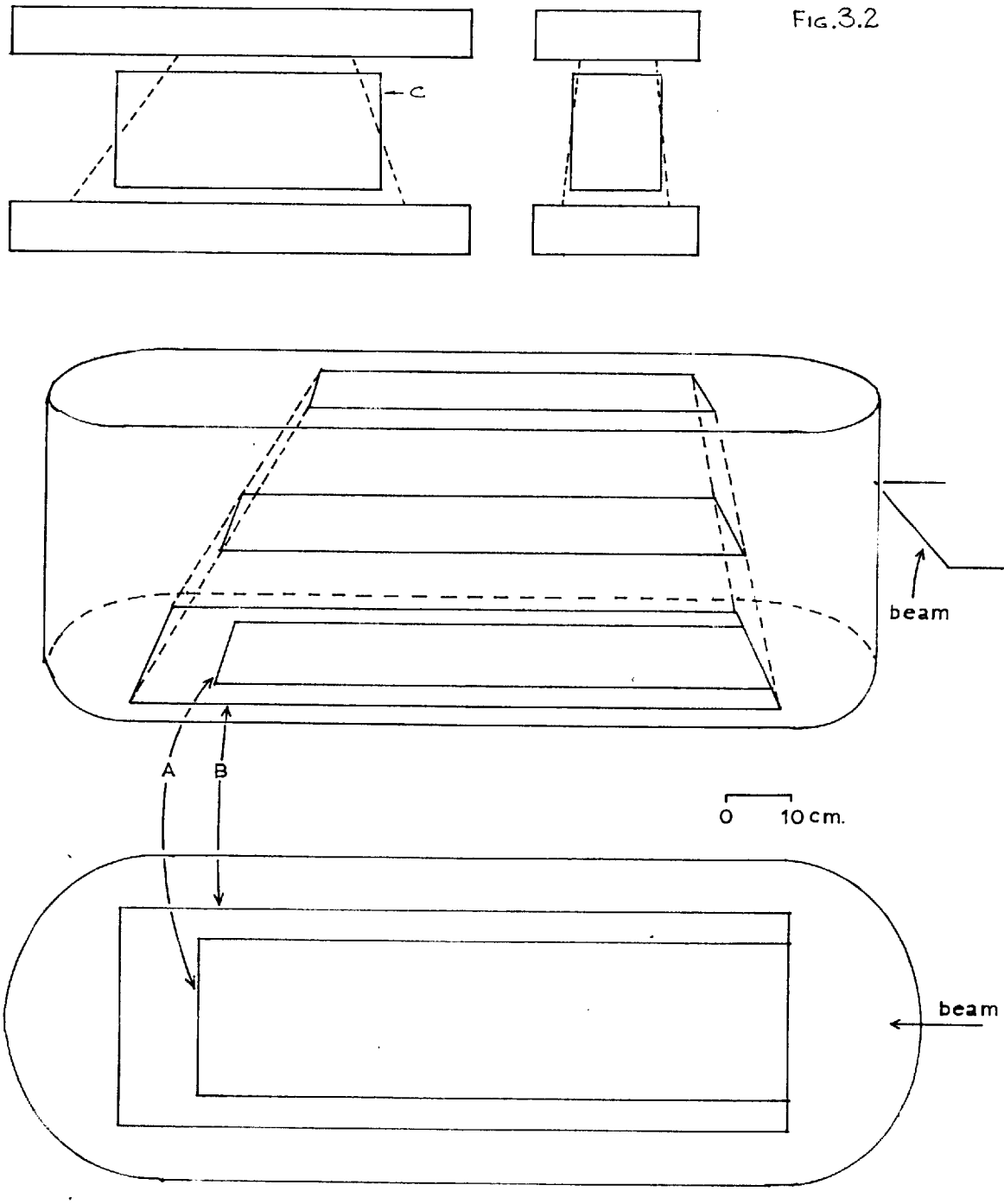

FIG. 3.2

FIG. 3.3

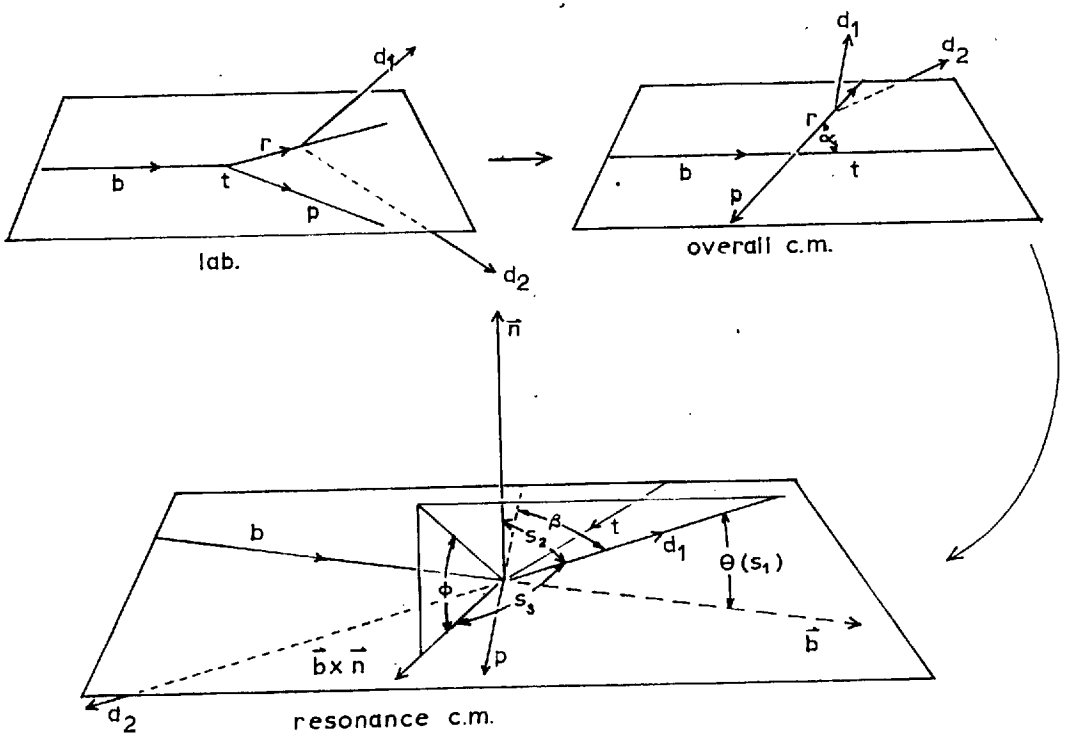
d1
r
b
t
p
d2
lab.
d1
d2
r
b
t
p
overall c.m.
n
b
β
s2
t
d1
θ(s1)
Φ
s3
b x n
p
b
d2
resonance c.m.

Chapter 4 — Errors - systematic and random, cross-section calculations.

Systematic as well as random errors can creep in at practically all stages of a bubble chamber experiment. In this chapter the various sources of errors would be discussed and the relevant cross-sections presented after correcting for the systematic errors.

Beam

The contamination of πs and μs have been determined in three independent ways. In the mass spectrum of the particles arriving at the mass slit, the Ks appear as a shoulder on the peak representing πs and μs. By folding the high mass side of the K peak the no. of πs and μs under the K peak can be found. The no. of μs alone was found by interposing lead plates in the beam to absorb Ks and πs by strong interaction so that the particles passing through the chamber were only μs.[9] The third method utilised the A (total no. of particles passing the chamber) and B (total no. of πs and μs through the chamber) counts obtained with the scintillation and cerenkov counters.

If p_K, p_π = probabilities that a K and a π would interact in the chamber

and f = expected value of (no. of πs / B)

then the expected no. of interactions in a frame or

$$N = (A-B).p_K + f.p_\pi.B \ .$$

If $\bar{N}/(A-B)$ is plotted against $B/(A-B)$ for different groups with the same value of $B/(A-B)$, the gradient and the intercept on the $\bar{N}/(A-B)$ axis give $f.p_\pi$ and p_K. p_K/p_π being known, f can be determined.

The contamination from μs is of no importance when absolute cross sections are required since they do not produce strong interactions. The pion contamination has been found to be as follows:

Run D (15 ± 5) %

Run E + F (3.5 ± 2.5) %

The spread in the beam momentum before entering the chamber is quoted by the beam designers to be 0.5% i.e. 30 Mev. Since reactions were measured over a fiducial volume about 100 cms. long, an additional fluctuation of about 25 Mev is put in by ionisation loss. To cover uncertainties in the beam momentum, a somewhat larger value of this error was fed into the kinematics programme - viz. 60 Mev. A histogram of the fitted beam momenta (centre of track value) of about 2000 '201's is shown in fig.4.1. The two separate peaks correspond to the runs (D + F) and E. Their central values are

Run D + F 6.017 Gev

Run E 6.032 Gev.

Scanning biases and chamber imperfections

Due to the finite size of the chamber, all strange particle decays cannot be measured. In the scanning stage, such decays

are accepted only in a fixed fiducial volume and this constitutes a bias against fast 'V's. On the other hand, charged as well as neutral V decays too close to the production vertex are often missed in scanning. These effects can be corrected for by rejecting all events with a V decay closer than a certain length from the production vertex and properly weighting all the accepted events.

If l = length travelled by a V before decay,

p = momentum of the V with mass m and mean life T in its own rest frame,

$x = l/p$ and

N_o = total no. of Vs produced,

then no. of Vs decaying with the value of x lying between x and $x+\Delta x$ is

$$\Delta N = \frac{N_o \cdot m}{c \cdot T} \exp\left(-\frac{x \cdot m}{c \cdot T}\right) \Delta x \ .$$

If all V decays are detected, the quantity $\Delta N/\Delta x$ should show an exponential fall-off with increasing x. Fig. 4.6 shows the distribution of $\Delta N/\Delta x$ against x for about 2000 $\overline{K}^o$s from fitted '201's, which should be a straight line of slope $(-m/c.T)$. It is apparent that there are a smaller no. of events with values of l/p less than 1.0 cm./Gev than expected. A depletion is found at high values of l/p as well which reflects the fact that K^os have been lost both by decay outside chamber and by loss of close V^o s during scanning.

Let L = potential length available to the V for decay within the required fiducial volume, (c, Fig 3.2)

r = minimum projected length to be travelled by the V to be accepted and

λ = dip of the V track.

The probability of observing this V is given by

$$P(p,\lambda,L) = \exp\left(-\frac{r \sec\lambda \cdot m}{p.c.t}\right) - \exp\left(-\frac{L \cdot m}{p.c.t}\right).$$

A fraction P of events of this category are observed and therefore different physical variables associated with this event are plotted with a weight $W(p,\lambda,L) = 1 / P(p,\lambda,L)$.

This method of weighting, although free from biases, has the drawback that the weight becomes a function of the position and orientation of the event in the chamber. These quantities are of no physical consequence and in some cases, e.g. if L is very small, the weights attain high values to produce fluctuations in different plots.

In the case of 201 s with K^o s, a minimum length cutoff of 0.6 cms. in chamber (i.e. about 0.3 cms. on the scanning table) has been applied. The average weight for these events has been found to be 1.16 i.e. about 16 % of the K^os have been lost.

It is possible to misidentify V^os decaying with low transverse momenta or to lose them during scanning as electron pairs. For a pure and unbiased sample of K^os, the distribution of the cosine

of the polar angle θ^* of decay i.e. the angle between the direction of motion of a K^o and that of the decay π^+ in the K^o centre of mass should be uniform. Fig. 4.7 shows this distribution for $\bar{K}^o_s$ in 201 s fitted to the final states (1) $\bar{K}^o P\pi^-\pi^o$, (2) $\bar{K}^o n\pi^+\pi^-$ and (3) $\bar{K}^o P\pi^-$. The distribution for (3) is consistent with isotropy but those for (1) and (2) show significant accumulation of events near the end with $\cos\theta^* = 1$. They correspond to V^os decaying with their positive decay products going forwards in their own rest frames with respect to their lines of flight. It is known that K^os and Λs decaying with this configuration can simulate each other kinematically. In the present experiment, a V^o fitting both as a K^o and as a Λ was accepted as a K^o if the event had a multivertex fit with the V^o as a K^o and none with the V^o as a Λ . The excess of events observed can be explained as events of the type $\Lambda\pi^+\pi^-$ + multineutrals. The contamination of such events is estimated to be

$$\bar{K}^o P\pi^-\pi^o - (3.1 \pm 1.4) \%$$

$$\bar{K}^o n\pi^+\pi^- - (7.5 \pm 1.2) \% .$$

The reason for the contamination for final state (1) being lower is, presumably, that the π^+ at the production vertex has to be fast enough to be indistinguishable from a proton by ionisation (i.e. > 1.5 Gev in momentum). The impurity is expected to be considerably less when a narrow resonance, such as K^{*-}_{890}, is selected.

Random scanning losses

Quite obviously, all the events on film are not detected in the scanning although scanning the film twice independently reduces the number of missed events to some extent and provides a rough idea of the scanning efficiency. A part of these missed events are unbiased i.e. do not belong to physically special classes. The events that do so may distort some distributions and introduce systematic errors in the determination of parameters of physical interest.

Assuming that the scanning loss is completely random and that there is no correlation between the chances of missing an event in the first and second scans, the scanning efficiency is given by

$$e = n_{12}(n_1+n_2-n_{12}) \;/\; n_1 \cdot n_2$$

where n_1 = no. of events found in the first scan,

n_2 = " second scan

and n_{12} = " both scans.

However, scanning losses mainly occur because of small angle decays on charged tracks, events being obscured by overlapping tracks etc. and thus an event missed in one scan is more likely to be missed in the second scan than average. The expression quoted above is therefore not strictly true and there is no direct and satisfactory way to correct for the scanning loss.

The scanning efficiencies for I.C. are listed in table 4.1 for different topologies.

Table 4.1

Topology	Scanning efficiency
201	.99
400	~1.00
001	.95
τ-decays	.90

A variety of distortions can enter between an event as it occurs in the bubble chamber and the photographs available for measurement. Lens distortion and systematic emulsion movements are corrected for in the geometrical reconstruction stage. Turbulence in the chamber liquid and random emulsion movements are not corrected. Some events may be more affected than others and measurements on them would have systematic errors. If they are measured twice, both measurements would be affected and this effect would show up in the stretching of physical variables in the process of kinematic fitting.

A sample of 27 V^o s has been used to study correlations in the X^2-probabilities of associated fit to their production vertices. A scatter plot of the two X^2-probabilities is shown in fig. 4.2. The product-moment correlation coefficient of the two probabilities is .77±.09, which is quite significant and indicates that a large part of the measurement errors come in between the actual events and the photographs.

Measuring and geometrical reconstruction

Biases in this part of the processing occur mainly due to slow and scattered tracks. Events with such tracks tend to fail in the reconstruction, the track being rejected as badly measured. Since these events may belong to definite physical categories, they were remeasured till the fraction of such events with no successful geometry was negligibly small.

Common events measurable on two views only have not been used since, apart from being less well-measurable, they may introduce a bias against tracks with small stereo-angles for the two available views.

Kinematic fitting

The kinematic fitting itself introduces very little bias in the sample of events processed. Only in very few cases it has been noticed that the programme failed to fit an event to the apparently correct hypothesis as mentioned in chapter 3. It has been found satisfactory to rerun these events with a different measurement.

The fits accepted were only those consistent with the ionisation density of the charged tracks. Assuming β (v/c) of beam tracks to be approximately 1.0 and its density of ionisation to be I_o, the same quantity for any charged track with momentum p, dip λ and assigned mass m is expected to be I given by

$$I = I_o\left(1 + \frac{m^2}{p^2}\right) \sec\lambda$$

when the line of viewing is parallel to the z - axis. It was found that tracks with relative ionisation (I/I_o) greater than 1.5 could be distinguishable from minimum ionising tracks while all tracks with more than 4 times minimum ionisation appeared to be completely dark and structureless.

The magnetic field in the chamber is adjusted using the invariant mass of the $\pi^+ - \pi^-$ from K^o decay as the guide. Once this is done, the stretch functions calculated by the kinematics programme can be used as a sensitive test for systematic errors. The stretch on (1/p) for the beam was used to find the central value of the beam momentum to be fed into kinematics. Fig.4.5(a) shows the distribution of this quantity for a sample of processed events. The distribution is found to be consistent with being normal.

The stretches on the dips of beam, outgoing charged tracks and outgoing neutral tracks are histogrammed in fig. 4.5 (b-d). It can be noticed that they are slightly displaced from the ideal mean of zero. The effect is of opposite signs for the beam and the outgoing tracks. The reason for this behaviour was found to be an error in the geometrical reconstruction stage which introduced a curvature in the plane normal to the camera axes. It amounted to an excess transverse momentum of 30 - 40 Mev. The effect of this on angles and effective masses was found to be

negligible but it produced a distortion in the X^2 distribution for the kinematic fits. The X^2 distributions for some 4-C and 7-C multivertex fits are displayed in fig. 4.3-4 , where the solid lines represent the expected distributions. A distinct tendency of the X^2s to be larger than expected can be observed.

Events were selected in such a way as to avoid the effect of the distortion in the X^2 distribution. For events with a V^o an associated fit of the V^o to the production vertex was accepted if the X^2-probability was greater than .01 . The production vertex fit was accepted if the condition

$$M^2 - 3\Delta(m^2) \leq m^2 \leq M^2 + 3\Delta(m^2)$$

was satisfied where

m^2 = square of missing mass at prodn. vertex with error $\Delta(m^2)$.

M = mass of the fitted missing particle (zero if no particle missing).

In the case of the final state $\bar{K}^o n\pi^+\pi^-$, the (missing mass)^2 distribution showed an asymmetry with an excess of events in the high mass end. This might be due to a contamination of events of the type $\bar{K}^o n\pi^+\pi^- + m\pi^o$, $m \geq 1$. Some contamination was also expected from events with Λs as already discussed. Since these events are likely to give wrong missing masses for the missing neutron, an additional missing mass cut was imposed, viz.

$$.56 \text{ Gev}^2 \leq (\text{missing mass})^2 \leq 1.20 \text{ Gev}^2.$$

The final cross sections were corrected for the effects of these selection criteria.

A small fraction of events cannot be identified uniquely even after checking the ionisations of the tracksfor consistency. In the case of events fitting a 4C hypothesis, i.e. those with four constraints at the production vertex fit, as well as an 1-C, the 4-C hypothesis has been accepted as true. The justification of this procedure is that because of measurement errors, a small missing momentum for an event with no missing particle can sometimes make it possible to accommodate one. It is much less likely for an event with a genuine missing particle to simulate one with nothing missing. In the case of 1-C 201 s the ambiguous events have been left out of general analysis. Cross-sections have been calculated by assuming half of these events to belong to the hypothesis concerned. These events were almost always ambiguous between two hypotheses out of $\bar{K}^{o}P\pi^{-}\pi^{o}$, $\bar{K}^{o}n\pi^{+}\pi^{-}$ and $\Lambda\,\pi^{+}\pi^{-}\pi^{o}$, which have comparable cross-sections. It is thus reasonable to assume that half of these events truly belong to the hypothesis in question. The corrections involved are

16.4 % for $\bar{K}^{o}n\pi^{+}\pi^{-}$

and 6.3 % for $\bar{K}^{o}P\pi^{-}\pi^{o}$.

The correction for ambiguity in the case of the final state $\bar{K}^{o}n$ has been found to be negligible.

Approximately 10 % of the events fitting the hypothesis $K^{-}P \rightarrow K^{-}P\pi^{+}\pi^{-}$ had two fits obtained by permuting tracks. In histograms, they have been plotted with weights of $\frac{1}{2}$. The no. of events with more than two fits was very small.

Accuracy of the experiment

The accuracy of momentum and angle measurements and, therefore, the overall resolution of the experiment depends on the setting errors. Fig. 4.10 shows the distribution of r.m.s. setting errors in track measurements. The modal value is 9μ on film, a part of which is contributed by multiple coulomb scattering of the track, turbulence in chamber liquid etc.. The measurement errors on vertices have been histogrammed in fig. 4.8. For a given vertex, the one with the smaller error of two vertex calculations has been used in these events. It is notable that for V^o apices these two methods have been used almost equally often, whereas for 201 production vertices it is almost always the one found by extrapolating the tracks. This indicates that with enough tracks available at a vertex, the vertex position is better determined by extrapolating the tracks than by direct measurements on the vertex.

An idea of the mass resolution is obtained from the width of the ideogram of the squared masses of the fitted $\overline{K}^o s$ i.e. the squares of the invariant masses of the two outgoing particles when they are assigned the pion mass. This ideogram is shown in fig. 4.9 together with the histogram and the former has a full width of .0164 Gev^2 at half height. The corresponding width in mass is about 16 Mev.

Cross-section calculations

The 'microbarn-equivalent' of an event can be determined by two independent methods as follows.

(a) By counting the total no. of beam track decays into three charged particles (i.e. into $\pi^-\pi^+\pi^-$, $\pi^-\pi^o$ and $\pi^-\pi^o\pi^o$ with $\pi^o \to \gamma e^+ e^-$).

(b) By normalising the total no. of observed interactions to the total cross section known from other experiments.

Both these methods have been used.

(a) Let T = mean life of K s at rest,

m = reat mass of K s,

P = beam momentum,

r = branching ratio of K^- decay into three charged particles (τ')

N = total no. of beam tracks with maximum length l each.

n_i = no. of events of a type with cross-section σ_i.

Then, probability of beam decay per cm. of track = $m/P.T = p_d$, say

and " of ith. type interaction " $= N_o.\rho.\sigma_i = p_i$, say,

where N_o = Avogadro's no. and ρ = density of liquid hydrogen.

Total prob. of decay or interaction on any track $= 1 - e^{-p.l}$

where $p = p_d + \Sigma p_i$. Then $n_i = (p_i/p)\, N\, (1 - e^{-p.l})$

and $n_{\tau'} = r\,(p_d/p)\, N\, (1 - e^{-p.l})$ = total no. of beam decays into three charged particles. Therefore,

$$n_i/n_{\tau'} = N_o.\rho.\sigma_i.P.T \,/\, r.m$$

or cross section per event $= \sigma_i/n_i = r.m \,/\, n_{\tau'}.\rho.N_o.P.T$

Using $r = .058 \pm .001$

$m = .4938$ Gev

$\rho = .0606 \pm .001$ gms/c.c.

$N_o = 6.02 \times 10^{23}$ per gm. mol.

$T = 1.23 \times 10^{-8}$ sec.

$n = 469$ in reg. A

and $P = 6.0$ Gev

$\sigma_i / n_i = .757 \pm .072$ microbarns per event.

(b) The total no. of events in the film used at I.C. = 33870. This number has been arrived at after estimating the no. of '000's (i.e. zero-prongs with no associated V^os) from the no. of '001's. A correction has been put in for the elastic scattering events with slow protons lost in scanning. With total $\sigma_{K^-P} = 24.0 \pm .3$mb.[10] $\sigma_i / n_i = .709 \pm .012$ μb/ev. Correcting for an average π-contamination of 6%, $\sigma_i / n_i = .751 \pm .013$ μb/ev.

Using a weighted mean of the two values of the microbarn - equivalent and the ratio of numbers of events processed through kinematics by I.C. alone and the collaboration, the values for the total sample of events becomes

201 s	.181 ± .005	μb/event
400 s	1.06 ± .08	"
001 s	.50 ± .06	" .

The corrected total cross sections for the final states used in this work are listed in table 4.2. The figures quoted in this table have been corrected for pion-contamination. For the channels where a strange particle decay is seen, it is adequate to use the corrected μb-equivalent. For four-prong events this is less simple since events of the type $\pi^- P \rightarrow P\pi^-\pi^+\pi^-$ are very likely

to fit the hypothesis $K^-P \to K^-P\pi^+\pi^-$. In the analysis of the latter final state, only run F film was used. The pion contamination of ~ 3.5 % is not expected to produce any appreciable distortion in the physics involved. The cross section for $K^-P \to K^-P\pi^+\pi^-$ can be found in the following way.

If $x = \sigma_{K^-P \to K^-P\pi^+\pi^-}$, $y = \sigma_{\pi^-P \to \pi^-P\pi^+\pi^-}$

p = average pion contamination and, using corrected μb - eq.,

z = observed cross section for $\left(\frac{\pi}{K}\right)^-P \to \left(\frac{\pi}{K}\right)^-P\pi^+\pi^-$

then $x = z - \frac{p \cdot y}{1-p}$. The value of y is known at beam momenta of 4, 7 and 10 Gev from ref.(11). The quoted cross section for $K^-P \to K^-P\pi^+\pi^-$ has been corrected by using an interpolated value of y = 1.6 mb.

Table 4.2

Final state	cross-section(mb)
$\bar{K}^o n$	.0985 ± .025
$\bar{K}^o P\pi^-$	.310 ± .045
$\bar{K}^o n\pi^+\pi^-$	.605 ± .070
$\bar{K}^o P\pi^-\pi^o$	.878 ± .105
$K^-P\pi^+\pi^-$	.594 ± .110

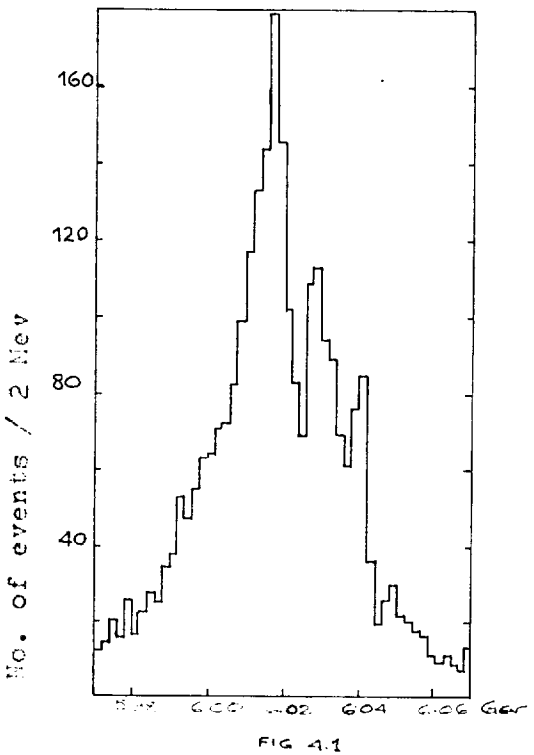

FIG 4.1

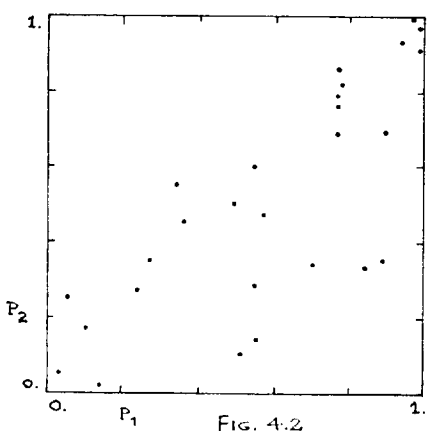

FIG. 4.2

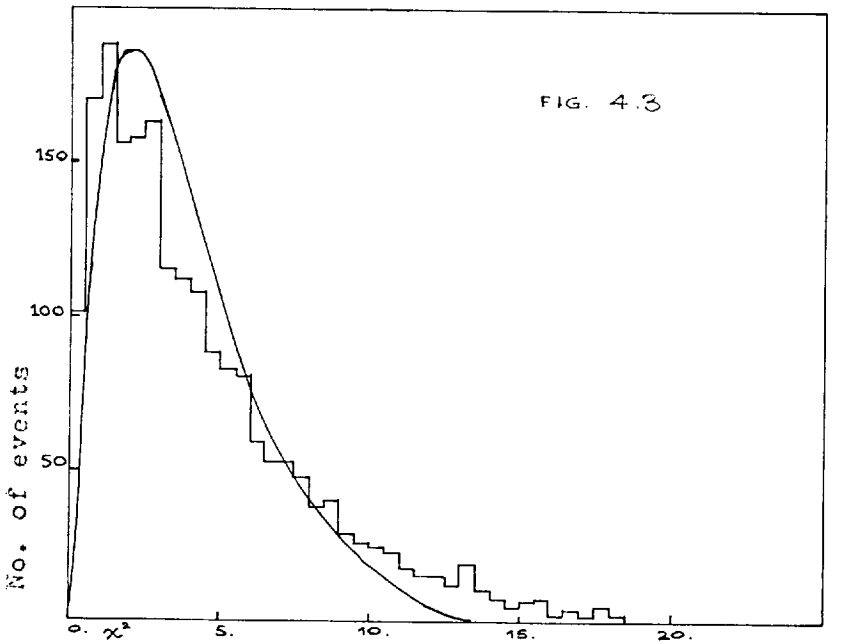

FIG. 4.3

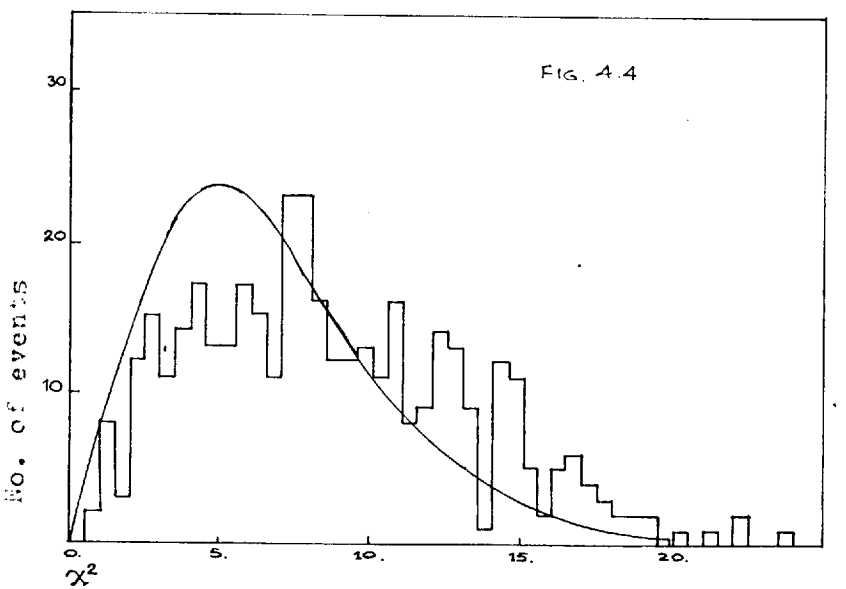

FIG. 4.4

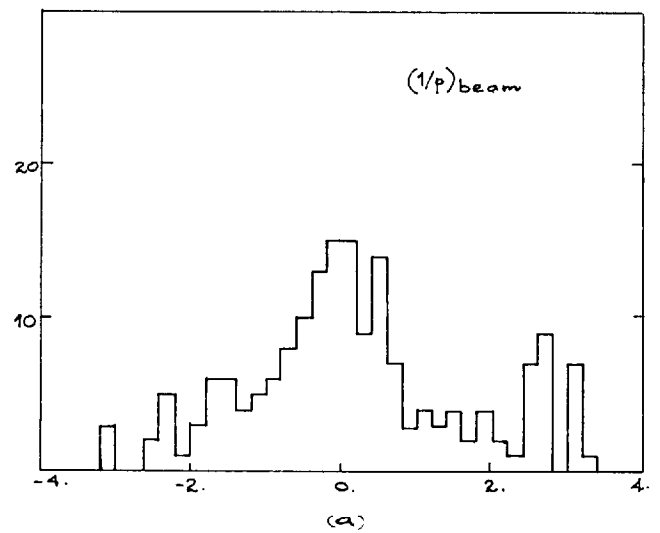
(1/p)beam
20
10
-4.
-2.
0.
2.
4.

(a)

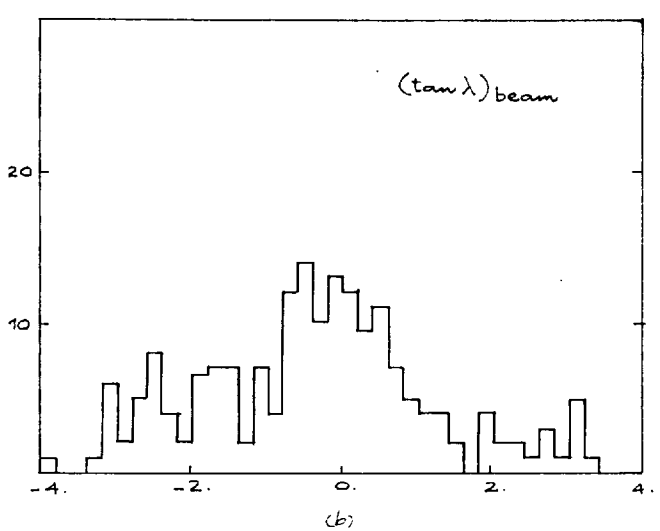
(tan λ) beam
20
10
-4.
-2.
0.
2.
4.

(b)

FIG. 4.5

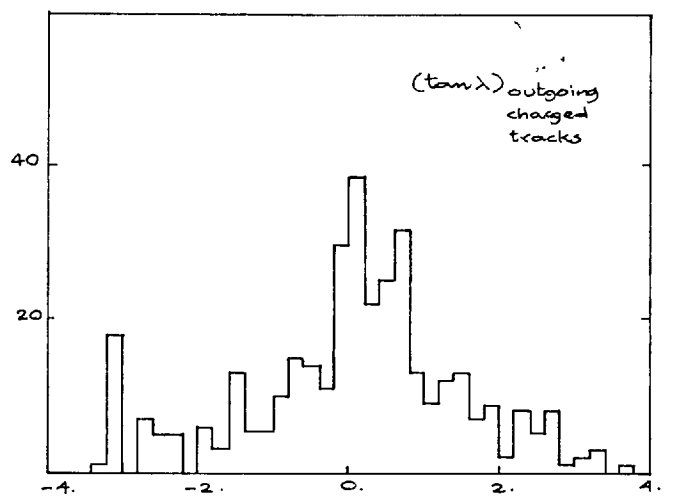
(tan λ) outgoing charged tracks
40
20
-4.
-2.
0.
2.
4.

(c)

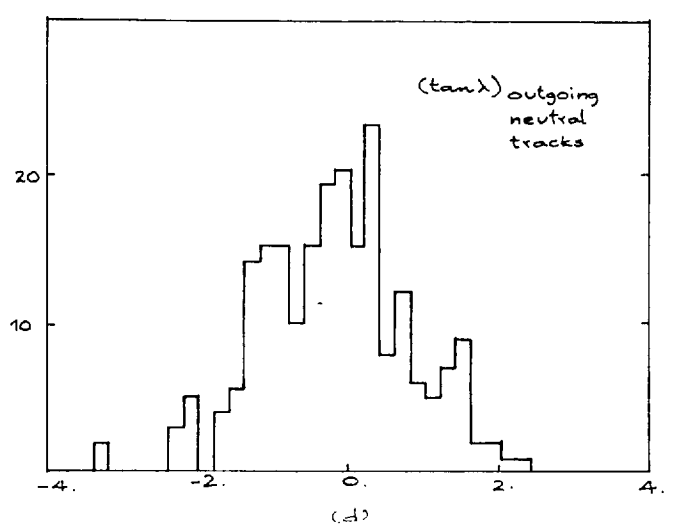
(tan λ) outgoing neutral tracks
20
10
-4.
-2.
0.
2.
4.

(d)

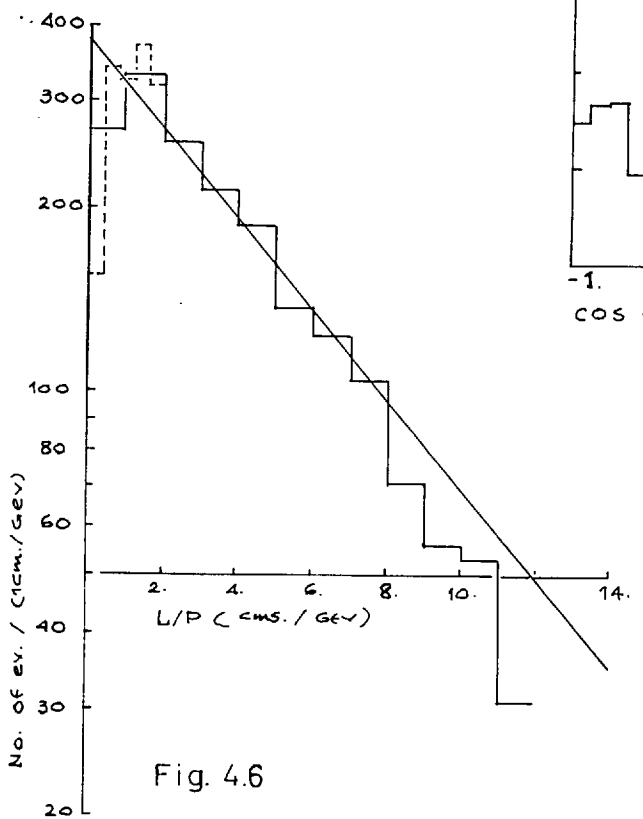
400
300
200
100
80
60
40
30
20
No. of ev. / (1cm./Gev)
2.
4.
6.
8.
10.
14.
L/P (cms. / Gev)

Fig. 4.6

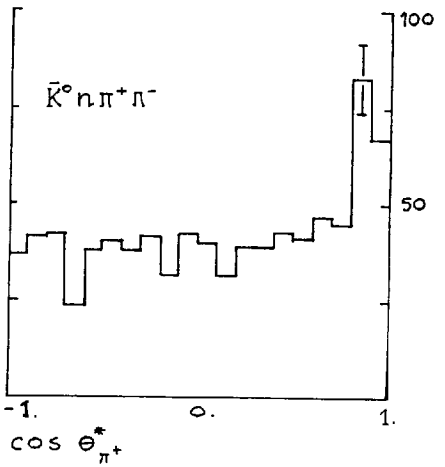
$\bar{K}^0 n\pi^+\pi^-$
100
50
-1.
0.
1.
$\cos\theta^*_{\pi^+}$

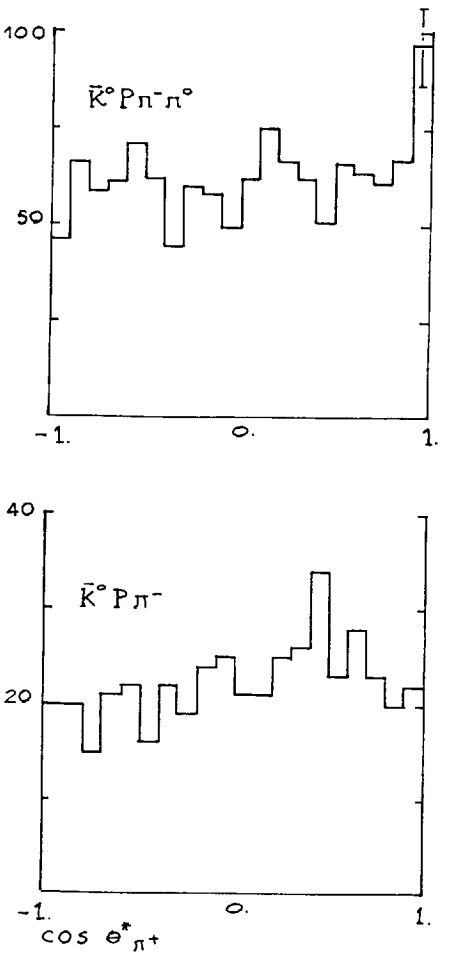
No. of events
100
50
$\bar{K}^0 P\pi^-\pi^0$
-1.
0.
1.
40
20
$\bar{K}^0 P\pi^-$
-1.
0.
1.
$\cos\theta^*_{\pi^+}$

Fig. 4.7

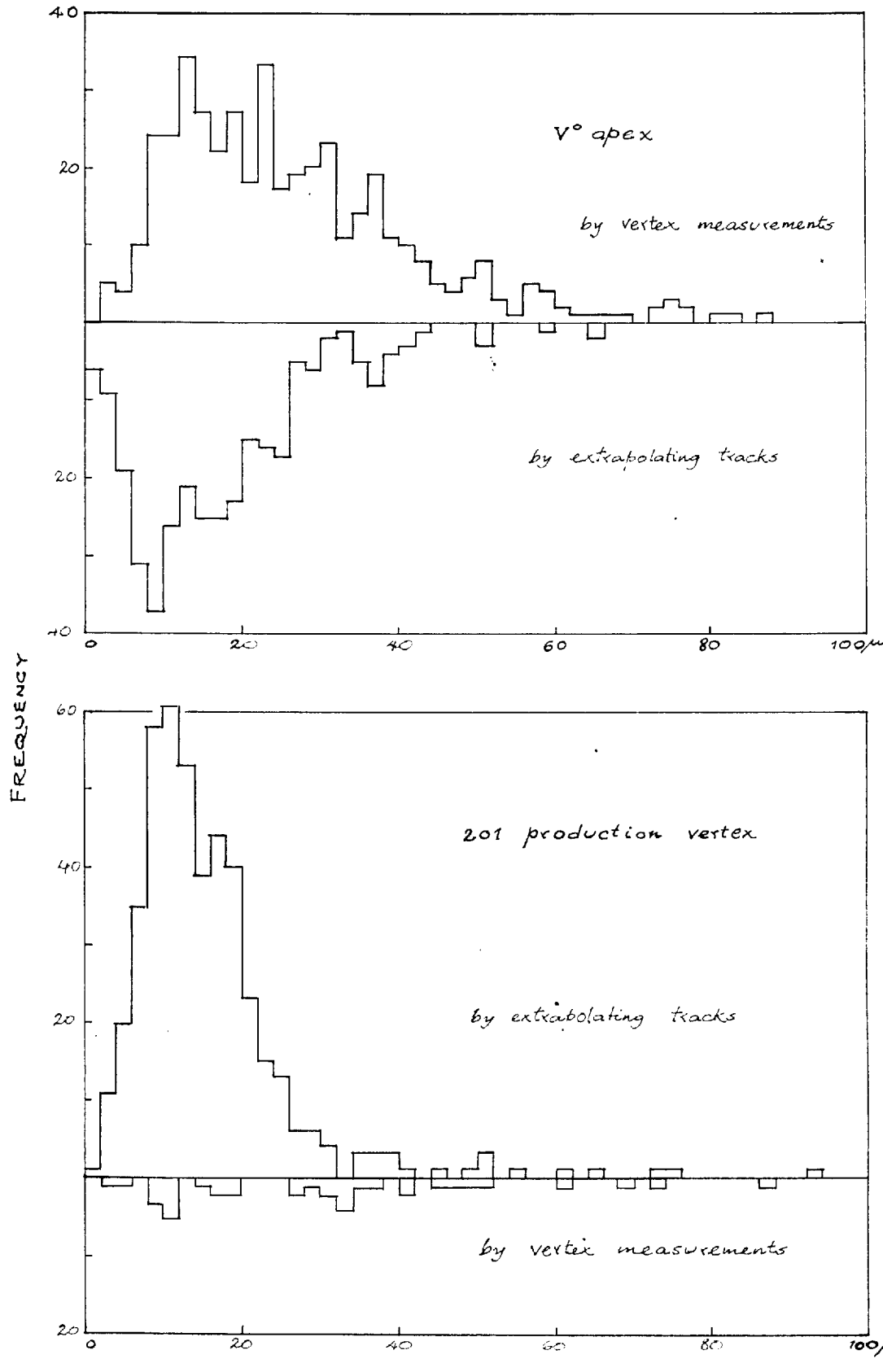
40
20
V° apex
by vertex measurements
20
by extrapolating tracks
40
0
20
40
60
80
100μ
FREQUENCY
60
40
20
201 production vertex
by extrapolating tracks
by vertex measurements
20
0
20
40
60
80
100μ

FIG. 4.8

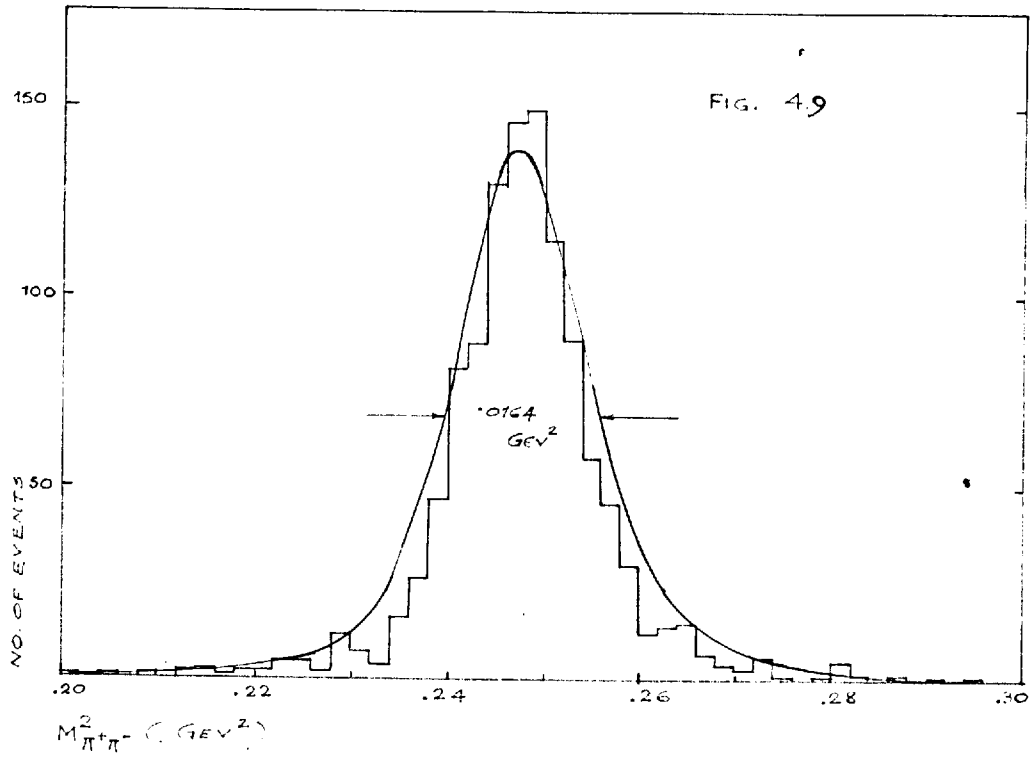

FIG. 4.9

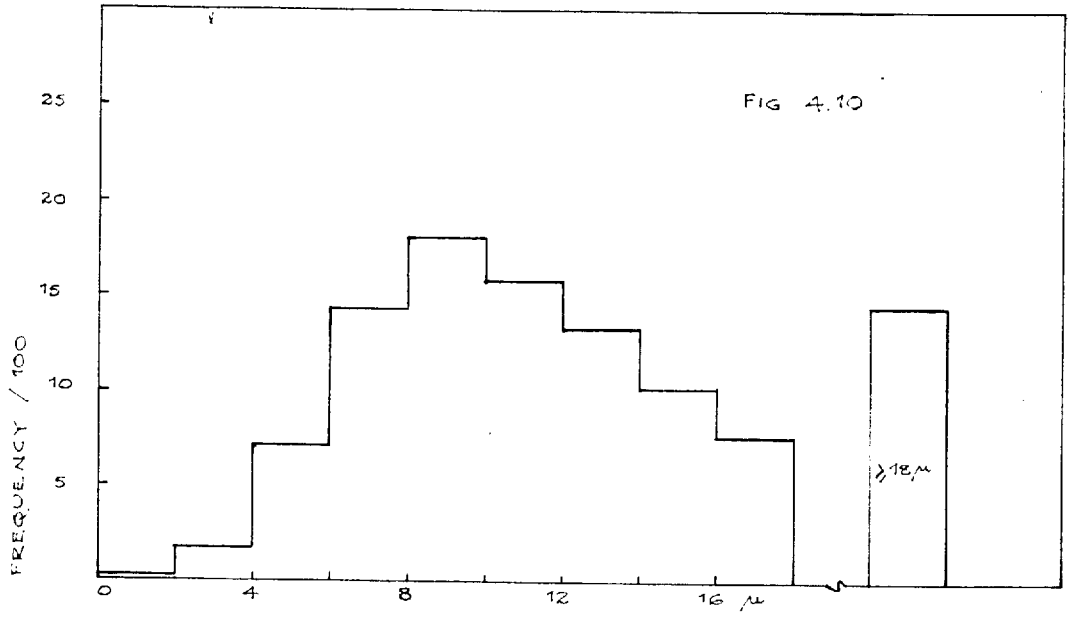

FIG 4.10

Chapter 5 Theoretical methods

Effective mass and four-momentum transfer

We denote the energy-momentum four-vector of the beam(K), target(P) and the ith. outgoing particle by P, Q and p_i respectively. For a group of outgoing particles, the effective mass and the four-momentum transfer to them from one of the two incoming particles are invariant under Lorentz transformations and are useful quantities to study elementary particle reactions. They are defined as follows:

$$M^2 = (\Sigma p_i^o)^2 - (\Sigma \underline{p}_i)^2 = (\Sigma p_i)^2$$

$$\Delta^2 \text{ or } t = (\sum_i p_i^o - \frac{P^o}{Q^o})^2 - (\sum_i \underline{p}_i - \frac{\underline{P}}{\underline{Q}})^2 = (\sum_i p_i - \frac{P}{Q})^2$$

In the definition of Δ^2 the choice of P or Q depends on whether the particular combination is assigned to the meson or baryon vertex in a Feynmann diagram as shown in fig. 5.1. In the case of K^-P interactions a mesonic particle combination would be normally assumed to be produced at the top vertex 1 and a baryonic combination at the bottom vertex 2. The vertex assignments are reversed in the case of a baryon-exchange process.

The Breit-Wigner shape

In a statistical model, an effective mass is expected to be distributed according to the Lorentz invariant phase space. We

represent the ordinate of this distribution by L(m). In certain cases this phase space is known to distorted by peripheralism or otherwise, in which case L(m) can be taken as the appropriately modified phase space. With n resonances contributing fractions r_i, i = 1,n, of the total channel the expected distribution Y(m) is given by

$$Y(m) = L(m).(1 - \sum_i r_i) + \sum_i r_i . \frac{L(m) . B_i(m)}{\int_{m_{min.}}^{m_{max.}} L(m).B_i(m)\, dm}$$

where $m_{min.}$ and $m_{max.}$ are the kinematic limit for the effective mass in consideration and

$$B(m) = \frac{m.m_o.\Gamma(m) / \pi}{(m-m_o)^2 + m_o^2 \Gamma(m)^2} \quad (18),$$

$B_i(m)$ being its value for the ith. resonance. $\Gamma(m)$, the width of the resonance is a slowly varying function of the mass and the variation arises from the angular momentum barrier. For a two body decay with the final state orbital angular momentum l, the expression for Γ is

$$\Gamma(m) = \Gamma_o . (q/q_o)^{2l+1},$$

q being the resonance c.m. momentum of each of the decay products and q_o, Γ_o being the values at $m = m_o$.

The expression for Y(m) quoted above has been used in this experiment to fit Breit-Wigner shapes to experimental mass distributions. The integration is conveniently done by a numerical method.

Peripheral and multiperipheral models

The general feature of two-body processes that the particles in the final state are produced with a small four-momentum transfer has led to the one-particle-exchange model. The unmodified one-particle-exchange model fails to explain the distribution of the differential cross-section but it is accepted in principle and one tries to explain two-body processes with the Feynmann diagram shown in fig. 5.1 . All known particles can play the role of the exchanged particle. In any particular process, conservation of charge, angular momentum, parity and other quantum numbers at the two vertices may limit the possibilities. One can go further and use the decay angular distributions of any resonances to deduce the nature of the exchanged particle.

Apart from elastic scattering, the cross-sections for two-body reactions decrease as the total energy goes up. At the energy of the present experiment, they form only a small part of the total cross-section. Three - body states contribute substantially. The double-peripheral model[43], a special case of the multiperi - pheral model[44] treats them as shown in fig. 5.2 . In general, the consequence of such a process is a low four-momentum transfer from A to C and B to E. The various conservation laws still hold at the vertices 1 , 2 and 3 and the exchanged particles e_1 and e_2 can be particles like mesons π , K etc. or the vacuum trajectory. This implies, for example, that the particles e_1 and

B may scatter elastically. Obviously, a_1 and D or B and E would be the same particles in that case. This process, known as 'Deck mechanism'[28] has received a good deal of theoretical attention.

The absorption model

The absorption model provides a natural explanation for the sharp fall-off in the t-distribution at high energies. The lower partial waves produce more central collisions and for these the two-body processes are suppressed by competition with many other open inelastic channels. The total cross-section for the two-body processes are, therefore, reduced and since it is made up mainly by high partial waves, these processes are more peripheral than otherwise.

The quantitative formulation is described in refs.(12-14). In principle, the initial and final state wave functions are approximated by those of an optical model potential. The absorption due to competing inelastic channels is simulated by the imaginary part of this wave function. These can be described in terms of elastic scattering in the initial and final states and the optical model potential is replaced by elastic scattering. The effect of the absorption is to introduce the elastic scattering phase shift into the wave functions.

Apart from modifying the t-distribution, absorption alters the predictions on the density matrix elements. As a result of the initial and final state interactions, the states observed in the laboratory are not the same as those of the main two-body reaction. The density matrix elements are, therefore, evaluated in the wrong frame of reference with respect to the wrong direction.

In the case of K^-P charge-exchange scattering, the particles that can be exchanged are the ρ and the A_2. The differential cross-section for ρ-exchange alone can be calculated with the absorption model without any free parameters. The initial and final state elastic scattering parameters and the $KK\rho$ and $NN\rho$ coupling constants are known.

In the case of $K^-P \to K^{*-}_{890} P$ the quantities

$$\xi = \frac{f_{KK^*v} \left(G^v_{NNv} + G^t_{NNv} \right)}{2\, G_{NN\pi} \cdot g_{KK^*\pi}}$$

$$\eta = \frac{f_{KK^*v} \cdot G^t_{NNv}}{g_{KK^*\pi} \cdot G_{NN\pi}}$$

are not exactly known and are free parameters to be input. The initial state elastic scattering is known from experimental data. At small angles the elastic scattering amplitude is approximated by

$$f_{el}(\theta) \simeq -iq \int_{b=0}^{\infty} b.J_o(\Delta b) \left(e^{2i\delta(b)} - 1\right) db$$

where b = impact parameter. Assuming that f_{el} is purely imaginary and $\frac{d\sigma}{dt}$ falls off exponentially, $e^{2i\delta(b)}$ can be written in the

form $1 - C_i\, e^{-\gamma_i (x-\frac{1}{2})^2}$ where $C_i = \frac{\sigma_{total}}{4\pi A}$ and $\gamma_i = 1/2Aq^2$ with q = c.m.momentum and A = slope parameter appearing in $\frac{d\sigma}{dt} \propto e^{At}$. C_f and γ_f are similarly defined. They are unknown and the values used are $C_f = 1$ and $\gamma_f = .75\gamma_i$ as prescribed in ref.(12).

The Regge - pole theory

In the Regge-pole theory of elementary particle interactions the exchanged particles are replaced by Regge-poles, which have a continuously variable spin $\alpha(t)$ depending on t i.e. invariant mass squared. The Regge-poles manifest themselves as physical particles when their trajectories i.e. $t - \alpha(t)$ curves cross either even or odd integral values of α.

The differential cross-section for a 0^- meson - nucleon collision is given by(15)

$$\frac{d\sigma}{dt}(s,t) = \frac{1}{\pi s}\left(\frac{m_N}{4k}\right)^2 \left(1-\frac{t}{4m_N^2}\right)\left|A\right|^2 + \frac{t}{4m_N^2}\left(s - \frac{s+p^2}{\frac{t}{4m_N^2}}\right)\left|B\right|^2$$

where s = (c.m.energy)^2

p = lab. momentum of incident meson

k = c.m. momentum of meson or nucleon

m_N = nucleon mass.

Each pole exchanged contributes to the helicity(of nucleon) - flip amplitude B and the non-flip amplitude A terms of the form

$$A_i = -C_i \frac{\exp(-\pi\alpha_i) \pm 1}{\sin(\pi\alpha_i)} \left(\frac{E}{E_o}\right)^{\alpha_i}$$

$$B_i = -D_i \frac{\exp(-\pi\alpha_i) \pm 1}{\sin(\pi\alpha_i)} \left(\frac{E}{E_o}\right)^{\alpha_i - 1}$$

with E = total meson lab. energy

E_o = arbitrary dimensional parameter.

K^-P charge exchange scattering has been treated by Rarita and Phillips [15] and Roy [16]. In the former approach, the 'residue functions' C_i and D_i are expressed as strongly t-dependent functions. Although the trajectories used (ρ and A_2) are determined from $\pi^-P \to \pi^o n$ and $\pi^-P \to \eta^o n$ data, the data-fitting for $K^-P \to \bar{K}^o n$ is too unconstrained. The latter method considers ρ - exchange alone and uses t-independent residue functions apart from the threshold factors ($2\alpha + 1$). The differential cross-section can be shown to be equal to

$$\frac{C(t)}{16\pi}(2\alpha+1)^2\left(1+\tan^2\frac{\pi\alpha}{2}\right)\left(\frac{s-(m_N^2+m_K^2)}{2m_N m_K}\right)^{2\alpha-2}$$

where $C(t) = \left(\frac{2\pi\varepsilon}{3}\gamma_{\rho NN}\cdot\gamma_{\rho KK}\right)^2 - \frac{t}{4m_N^2}\left(\frac{4\pi}{3}\varepsilon m_N \mu_{\rho NN}\cdot\gamma_{\rho KK}\right)^2$

and ε = slope of the trajectory at the ρ mass.

This formula predicts the differential cross section absolutely but approximately since the coupling constants are not exactly known.

The Regge-pole exchange model gives rise to either a 'nonsense state' or to a 'nonsense coupling' when the exchanged

trajectory passes through $\alpha = 0$. The corresponding contribution to the differential cross-section becomes zero in that case and a dip in the total $\frac{d\sigma}{dt}$ is expected at that point. For the ρ-trajectory, as for example, this occurs at $t \simeq -0.6$ Gev^2 (17).

The spin density matrix

A resonance of spin j is, in general, produced in a mixture of pure spin states, each of which is of the form $\Sigma_m a_m |j,m>$. If p^i = contribution of the ith. pure spin state and if we define $\rho_{mm'} = \Sigma_i p^i a^i_m a^i_{m'}$, then the expectation value of any physical variable can be written as

$$<Q> = \Sigma\Sigma_{m\,m'} \rho_{mm'} Q_{mm'}, \quad Q_{mm'} = <j,m'|Q|j,m>$$

The element $\rho_{mm'}$ of a spin density matrix can be interpreted as the weight attached to the contribution to the observed value of the physical variable by the overlap of the states $|j,m>$ and $|j,m'>$ of the resonance.

The decay angular distributions of resonances can be expressed in terms of the density matrix elements. The expressions for some commonly observed decays are quoted below.

(a) 1^- meson -> two 0^- mesons

$$W(\theta,\varphi) = \frac{3}{4\pi}\left[\rho_{11}\sin^2\theta + (1-2\rho_{11})\cos^2\theta - \rho_{1,-1}\sin^2\theta\cos 2\varphi - 2\,\mathrm{Re}\rho_{10}\sin 2\theta\cos\varphi\right]$$

(b) $3/2^+$ baryon $\rightarrow$ $1/2^+$ baryon + 0^- meson

$$W(\theta,\varphi) = [\rho_{33}\sin^2\theta + (\tfrac{1}{2} - \rho_{33})(\tfrac{1}{3} + \cos^2\theta) - \frac{2}{\sqrt{3}}\mathrm{Re}\rho_{3,-1}\sin^2\theta\cos 2\varphi - \frac{2}{\sqrt{3}}\mathrm{Re}\rho_{31}\sin 2\theta\cos\varphi]$$

(c) 2^+ meson -> two 0^- mesons

$$W(\theta,\varphi) = \frac{15}{16\pi}[3\rho_{00}(\cos^2\theta - \tfrac{1}{3})^2 + 4\sin^2\theta\cos^2\theta(\frac{1-\rho_{00}}{2} - \rho_{1,-1}\cos 2\varphi)]$$

In the case of 2^+ meson (c), it has been assumed that the resonance is produced by the exchange of a pseudoscalar or vector meson only. This restricts the matrix elements ρ_{2m}, ρ_{m2} and $\mathrm{Re}\rho_{10}$ to be zero.

It is possible to determine many of the elements in the spin density matrices by fitting the theoretical angular distri - butions to the experimental data. In the present experiment, the fitting has been done by maximum - likelihood method. An alternative method is to express the density matrix elements in terms of the expected values of some functions of θ and φ, which are then calculated from the data. The formulae used are given below.

case(a) $\rho_{00} = \frac{1}{2}(5\langle\cos^2\theta\rangle - 1)$

$\rho_{1,-1} = -5/4 \cdot \langle\sin^2\theta\cos 2\varphi\rangle$

$\mathrm{Re}\rho_{10} = -5/4/2 \cdot \langle\sin 2\theta\cos\varphi\rangle$

case(b) $\rho_{33} = 1/8\,(15\langle\cos^2\theta\rangle + 7)$

$\mathrm{Re}\rho_{3,-1} = -5/3/8 \cdot \langle\sin^2\theta\cos 2\varphi\rangle$

$\mathrm{Re}\rho_{3,1} = -5/3/8 \cdot \langle\sin 2\theta\cos\varphi\rangle$

case(c) $\rho_{00} = 21/2\,(\langle\cos^2\theta\rangle - 3/7)$

$\rho_{1,-1} = -7/4 \cdot \langle\sin^2\theta\cos 2\varphi\rangle$.

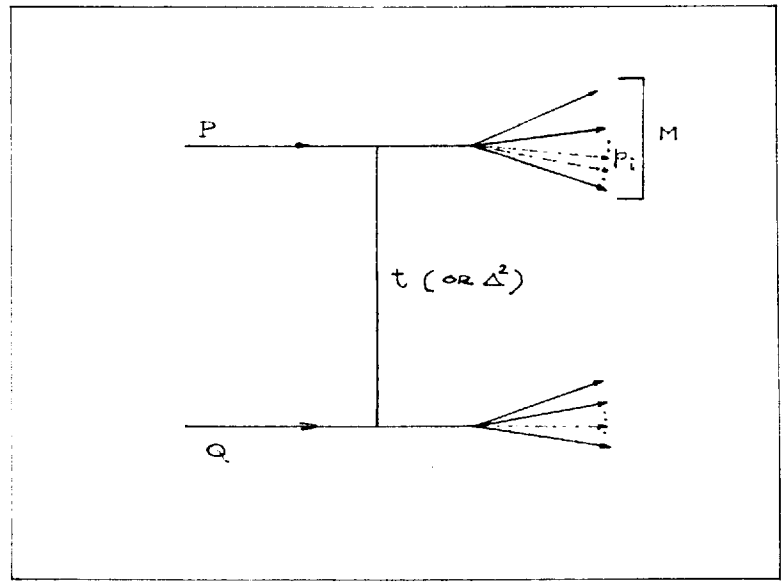

FIG. 5.1

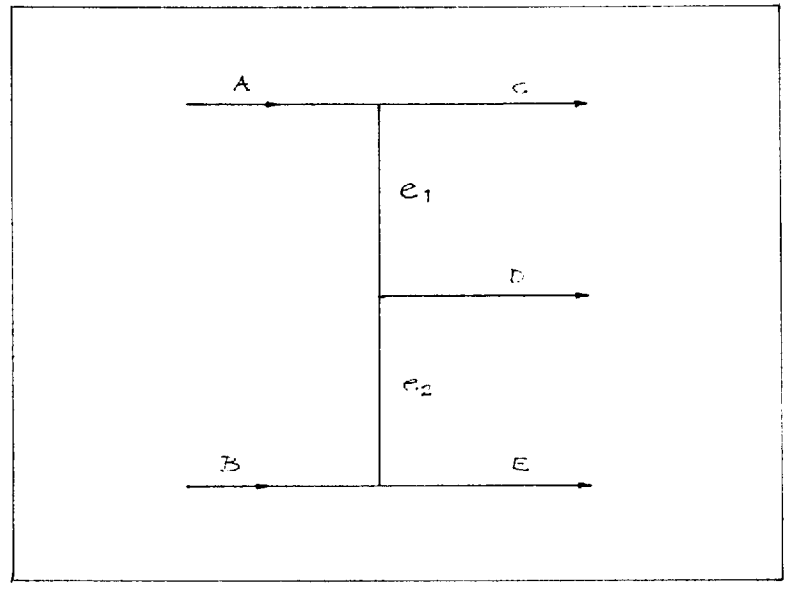

FIG. 5.2

Chapter 6 — The final states $\bar{K}^0 n$ and $\bar{K}^0 \pi^- P$

Charge - exchange scattering

Events of the topology '001' were measured on about a third of the film and 43 gave satisfactory fit to the hypothesis $K^- P \rightarrow \bar{K}^0 n$. The observed total cross-section of 99 ± 25 μb agrees fairly well with the results of spark chamber experiments by Astbury et. al.[20] as shown in fig. 6.1 . The differential cross-section is shown in fig. 6.2. The spark chamber experiments mentioned above have observed a peak in the differential cross-section at $t \simeq -0.1$ Gev^2 . Our data show a similar effect although with much lower statistical significance.

The absorption model for $K^- P$ charge exchange scattering with ρ exchange alone gives a cross-section higher than observed ones by a factor of ~ 10 . The Regge-pole theory can provide a qualitative explanation of the dip in $\frac{d\sigma}{dt}$ near $t = 0$ by postulating a large helicity - flip amplitude whose contribution vanishes at $t \simeq 0$. The solid line drawn in fig.6.2 is the prediction by a Regge-pole model [16] with the ρ - trajectory approximated by $\alpha(t) = .6 + .6\, t$. The cross-section is correctly predicted since only an approximate agreement is expected. However, the dip at $t = 0$ is not reproduced by this theory and is

attributed to possible fine-structure in the residue functions or to non-linear t - dependence of $\alpha(t)$. The data are obviously too poor to show any secondary dips in the t - distribution.

The final state $\bar{K}^{o}\pi^{-}P$

The sample used for this final state consists of 416 events where a V^{o} is seen. The kinematic fit to the production vertex has four constraints and the proton is identifiable in about 99 % of cases. The sample can be considered to be 100% pure for all practical purposes.

A Dalitz plot for the state is shown in fig.6.3 and the mass plots for the $\bar{K}^{o}\pi^{-}$ and $P\pi^{-}$ combinations in figs. 6.4. The $\bar{K}^{o}\pi^{-}$ effective mass shows two prominent spikes corresponding to the K^{*-}_{890} and K^{*-}_{1400} resonances. The solid line drawn on the $\bar{K}^{o}\pi^{-}$ mass histogram is a maximum likelihood fit to the data with Lor.inv. phase space plus the two K* resonances. The fitted values of the masses and widths of the K*s are given in table 7.2. Apart from the two K*s, $N^{*o}_{3,3}$ is the only resonance noticeable. The cross-sections for the different channels are listed in table 6.1. The cross-sections quoted are for $K^{*-} \rightarrow \bar{K}^{o}\pi^{-}$ and $N^{*o} \rightarrow P\pi^{-}$ decays alone. The channel $\bar{K}^{o}N^{*o}$ is very weak and has a large background. No detailed study is, therefore, possible. The two-body states $K^{*-}_{890}P$ and $K^{*-}_{1400}P$ will be

discussed with a study of the non-resonant $\bar{K}^o\pi^-P$ events.

Table 6.1

Channel	Cross-section (mb.)
$K^{*-}_{890}P$	.126 ± .025
$K^{*-}_{1400}P$	.048 ± .012
$\bar{K}^oN^{*o}$	.012 ± .005

$K^{*-}_{890}P$

Events used for this channel are those with $0.80\ \text{Gev} \leq M(\bar{K}^o\pi^-) \leq 0.98\ \text{Gev}$. The estimated background of non-resonant events is $\sim 10\%$. The t-distribution for these events, shown in fig. 6.5 shows a peaking in the low-t end it is clear that the K* is produced in a peripheral process. In a one-meson-exchange model, the particles that can be exchanged are

Pseudoscalar mesons π^o, η^o or X^o

Vector mesons ρ^o, ω or φ

excluding heavier candidates like the A_2 and f^o. A common technique for studying the nature of the exchanged particle is the density matrix analysis described in ch. 5. The elements of the K* density matrix, ρ_{oo}, $\rho_{1,-1}$ and $\text{Re}\,\rho_{10}$, are listed in table 6.2. The numbers appearing on the top lines are the results of moments-method calculations, while those on the bottom lines are obtained by Malik.

Table 6.2

	t <0.2	0.2< t <0.4	t > 0.4	all events
ρ_{00}	.215±.078	.148±.099	.030±.092	.130±.050
	.192±.056	.116±.068	-.116±.078	.116±.035
ρ_{11}	.393±.039	.426±.050	.485±.046	.435±.026
	.404±.028	.442±.034	.558±.039	.442±.017
$\rho_{1,-1}$	.456±.062	.467±.081	.356±.105	.437±.045
	.483±.040	.542±.039	.373±.080	.394±.026
$Re\ \rho_{10}$	.040±.036	.011±.042	.037±.051	.017±.031
	.098±.034	.052±.047	.034±.032	.020±.026

The fitted angular distributions for all events in the sample are shown in fig. 6.6 together with the experimental histograms.

If we assume ρ_{00} to be a guide to the amount of vector meson exchange in the process $K^-P \rightarrow K^{*-}P$, this proportion is about 88 %. It is not possible to infer from this experiment alone whether this particle is mainly isotopic singlet (i.e. ω or φ) or triplet. (i.e.ρ). However, the process $K^-P \rightarrow \bar{K}^{*o}n$ can occur only via isovector exchange and the ratio

$$\sigma_{\bar{K}^{*o}n} / \sigma_{K^{*-}p} \text{ (isovector exchange only)} = 4 .$$

The channel $\bar{K}^{*o}n$ has been studied in K^-P experiments at other energies and some results are quoted in table 6.3.

Table 6.3

Beam mom.	$\sigma_{\bar{K}^{*o}n}$	Ref.
4.1 Gev	514±75 μb	21
5.5 "	352±53 "	21
10.1 "	64± 9 "	22

The interpolated value for the cross-section is ., for a beam momentum of 6 Gev, 320 ± 50 μb . Therefore, the contribution to the total $\sigma_{K^{*-}P}$ of 189 ± 37 μb (correcting for the $K^-\pi^o$ decay of the K^{*-}) from isovector exchange is 80 ± 12 μb . Since the rest is isoscalar, it is natural to assume that it is made up almost entirely of ω or φ exchange .

The distribution of the four-momentum transfer shows characteristics of vector - exchange as well. There is a signi - ficant drop in the value of the differential cross-section near t = 0 which is explained by the fact that the vector exchange contribution vanishes at zero production angle. In fig. 6.5 the observed t - distribution is compared with the results of absorption model calculations done with the computer programme mentioned in ref.(23). The elastic scattering slope parameter A is obtained by interpolating between results from refs.(24-26). The total K^-P cross-section is the same as that used in ch. 4. The value of η has been kept fixed at zero as for ω exchange (45) $G_T \ll G_V$. It has been found that values of ξ equal to

.50 - .75 give a total cross-section of the right order although the shape of the distribution is not correctly reproduced. The predicted values of the K^{*-} spin density matrix elements with the same values of η and ξ are shown against the data in fig.6.8. The agreement is satisfactory and specially the trend of variation of ρ_{oo} with increasing (-t) is consistent with the data.

There is a suggestion of a dip in the t-distribution nearabout $t = -.6$ Gev^2 but with the available statistics no statement of any statistical significance can be made.

Figs. 6.9-10 compare the total cross-section and the K^{*-} density matrix elements obtained in this experiment with those in others. The general falling-off of the cross-section with increasing beam momentum can be clearly observed. The density matrix elements seem to indicate a steadily increasing proportion of vector meson exchange in this channel.

K^{*-}_{1400} P

The K^{*}_{1400} peak in fig. 6.3 contains 62 events between 1.36 and 1.52 Gev. This sample is expected to be about 70 % pure, the rest being non-resonant background. The t-distribution of these events is shown in fig.6.11.

As in the case of K^{*}_{890}, we study the exchange mechanism for K^{*}_{1400} production with the help of its spin density matrix assuming the K^{*}_{1400} to be a $J^P = 2^+$ object. The contribution from

any spin two particle exchange can be neglected unless the decay-angular distribution demands the inclusion of terms involving Y_2^m. Neglecting also the effects of absorption, we expect in the case of pure 0^- exchange, $\rho_{oo}=1$, $\rho_{1,-1}=.5$.

Fig. 6.7 exhibits the $\cos\theta$ and φ distributions for the K^*_{1400} decay. The fitted θ distribution has been superposed on the histogram while the curves shown along with the $\cos\theta$ distribution represent the expected ones for the extreme cases of pure pseudoscalar (a) and pure vector(b) exchange. The values of the density matrix elements obtained from the decay angular distribution are

	By moments	By Halik
ρ_{oo}	$.97 \pm .42$	.44
$\rho_{1,-1}$	$.24 \pm .07$	.20

The value of ρ_{oo} itself does not give much information because of the large uncertainty. This arises because of the inherent nature of the $\cos\theta$ distribution which is too insensitive in general features to the value of ρ_{oo}. However, the $\cos\theta$ distribution does not demand the inclusion of any spin 2 exchange. The value of $\rho_{1,-1}$ is significantly different from zero and hence indicates some vector exchange.

The identification of the K^*_{1400} as a 2^+ object is not, to date, established beyond doubt and one cannot rule out the possibility of $J^P = 1^-$. An attempt to fit the observed decay angular

distribution to the theoretical one for an 1^- particle gives the following values for the density matrix elements:

$$\rho_{oo} = .80 \pm .10$$

$$\rho_{1,-1} = .17 \pm .06$$

$$\mathrm{Re}\,\rho_{10} = -.02 \pm .05$$

The fitted distributions for the two cases are shown in fig.6.14. for the $\cos\theta$ along with the folded histogram. Quite clearly, it is not possible to find the spin and parity of the K^*_{1400} by judging the quality of fit. If the K^*_{1400} were assumed to be an 1^- meson, the value of ρ_{oo} would indicate almost pure pseudo-scalar exchange and no $\cos 2\varphi$ dependence of the φ-distribution would be expected. The value of $\rho_{1,-1}$ is not very high, so that it does not provide a reliable check on the spin-parity assignment.

The variation of the $K^-P \rightarrow K^{*-}_{1400}\,P$ cross-section for different beam momenta has been shown in fig. 6.12. It shows the same trend of falling off for increasing beam momentum as in the case of $K^{*-}_{890}\,P$. The results of some of the latest experiments attempting to determine the J^P of the K^*_{1400} are summarised in fig. 6.15. The quantities plotted are the probabilities of obtaining a X^2 equal to or greater than the observed X^2 for the best fits for 1^- and 2^+ assignments of J^P.

The decay angular distributions of the K^*_{890} and the K^*_{1400}, together with a very peripheral production of these

resonances produce an interesting outcome. Because of the peripheralism, the incoming beam direction in the K* centre of mass is practically the same as that in the overall centre of mass. The K^{*-}_{890} tends to decay equatorially and gives rise to medium mass values for the $P\pi^-$ combination. The K^{*-}_{1400} decays with strong forward-backward peaking with respect to the beam direction in its own rest frame and thus produces either low or high $P\pi^-$ masses. This feature is clearly seen on the Dalitz-plot in fig. 6.3 and also explains why apparently some N^{*o} events are associated with the K^{*-}_{1400}.

The non-resonant events

If the K* events are removed, the rest of the $\bar{K}^o\pi^-P$ events provides a sample of three body states with a small contamination from N^{*o} events. Fig. 6.13 shows the $P_l - P_t$ (i.e. longitudinal vs. transverse momentum in the overall centre of mass) for the individual particles. In fig. 6.13(a) the K*s have been left in and they produce distinct arcs in the proton P_l-P_t diagram. Apart from these, it can be seen that the $\bar{K}^o$ and the proton tend to continue in the directions of the K^- and the target proton respectively while the π^- is comparatively isotropic. This fits a double peripheral model (fig. 5.2) where $C=\bar{K}^o$, $D=\pi^-$ and $E=P$. The exchanged particle e_1 can be assumed to be ρ alone

with $e_2 = \pi^o, \eta^o, \omega^o$ or φ^o. However, since the particle C in this case is not a resonance with non-zero spin, the total vector-exchange in its production cannot be verified by density matrix analysis.

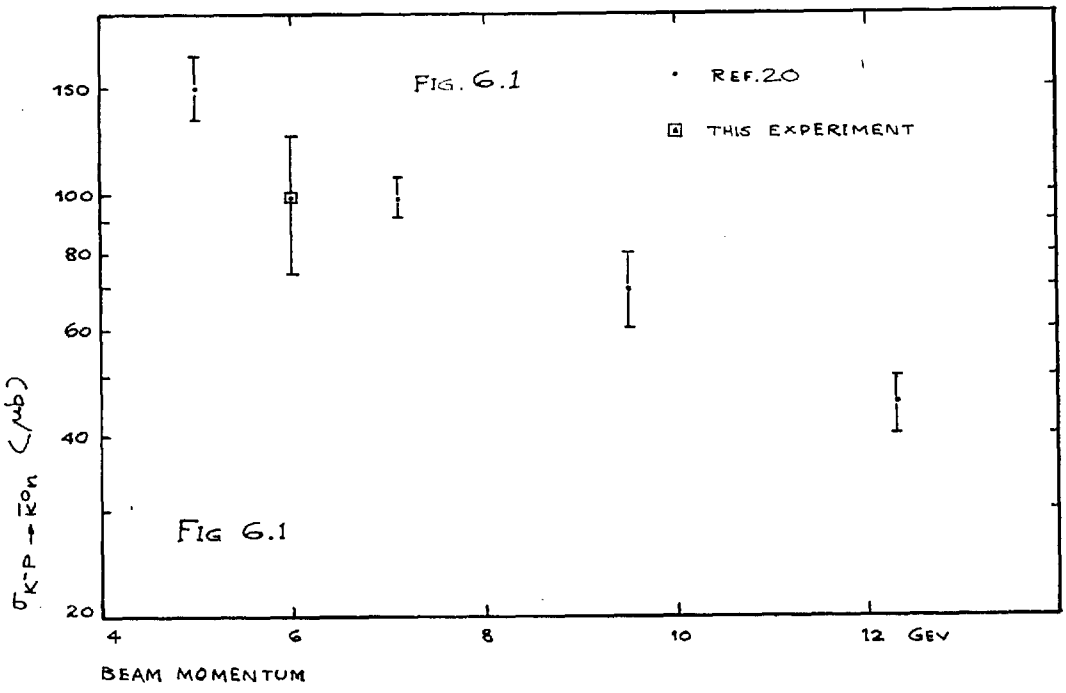
FIG. 6.1
REF.20
THIS EXPERIMENT
150
100
80
60
40
20
4
6
8
10
12 GEV
BEAM MOMENTUM
$\sigma_{K^-P \to \bar{K}^0 n}$ (mb)

FIG 6.1

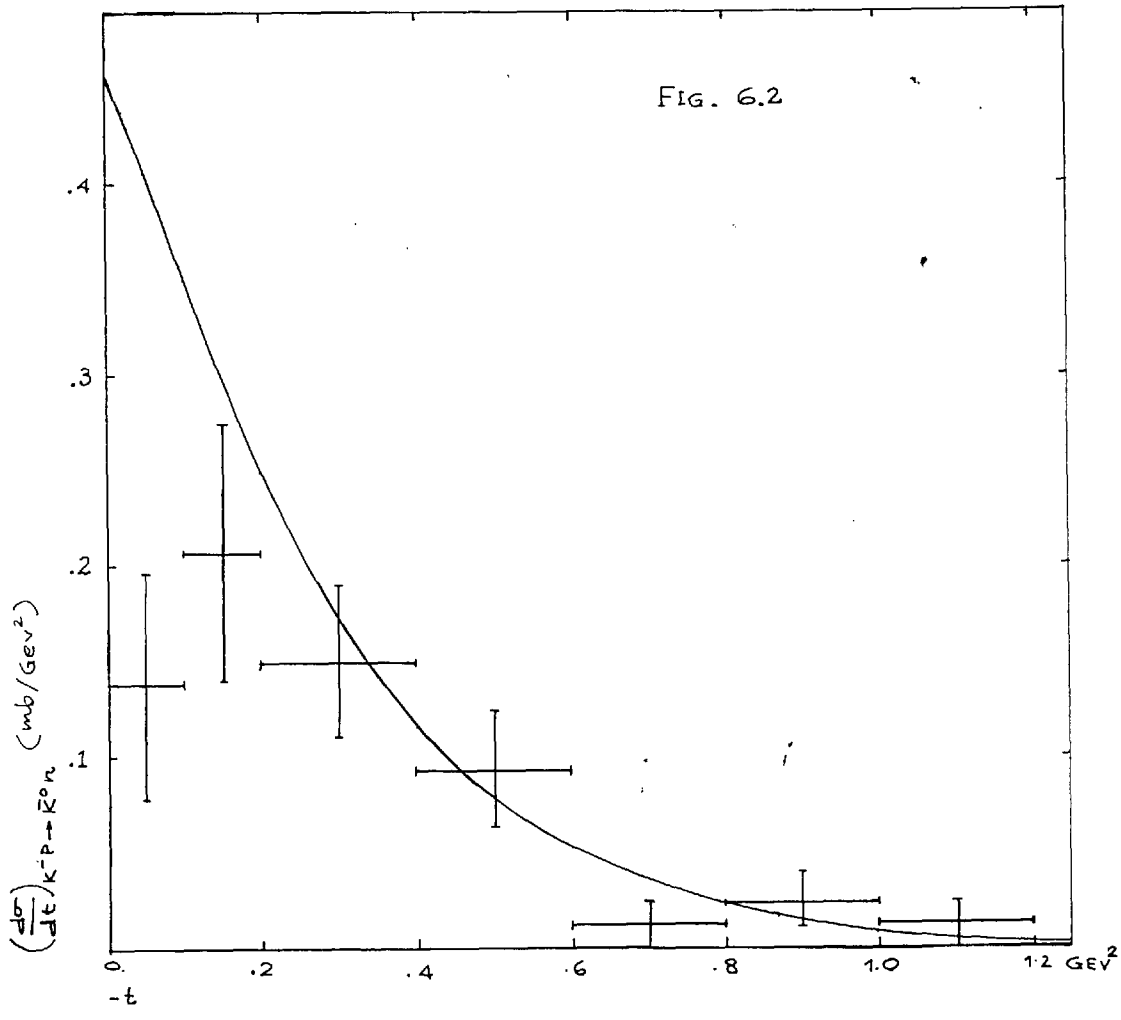
FIG. 6.2
.4
.3
.2
.1
0.
.2
.4
.6
.8
1.0
1.2 GEV^2
-t
$\left(\frac{d\sigma}{dt}\right)_{K^-P \to \bar{K}^0 n}$ (mb/GeV^2)

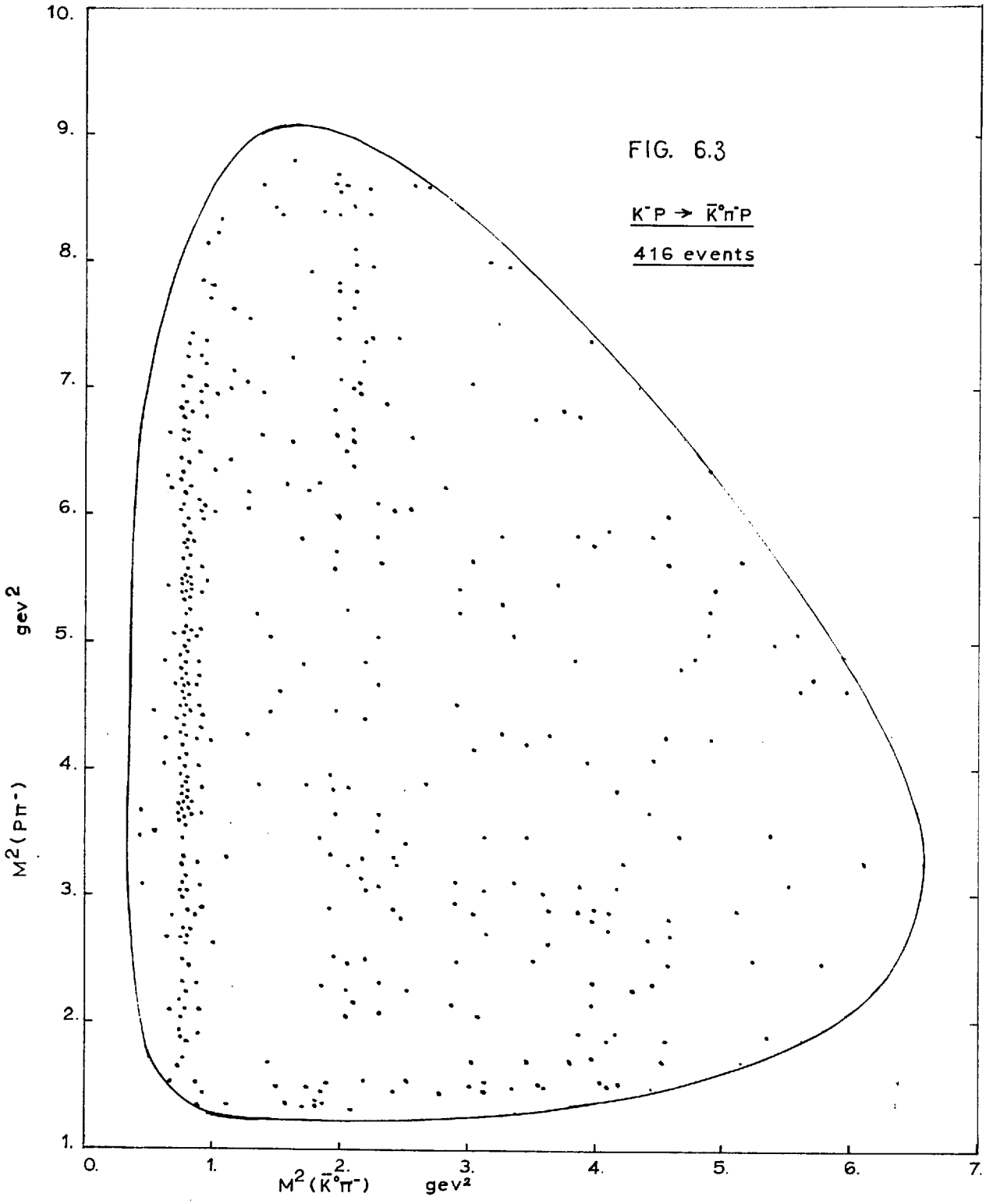
FIG. 6.3
K⁻P → K̄°π⁻P
416 events
M²(Pπ⁻) gev²
M²(K̄°π⁻) gev²
10.
9.
8.
7.
6.
5.
4.
3.
2.
1.
0.
1.
2.
3.
4.
5.
6.
7.

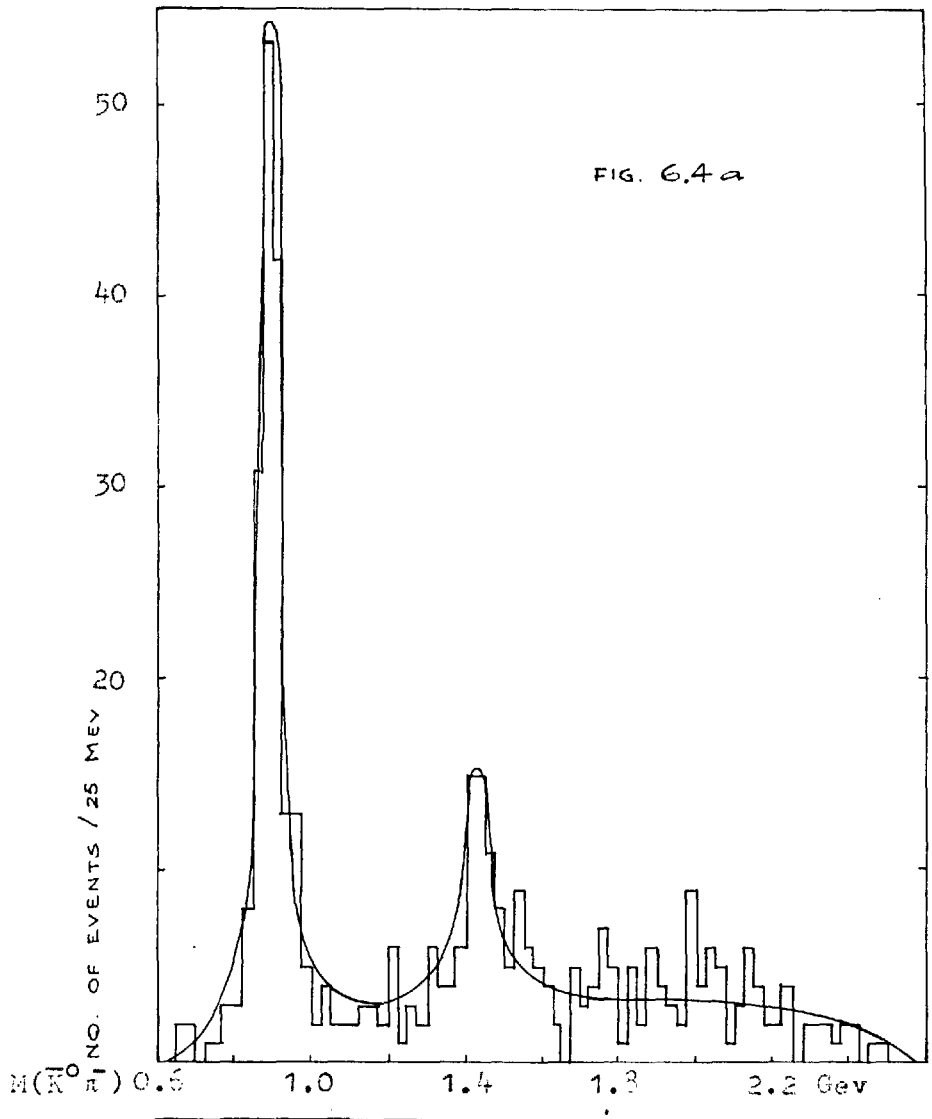
$K^-P \to \bar{K}^0\pi^-P$
FIG. 6.4a
NO. OF EVENTS / 25 MEV
50
40
30
20
$M(\bar{K}^0\pi^-)$ 0.6
1.0
1.4
1.8
2.2 Gev

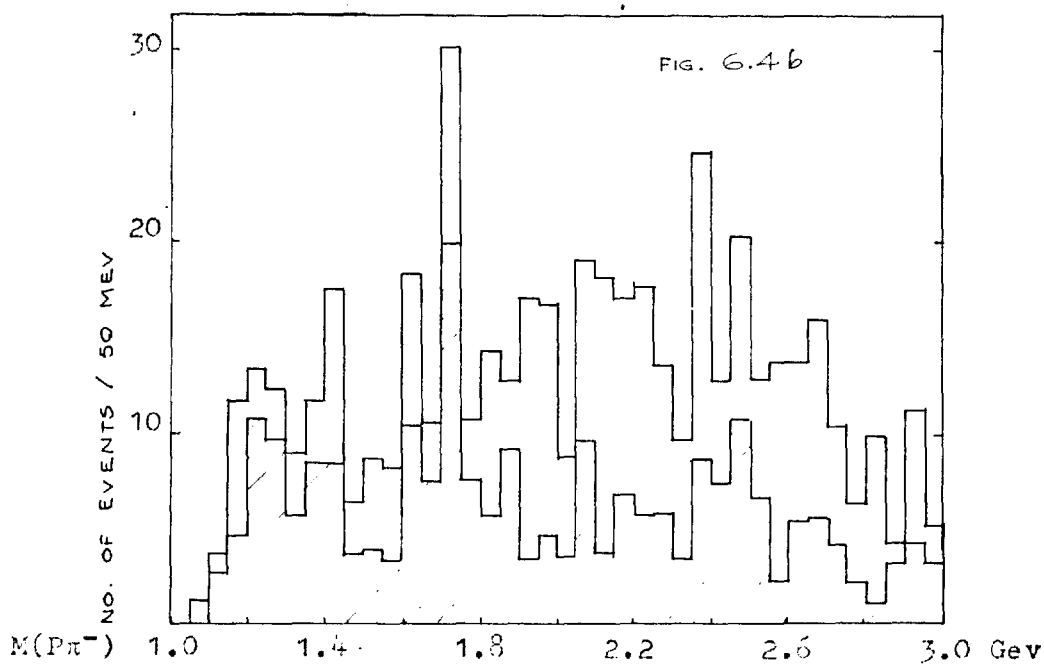
FIG. 6.4b
NO. OF EVENTS / 50 MEV
30
20
10
$M(P\pi^-)$ 1.0
1.4
1.8
2.2
2.6
3.0 Gev

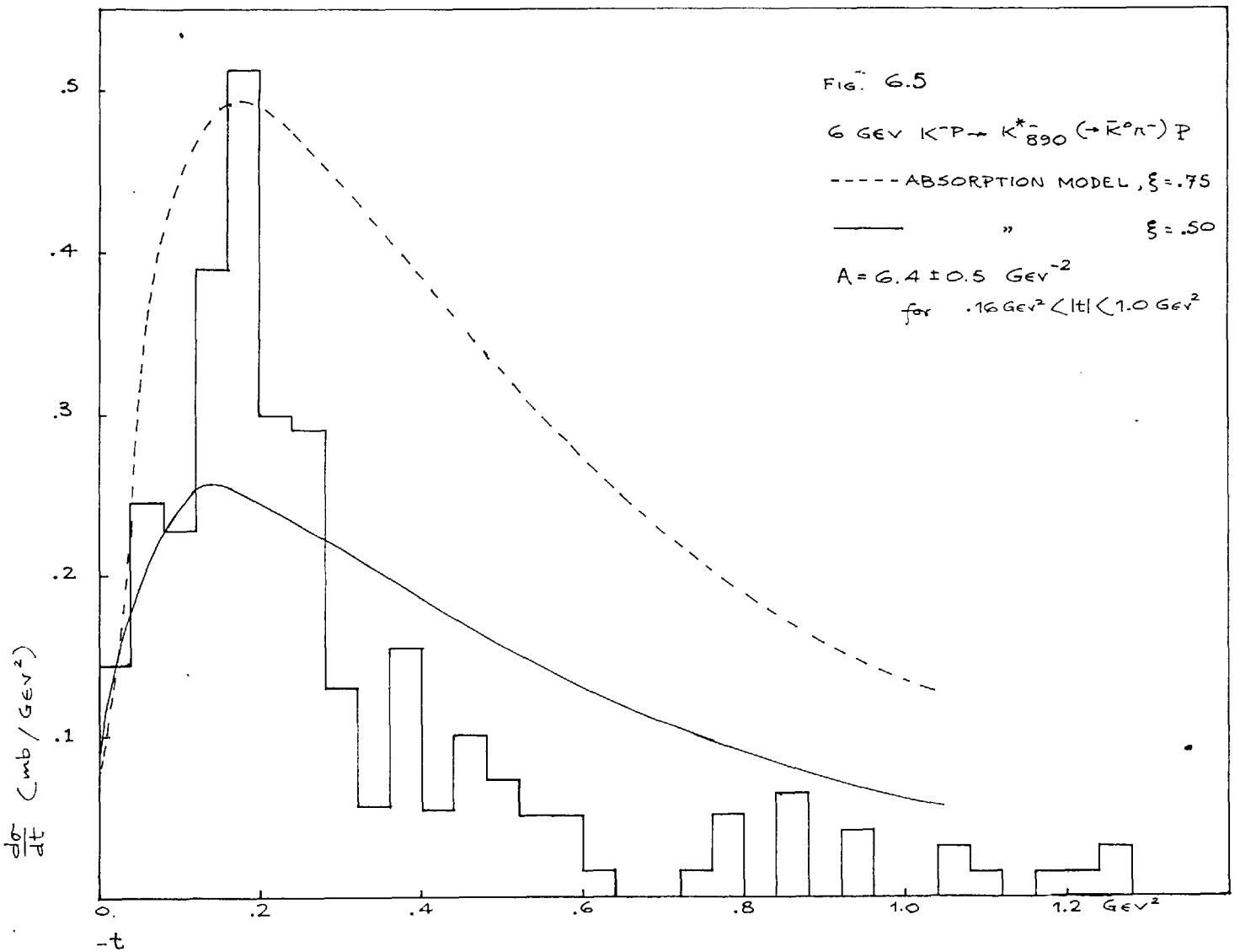
FIG. 6.5
6 GEV $K^-P \to K^{*-}_{890}(\to \bar{K}^0\pi^-)P$
----- ABSORPTION MODEL, $\xi = .75$
——— " $\xi = .50$
$A = 6.4 \pm 0.5$ GEV^{-2}
for .16 GEV^2 < |t| < 1.0 GEV^2
$\frac{d\sigma}{dt}$ (mb / GEV^2)
.5
.4
.3
.2
.1
0.
.2
.4
.6
.8
1.0
1.2 GEV^2
-t

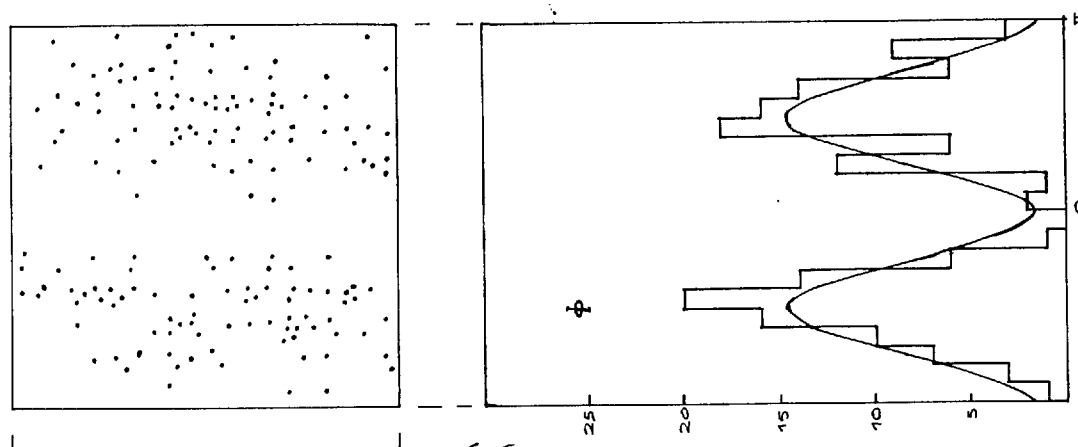
π
0
-π
φ
25
20
15
10
5

FIG. 6.6

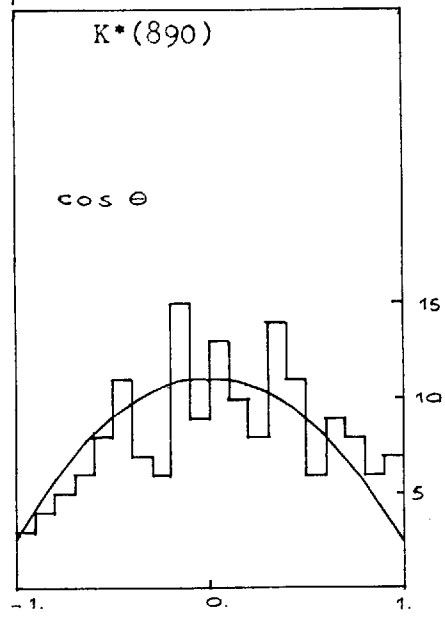
K*(890)
cos θ
15
10
5
-1.
0.
1.

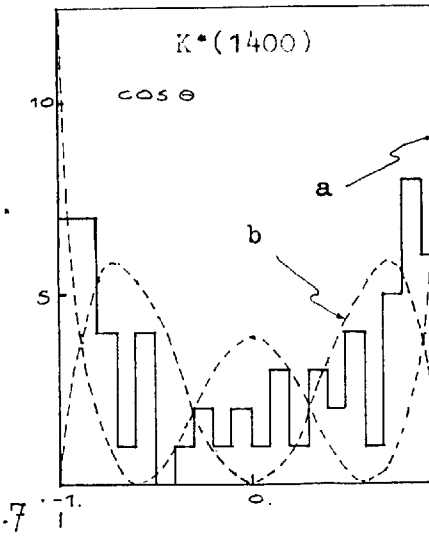
K*(1400)
cos θ
10
5
a
b
-1.
0.
1.

FIG. 6.7

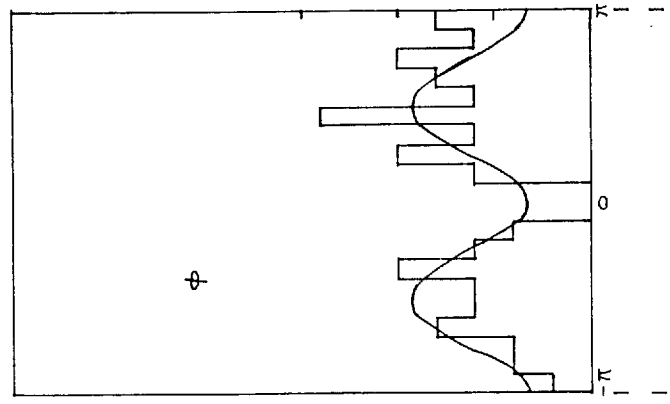
π
0
-π
φ

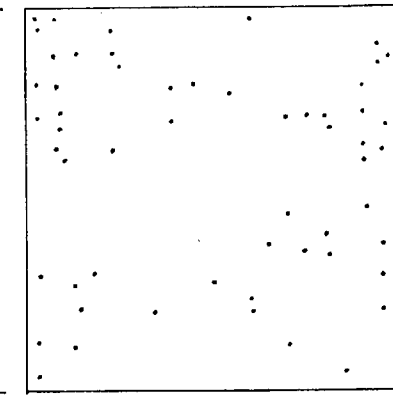

FIG. 6.8

– – – – – absorption model ξ = .75

——— " ξ = .50

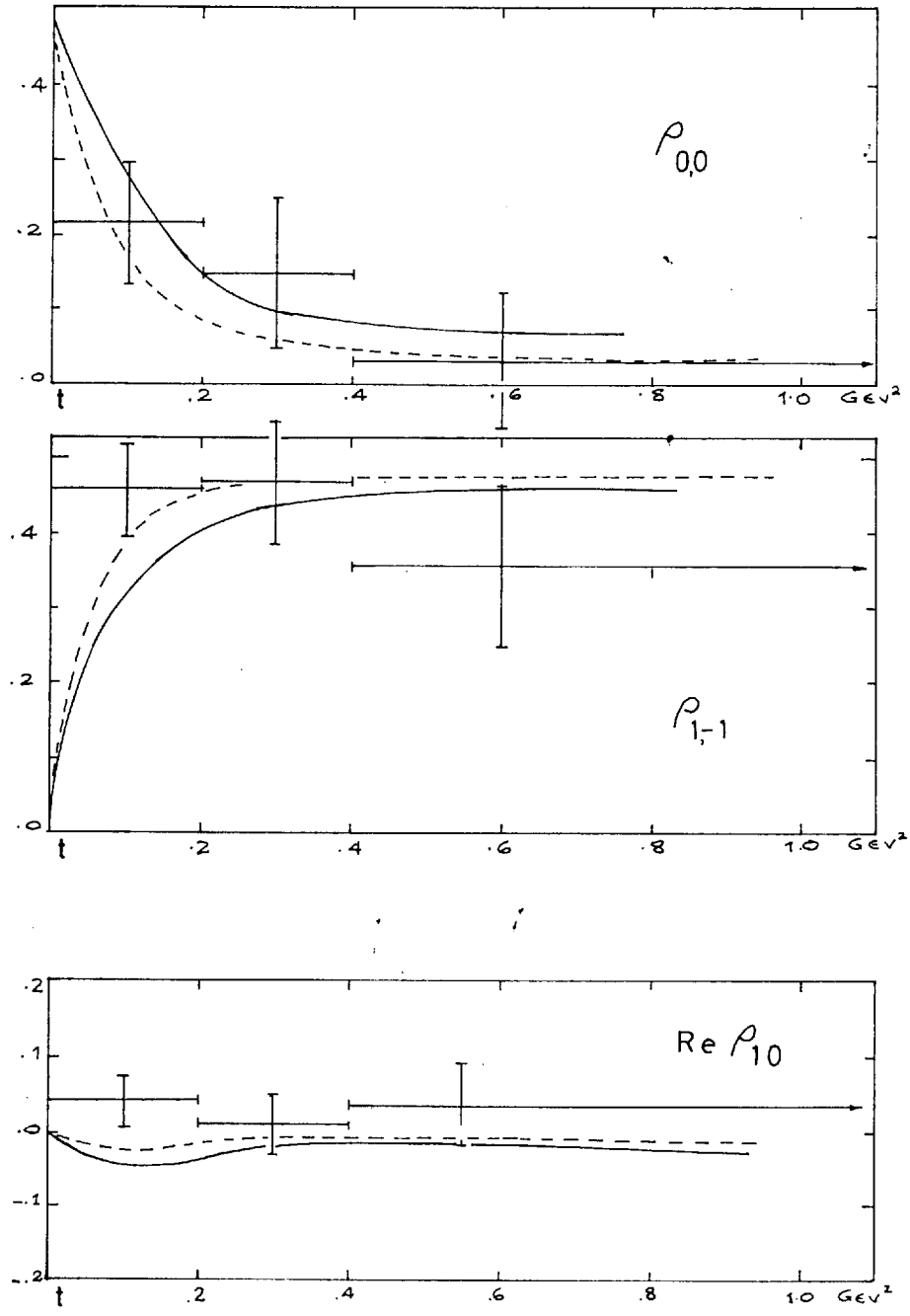

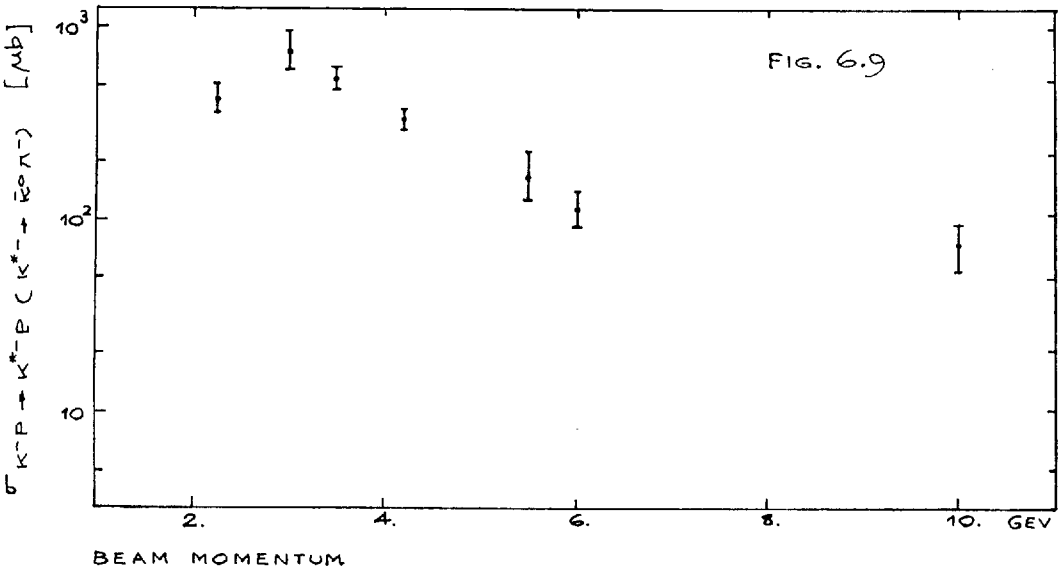

FIG. 6.9

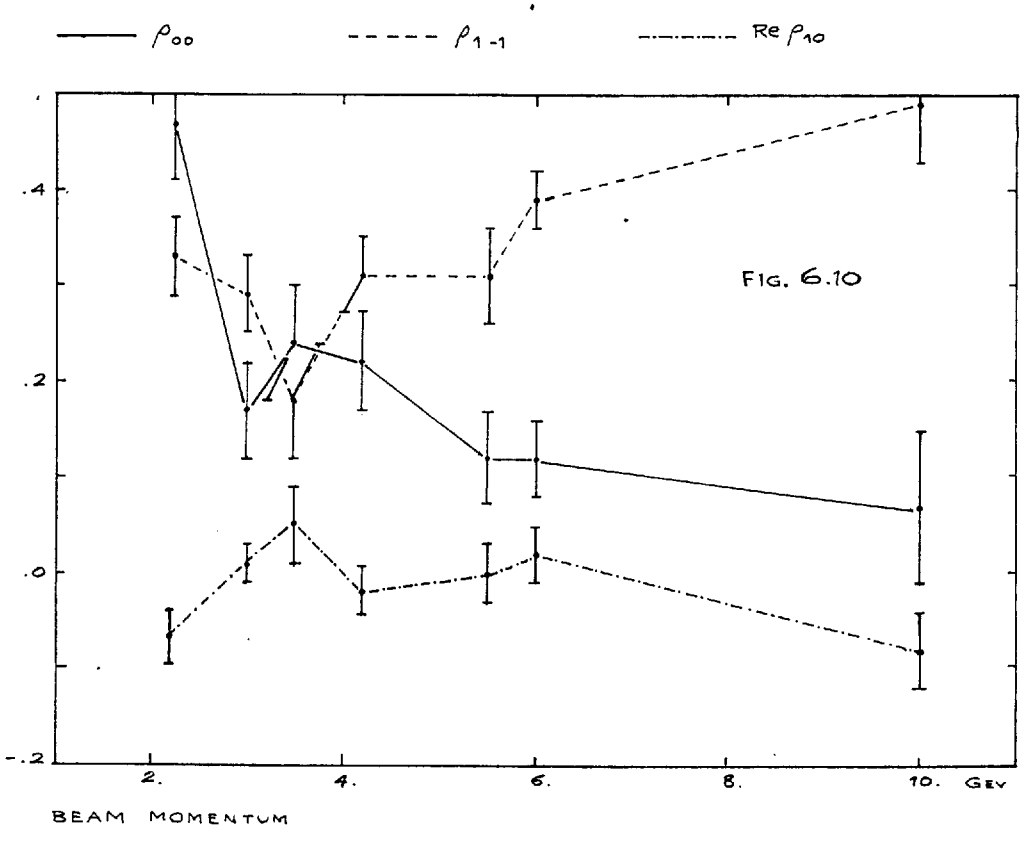

FIG. 6.10

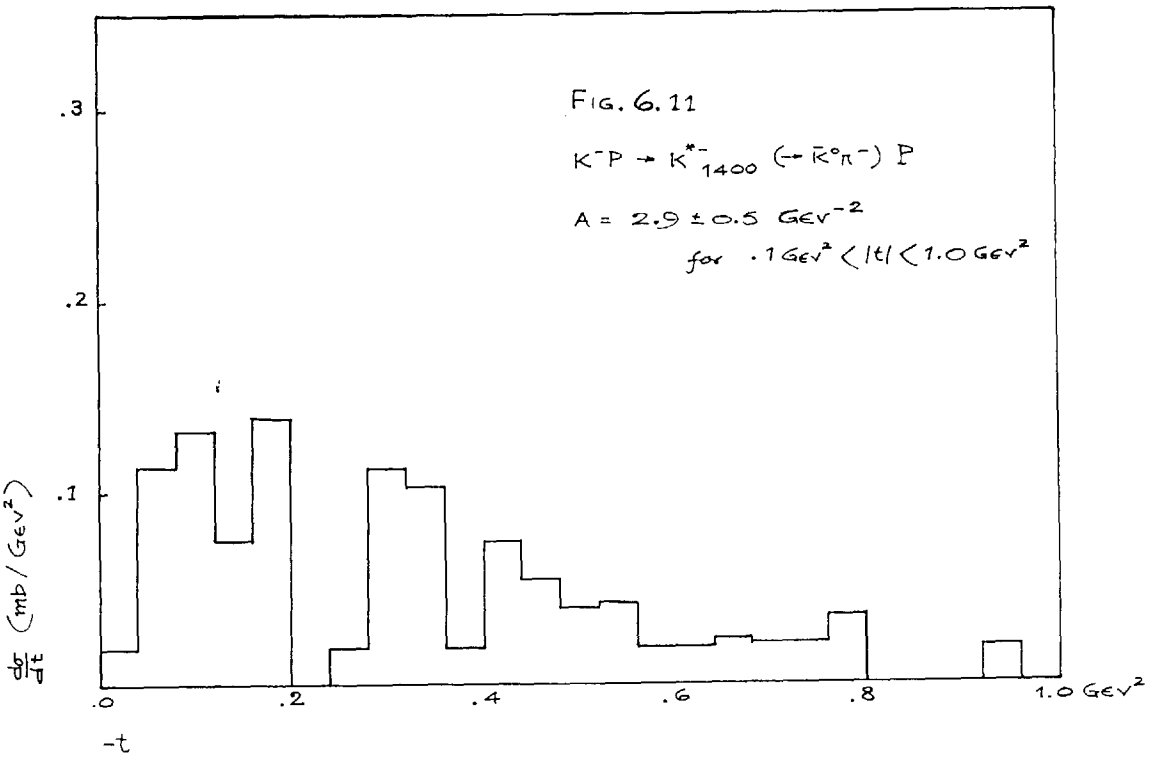

FIG. 6.11

$K^- P \to K^{*-}_{1400} (\to \bar{K}^0 \pi^-) P$

$A = 2.9 \pm 0.5$ GeV^{-2}

for $.1\ \text{GeV}^2 < |t| < 1.0\ \text{GeV}^2$

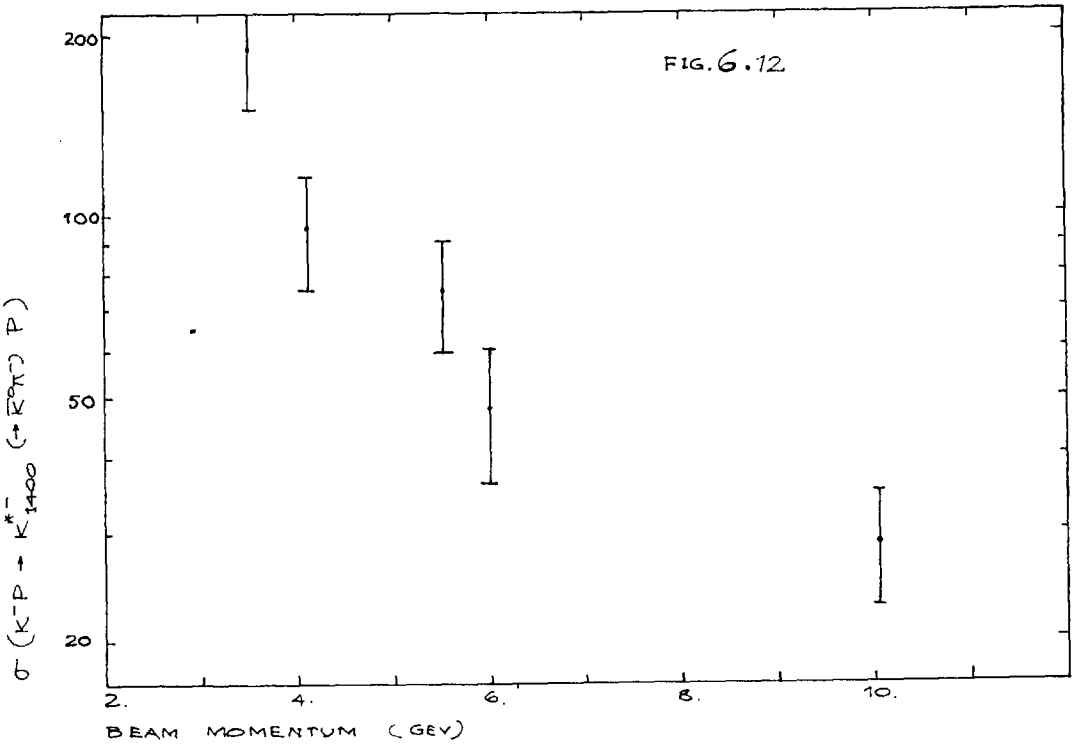

FIG. 6.12

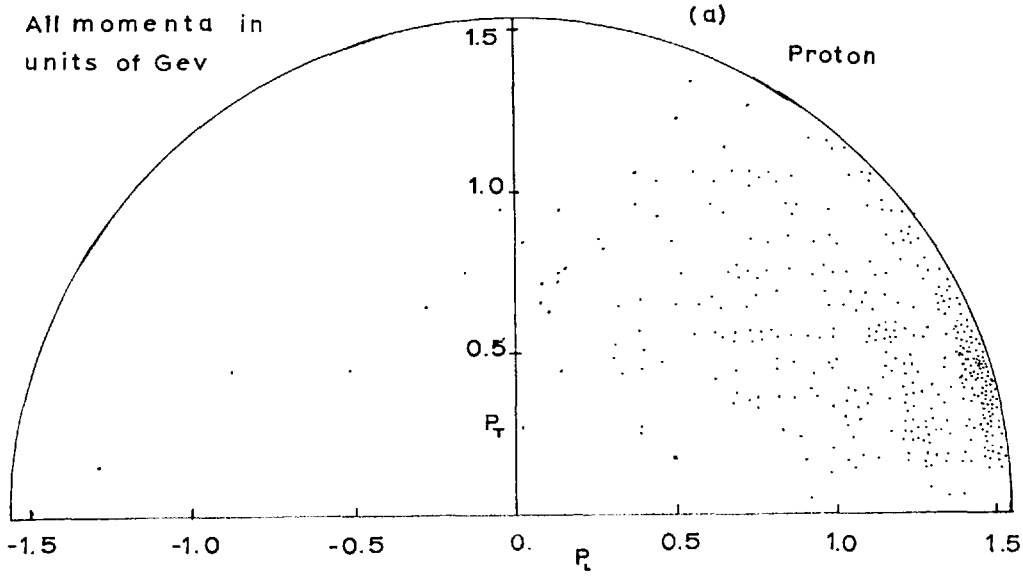

FIG. 6.13

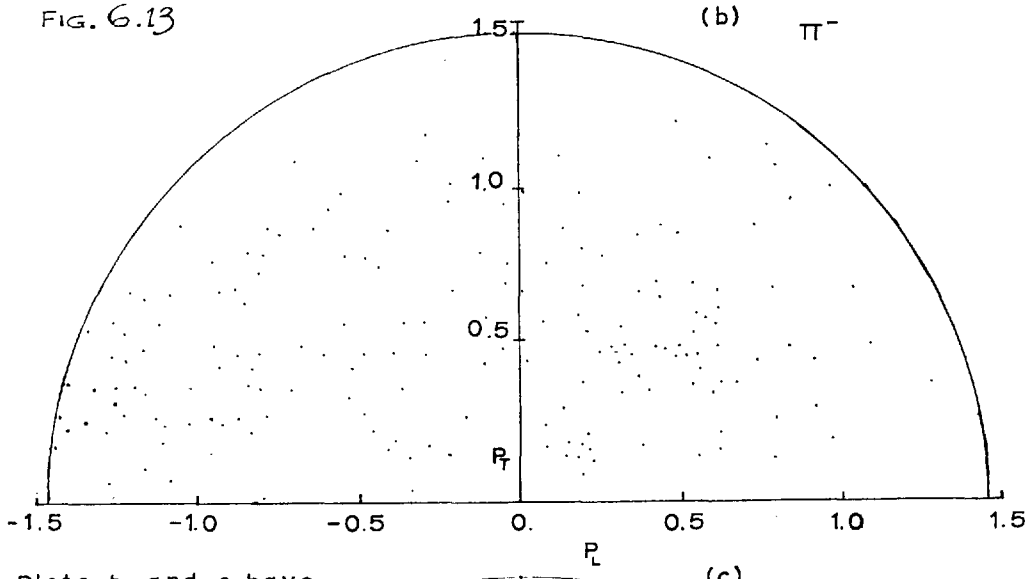

Plots b and c have K^*'s (890 and 1400) removed

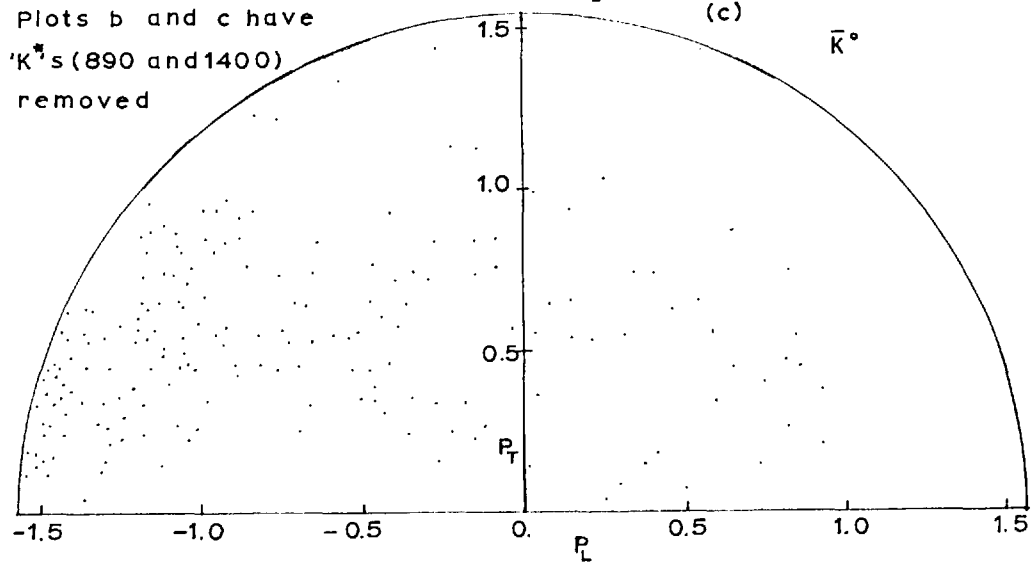

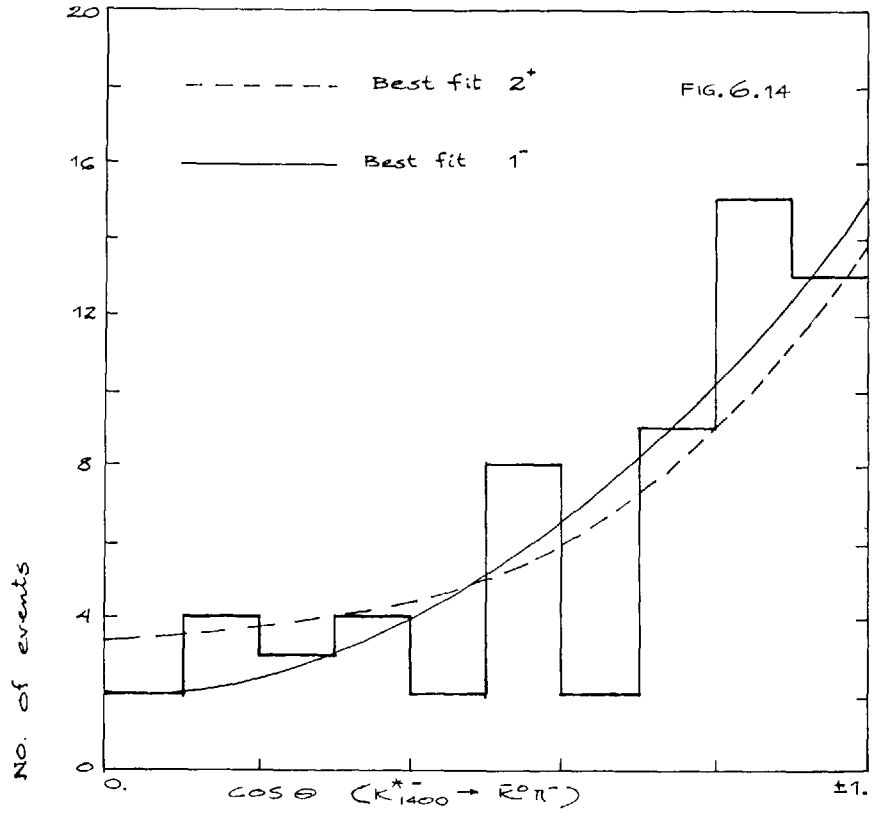

FIG. 6.14

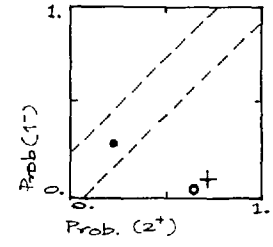

\+ 6 GeV π^-p , B.N.L.

o 3 GeV K^-p , E.P. + S. + Z.L.

4.1, 5.5 GeV K^-p , A.N.L. + N.U.

• 6 GeV K^-p , B-G-L-M-O-R.

FIG. 6.15

Chapter 7 Four-body final states of the type $\bar{K}N\pi\pi$.

The following four-particle final states have been studied:

(1) $\bar{K}^{o}n\pi^{+}\pi^{-}$

(2) $\bar{K}^{o}P\pi^{-}\pi^{o}$

(3) $K^{-}P\pi^{+}\pi^{-}$.

The first two appear as 201 s while the third as four-prongs. Figs. 7.1-2-3 show some triangle plots for these final states and the contributions from various channels are listed in table 7.1. The K^{*}_{890} s are the most preminent resonances in these channels. The fitted parameters of the K* s (890 and 1400) observed in this experiment are shown in table 7.2.

The $(\bar{K}\pi)^{o,-}$ mass distributions are shown in figs. 7.23-26. Except in the case of $\bar{K}^{o}\pi^{o}$ for channel (2), the solid lines drawn on the histograms show the fitted distributions. In the case of $\bar{K}^{o}\pi^{-}$ in final states (1) and (2), the fitted distributions are the sum of K^{*-}_{890} and normal phase space. The K^{*}_{1400} has been included in the case of $K^{-}\pi^{+}$ in final state (3). In these cases the normal Lorentz-invariant phase space is a fair approximation since the K^{*}_{890} s are strong and the phase space distortions do not seriously affect the estimation of the percentages of K*. In the case of $\bar{K}^{o}\pi^{o}$ mass spectrum, the distortion produced by peripherality and other resonances or 'bump's is quite appreciable

and it is difficult to do a Breit-Wigner curve fitting. The cross-section for the channel $\bar{K}^{*o}\pi^{-}P$ can be obtained more accurately from the final state (3) and no attempt to do this fitting has been made in the case of (2). Instead, we subtract the expected no. of $\bar{K}^{*o}_{890}$ events from the $\bar{K}^{o}\pi^{o}$ mass plot (shaded area) and a comparison of the unshaded area with the normal phase space (solid line) gives an idea of the distortion produced. Clearly, there is an excess of events in the low mass end as expected as a result of $K\pi\pi$ bumps (treated later in this chapter). Similar distortions have been noticed in the π-π spectra as well and in channels (2) and (3), the uncertainty in the two π phase space adds to the error in the estimated amounts of the ρs present.

The central mass values of the K*s have been determined without putting in the effects of orbital angular momenta. If the K^*_{890} and the K^*_{1400} are supposed to have $J^P = 1^-$ and 2^+ respectively, they would appear to have the peak mass values lowered in the case of ($K\pi$) decays by 2.4 and 4.8 Mev respectively.

$K^{*-}N^{*+}$

It can be seen in table 7.1 that processes of the type $K^*\pi N$ and $K\pi N^*$ have fairly large cross-sections — of the order of hundred millibarns. We, therefore, look for any associated production of the K^{*-} and the N^{*+} in the triangle plot shown in

Table 7.1

Final state	channel	cross - section (mb)
$\bar{K}^{o}n\pi^{+}\pi^{-}$		.665 ± .070
	$K^{*-}n\pi^{+}$	.225 ± .023
	$\bar{K}^{*o}_{1400}n$	.066 ± .025
	$\bar{K}^{o}n\rho^{o}$	.040 ± .025
	$N^{*+}\bar{K}^{o}\pi^{-}$	.062 ± .015
	$K^{*-}N^{*+}$	see text
$\bar{K}^{o}P\pi^{-}\pi^{o}$		.878 ± .100
	$K^{*-}P\pi^{o}$	.404 ± .060
	$\bar{K}^{o}P\rho^{-}$	.153 ± .050
	$N^{*+}\bar{K}^{o}\pi^{-}$	.120 ± .032
	$\bar{K}^{*o}P\pi^{-}$	Not attempted but known from the final state $K^{-}P\pi^{+}\pi^{-}$.
	$\bar{K}^{*o}_{1400}P\pi^{-}$	
	$K^{*-}N^{*+}$	see text
$K^{-}P\pi^{+}\pi^{-}$		.594 ± .110
	$\bar{K}^{*o}P\pi^{-}$	.255 ± .060
	$\bar{K}^{*o}_{1400}P\pi^{-}$	.040 ± .009
	$K^{-}P\rho^{o}$	.074 ± .040
	$N^{*++}K^{-}\pi^{-}$	.172 ± .045
	$N^{*o}K^{-}\pi^{+}$	.026 ± .010
	$N^{*+}_{1518}\ K^{-}$	.041 ± .016
	$N^{*+}_{1688}\ K^{-}$	.065 ± .023

Table 7.2

Resonance	Channel	Mass (Mev)	Width (Mev)
K^{*-}_{890}	$(\bar{K}^{o}\pi^{-})$ P	891.8 ± 3.0	47.3 ± 4.5
K^{*-}_{890}	$(\bar{K}^{o}\pi^{-})\pi^{+}n$	896.7 ± 3.5	47.3 ± 3.5
K^{*-}_{890}	$(\bar{K}^{o}\pi^{-})\pi^{o}P$	887.2 ± 2.0	59.0 ± 4.2
$\bar{K}^{*o}_{890}$	$(K^{-}\pi^{+})\pi^{-}P$	891.6 ± 2.7	55.5 ± 8.0
K^{*-}_{1400}	$(\bar{K}^{o}\pi^{-})P$	1436 ± 9	85 ± 15
$\bar{K}^{*o}_{1400}$	$(K^{-}\pi^{+})\pi^{-}P$	1420 ± 10	75 ± 18
$\bar{K}^{*o}_{1400}$	$(\bar{K}^{o}\pi^{-}\pi^{+})n$ **	1414 ± 13	81 ± 14

** $K^{*-}\pi^{+}$ events only.

fig. 7.4. The events included in this plot are only those with the $|t|$ to the $\bar{K}^{o}\pi^{-}$ or the $N\pi^{+}$ system less than 0.5 Gev^{2}. Since the process $K^{-}P \rightarrow K^{*-}N^{*+}$ is expected to be more peripheral than the events with only one or no resonance in, this sample should be more enriched in genuine $K^{*-}N^{*+}$ events.

In the overlap region of the K* and the N* bands we find an excess of $\sim$ 30 events over the number expected from an incoherent addition of non-resonant background and events of the type $K^{*-}(P,n)$ (π^{o},π^{+}) and $\bar{K}^{o}\pi^{-}N^{*+}$. By a similar exercise with the same triangle plot for channels (1) and (2) combined including all events, we find an excess of 31 ± 14 events

which is equivalent to a cross-section of .026 ± .014 mb. for the process

$$K^-P \rightarrow K^{*-} (\rightarrow \bar{K}^0\pi^- \text{ only}) \; N^{*+} (\rightarrow P\pi^0 \text{ and } n\pi^+) .$$

This cross-section is probably an underestimate since some of the $K^{*-}N^{*+}$ events are expected outside the chosen overlap region. These events sit on a background of $\sim$ .07 mb. and it is not possible to do any further analysis of the process.

$K^-\pi^-N^{*++}$

The $P\pi^+$ mass distribution, shown in fig. 7.5 shows a prominent N^{*++}_{1238} resonance and a large part of the events in this channel without a $\bar{K}^{*0}$ are produced via the channel $K^-\pi^-N^{*++}$. No deviation from phase space is expected in the $K^-\pi^-$ mass spectrum. However, the $N^{*++}\pi^-$ as well as the $P\pi^+\pi^-$ combinations appear to deviate quite strongly from the phase space, as shown in fig. 7.6. Both these distributions show two peaks at approximately 1500 and 1700 Mev.

A similar effect has been noticed by Alexander et. al. in P-P collisions at 5.5 Gev[26]. In the present experiment, these peaks cannot be definitely established as resonances and two explanations can be put forward. They may arise from Deck-type scattering of the K^- and π^- as shown in fig. 7.27a, which is expected to produce a low-mass enhancement in the $N^{*++}\pi^-$

mass distribution. Alternatively, and more probably, they may be due to the N* resonances at 1518 and 1688 Mev. The observed widths of these peaks are consistent with the expected 125 Mev for the N^*_{1518} but the 1688 peak appears to be rather broad for the expected value of $\sim$ 100 Mev. The reason may well be a background which is greater at the position of the second peak due to rising phase space.

Both these N^{*+}s are expected to decay into $N^{*o}_{33}\pi^+$ as well, the branching ratios depending on the isotopic spins. The ratio for decay into $N^{*++}_{1238}\pi^-$ and $N^{*o}_{1238}\pi^+$ (with $N^{*o} \rightarrow P\pi^-$) is

1 : 1/9 for I of N*(1518 or 1688) = 1/2

1 : 4/9 " " = 3/2.

It is estimated that there are 89±10 events in the N* peaks and the fact that there are altogether 22±5 events in the N^{*o}_{33} peak in the $P\pi^-$ mass distribution is consistent with the $I = \frac{1}{2}$ assignment to these N*s.

$\overline{K}^{*o}_{1400}$

The $\overline{K}^o\pi^+\pi^-$ mass spectrum in channel (2) is shown in fig. 7.7. for all events in the sample and for those with the $\overline{K}^o\pi^-$ mass within the K* range (i.e. .830 < M(Kπ) < .950 Gev). The K^*_{1400} enhancement appears quite distinctly and is strongly associated with the K^{*-}_{890} resonance.

Fig. 7.9 shows a Dalitz plot of the events with the $\bar{K}^{o}\pi^{+}\pi^{-}$ mass between 1.375 Gev and 1.575 Gev. A concentration of events along the K^{*-}_{890} band, specially in the overlap region of the K^{*-}_{890} and the ρ^{o} bands is noticeable and suggests $K^{*-}\pi^{+}$ and $\bar{K}^{o}\rho^{o}$ as possible decay modes of the resonance. The $\bar{K}^{o}\pi^{-}$ and $\pi^{+}\pi^{-}$ masses for these events and for those in the background region are plotted in fig. 7.10. The decay branching ratios can be determined by subtracting background plots from the K^{*}_{1400} plots and estimating the proportions of K^{*-}_{890} and ρ^{o} in the $\bar{K}^{o}\pi^{-}$ and $\pi^{+}\pi^{-}$ mass spectra thus obtained. The figures we get are:

$$\frac{K^{*-}\pi^{+}}{\text{total 3-body}} = .6 \pm .2 \; ; \quad \frac{\bar{K}^{o}\rho^{o}}{\text{total 3-body}} = .2 \pm .2$$

$$\frac{\bar{K}^{o}\pi^{-}\pi^{+}}{\text{total 3-body}} = .2 \pm .2$$

However, large background prevents any further analysis. Fig.7.8 shows the $\cos\theta$ distribution for events in the peak and background regions for K^{*}_{1400} decay into $K^{*-}_{890}\pi^{+}$. Both of them show a strong asymmetry, the K* tending to go forwards with respect to the beam in the $K^{*-}\pi^{+}$ rest frame. This arises from the multiperipheral behaviour of the 3-body state $K^{*-}n\pi^{+}$ and would be discussed later.

A qualitative feature of these events can be studied as follows. It can be expected that in the K^{*o}_{1400} region, The $K\pi\pi$

system would be more peripheral than in the background. The values of the slope parameter A for these events are:

For K^*_{1400} region $3.87 \pm .38$

For background $3.80 \pm .49$.

The similarity of these values indicates that the background events are as peripheral as those in the K* region and it is not possible to separate the K^*_{1400} events by a t - cut.

The $K\pi\pi$ enhancements

It has been seen that the $\overline{K}^o\pi^+\pi^-$ mass spectrum in the channel (1) can be explained by Lorentz invariant phase space plus some amount of K^*_{1400}. The $(K\pi\pi)^-$ mass spectra for the channels (2) and (3) are shown in figs. 7.11 and 7.12. Clearly they show an entirely different shape with a large clustering of events in the mass range of 1100 - 1500 Mev.

The nature of the events in these $K\pi\pi$ bumps can be examined with the help of figs. 7.13 and 7.14. The boundaries on the Dalitz plots correspond to central values of the range chosen for $K\pi\pi$ mass. The mass distributions are shown in the accompanying histograms. In the $\overline{K}^o\pi^-\pi^oP$ events there is a strong K^{*-}, a less strong $\overline{K}^{*o}$ and a doubtful ρ^-. For the $K^-\pi^+\pi^-P$ events, $\overline{K}^{*o}$ and ρ^o are clearly seen. There are several possible explanations

for a bump and the arguments for and against them will be discussed. The possibilities are

(a) constructive interference of resonances and triangular singularities.

(b) a kinematic effect

(c) one or more resonances.

(a) It can be shown that simultaneous production of two-body resonances can distort normal phase space. In the case of final state (2), any constructive interference between the channels $K^{*-}\pi^{o}P$ and $\bar{K}^{*o}\pi^{-}P$ can produce a heaping at low $K\pi\pi$ masses. However, if the mass of the $\bar{K}^{o}\pi^{-}$ system is plotted against those of the $\bar{K}^{o}\pi^{o}$, no excess of events is noticed in the overlap region of the K^{*} bands. In the case of the $K^{-}\pi^{+}\pi^{-}$ system in final state (3), this explanation is even more inadequate since the ρ^{o} in the $\pi^{+}\pi^{-}$ mass spectrum for the total sample is fairly weak.

The case of triangular singularities has been considered by Month[27]. In fig. 7.27b S,M,m_1 etc. denote masses and the process is collinear in space. S can be taken as an excited state which decomposes into M and m_3. M decays and one of the decay products, m_2, scatters off m_3. There is a singularity for the value of S for which this process is possible with the particles real and on the mass shells. It has been shown in ref.(27) that if the particles are taken as M=K^{*}, m_2,m_3 = π and m_1 = K, the

$K\pi\pi$ mass has a maximum at 1170 Mev. The mass value at which we observe the $K\pi\pi$ peak is certainly different and this explanation can be discarded.

(b) In trying to explain the $\rho\pi$ enhancement called the A_1, Deck [28] proposed a process of the type shown in fig.7.27d. If the particles C,D,E and e_1 in fig. 5.2 are replaced by K*, π, P and π respectively and if the particle e_1 is considered as scattered off the proton elastically, the K* and π in the final state would show an enhancement in the low mass region.[29] Such a process should have certain experimental consequences which will be examined below.

1. The scattering of the pion and the proton should show the characteristics of elastic scattering. There should be a strong forward peaking and an axial symmetry in the angular distribution of the scattered particles. In figs. 7.15 a and c the centre-of-mass scattering angle of the π - P has been plotted against the π-P mass for the events of the type $K^{*-}\pi^{o}P$ and $\bar{K}^{*o}\pi^{-}P$ from the final states (2) and (3) respectively. Figs. 7.15 b and d show the distributions of the azimuthal angles for the same events and these plots have been folded and combined in fig. 7.15e . The polar angle distribution shows the expected behaviour for elastic scattering and for high enough energy of the π-P system, there is a strong diffraction peak. However, the azimuthal angle (φ) distribution shows a

a definite asymmetry. The peaking at $\varphi = \pm \pi$ means that the pion tends to follow the K* more than expected in a 'Deck - mechanism' process.

2. It is implied that the K* in these cases are produced via a pion exchange. The distributions of the decay angles θ and φ should show the characteristics of pseudoscalar exchange, i.e. they should be of the form:

$$W(\cos\theta) \propto \sin^2\theta$$

$$W(\varphi) = \text{constant.}$$

The distributions of the $\cos\theta$ for events in the 'bump'-region (1.200 - 1.475 Gev) are shown in fig. 7.18 . Although the $\cos\theta$ distributions contain a fair amount of background, they appear to agree with a considerable proportion of pion-exchange. The φ distributions were less reliable but consistent with flatness.

3. The $K^{*-}\pi^{o}$ mass distribution for the channel $K^{*-}\pi^{o}P$ has been calculated by Fraser and Roberts[30] considering the diagrams shown in fig. 7.27d-e-f. The solid line drawn on fig. 7.11 is the distribution expected from maximum constructive interference of the amplitudes for these three processes. Altering the relative phases does not appreciably change the shape of the distribution but reduces the expected total cross-section. Quite clearly, the peaking in the $K^*\pi$ mass distribution cannot be explained with this hypothesis though it

predicts a large distortion in the $K^*\pi$ phase space. At the same time, it has been seen that the diagram in fig. 7.27f makes a large contribution and if that is true, it may seriously distort the pseudoscalar exchange behaviour of the K^* decay. The exact expected behaviour depends on the quantum numbers of the off-mass-shell K.

The total $K\pi\pi$ mass spectrum is even more unpredictable by theoretical calculations since there are contributions from other diagrams with the K^{*-} replaced by $\bar{K}^{*o}$ and ρ^- and the π^o, by π^- and $\bar{K}^o$. Similar arguments apply to the case of the $\bar{K}^{*o}\pi^-P$ channel in the final state (3).

4. The reaction $K^-P \rightarrow \bar{K}^{*-}\pi^+n$ should not show any bump in the $K^{*-}\pi^+$ mass. The reason is that the elastic scattering of the $\pi^o - P$ has to be replaced by charge-exchange scattering which is expected to have a much smaller cross-section. The $K^{*-}\pi^+$ mass spectrum in fig. 7.7 can be explained by phase space plus K^*_{1400} alone and certainly does not show a broad peaking. This feature definitely favours the Deck-mechanism.

We can probably conclude that diffraction-scattering processes are likely to be an important contributor to the $K\pi\pi$ bumps but can certainly rule them out as the only responsible mechanism.

(c) The resonance hypothesis gains a strong foothold once the others fail to explain the $K\pi\pi$ bump entirely. To date, the only established resonance that has been observed to decay into $K\pi\pi$, either directly or via $K^*\pi$ or $K\rho$ is the K^*_{1400}. The reaction $K^-P \rightarrow K^{*-}_{1400}P$ is clearly observed in the final state $\bar{K}^o\pi^-P$. Using the predicted decay branching ratio

$$\frac{K^*(1400) \rightarrow K^*(890)\ \pi}{K^*(1400) \rightarrow K\ \pi} = .6 \quad (31)$$

one can find the amounts of K^*_{1400} in the $K^{*-}\pi^o$ and the $\bar{K}^{*o}\pi^-$ decay channels in final states (2) and (3). The dashed lines in fig. 7.11-12 show the result of subtracting these events. The remaining events form a peak at about 1350 Mev with a width of about 200 Mev.

The behaviour of the $P\text{-}\pi^o$ system can be reviewed from the resonance hypothesis angle. We have taken the events fitting the $\bar{K}^o\pi^-P$ hypothesis as a test sample to look at the $\pi^-\text{-}P$ scattering if these events are considered as produced by a Deck mechanism. Fig. 7.27c illustrates the process. The $\cos\theta$ and φ for the $\pi^-\text{-}P$ scattering are plotted against the $\bar{K}^o\pi^-$ mass in fig. 7.16. Events in the K^{*-}_{890} and K^{*-}_{1400} bands are clearly seen to produce diffraction-like peaking in the $\cos\theta$ distribution. In the case of φ-distribution, they form clusters nearabout $\varphi = \pm\pi$. The behaviour is very similar to the $K\pi\pi$ bump events. The K*s are, however, well-identified as resonances apart from the fact that the diagram in fig.7.27c

includes a three-0^- (i.e. $\bar{K}^o$-K^--π^-) vertex and hence does not conserve parity and angular momentum. The $\cos\theta_{p-\pi}$ distribution of the $K\pi\pi$ bump events is, therefore, equally consistent with the resonance hypothesis whereas the $\varphi_{p\pi}$ distribution favours the latter.

The angular distributions of the K*(890 or 1400) P events can be easily explained. These two-particle states are produced with fairly large c.m.momenta. If the K* has a relatively small Q-value for decay into $K\pi$, both the decay products would be roughly collinear to the outgoing proton. However, due to peripheralism, the incoming and the outgoing protons have more or less the same direction of motion in the centre of mass. The Lorentz transformation to the π^--P_{out} rest frame is roughly parallel to the same direction again and therefore little alters the small angle between P_{in} and P_{out}.

The arguments for and against the resonance hypothesis are the following:

1) The isospin of this object, henceforth called the K^*_{1320}, can be 1/2, 3/2 etc. In any case, the neutral counterpart of this state should exist and show up in the reaction $K^-P \rightarrow \bar{K}^{*o}_{1320}n$. The $K\pi\pi$ bump appears to be strongly associated with the K^*_{890} and it is natural to assume $K^*_{890}\pi$ to be one of its principal decay modes. The $\bar{K}^{*o}_{1320}$ should then decay into $K^{*-}_{890}\pi^+$ and

should be seen in the shaded part of fig. 7.7 . We do not see any evidence of the $\bar{K}^{*o}_{1320}$.

To help the K^*_{1320} survive this severe test, a special model has been proposed. [32] The K^*_{1320} is assumed to be produced by a process similar to that shown in fig. 7.27d where the diffraction - scattered pion recombines with the K^*_{890} to form the K^*_{1320}. The absence of the $\bar{K}^{*o}_{1320}$ is explained by the fact that no charge can be exchanged in elastic scattering. However, a simpler explanation relies on the fact that K^{*-}_{1320} can be produced via the exchange of a T=0 object, the Pomeranchuk trajectory thus being a contributor. At high energies the contributions of all other particles fall off while that of the Pomeranchuk trajectory stays roughly constant. Thus the process $K^-P \rightarrow K^{*-}_{1320}P$ has an advantage over the process $K^-P \rightarrow \bar{K}^{*o}_{1320}\, n$ which demands a $T=1$ exchange.

2) A resonance is expected to have a constant mass value and a reasonable width. Although the constancy of the mass value of this resonance cannot be verified from the results of this experiment alone, a lack of such constancy has been reported. [33] The width of about 200 Mev is large compared to those of other known resonances but this is a less serious objection since effects like interference with $\bar{K}^*_{1400}$ can significantly alter the true width.

3) The decay of a resonance should have a symmetric $\cos\theta$ distribution. The K^*_{1320} can decay into $K^*\pi$ or $K\rho$ or directly into $K\pi\pi$. In the two-body decays θ is defined by the line of flight of any of the decay products. For the $K\pi\pi$ decay mode, the relevant direction is the normal to the decay plane. In the present experiment and, as a matter of fact, in all experiments done to date, it cannot be possible to separate out any single decay mode from the background. As seen in the case of $\bar{K}^{*o}_{1400}$ in final state (1), the background shows an asymmetric $\cos\theta$ distribution when treated as a state decaying into $K^*\pi$. It is, therefore, impossible either to verify the behaviour of the $\cos\theta$ distribution or to nullify it.

The preceding analysis does not lead to any one answer to the $K\pi\pi$ problem. To summarize the situation, (a) no kinematic enhancement explanation adequately describes the effect and (b) the resonance hypothesis suffers from the absence of the $\bar{K}^{*o}_{1320}$ in $K^-P \rightarrow \bar{K}^o n\pi^+\pi^-$. The case of the A_1 is more or less similar but the reaction $\pi^-P \rightarrow A_1^o n$ with the A_1^o decaying into $\rho^{\pm}\pi^{\mp}$ cannot be seen because of at least two neutral particles in the final state. With the information available at the moment the most likely explanation seems to be a superposition of

(1) A phase space that takes peripherality into account

the Deck-mechanism phase-space being one of them.

(2) K^*_{1400} plus other resonance(s). Various candidates have been reported in the past [33-4] but their appearence has been rather occasional. It is quite likely that their production processes have some kind of dependence on energy and experimental conditions. They may be produced in varying proportions in different experiments and possibly they interfere with each other to different extents. The shifting of the central mass value of the $K\pi\pi$ bump is easily understood with this picture.

The absence of K^*_{1320} (where we use this name for a conglomeration of various S=-1 mesonic resonances near this mass) can probably be explained byadiffraction-type picture. At high energies, the interaction $K^-P \rightarrow$ (B=0,S=-1 system) + P occurs mostly through a diffraction of the K off the proton. The final state would contain an excited K, the bracketed system being its manifestation. The K^*_{1320} resonance(s) are possibly produced mainly via this process and hence the preponderance of the K^*_{1320} with the same charge as that of the incident K^-. Ideas of this type have been used in the past for scattering of high energy particles on nuclei [35].

An experimental verification of such a process can be made by studying the t-distribution of the $K\pi\pi$ system. At lower energies any two-body state of the type K*P is produced strikingly more peripherally than the normal background. In

our case we expect a contrary behaviour i.e. we expect the whole $K\pi\pi$ spectrum to show the same trend - regardless of any resonances. The slope parameter A for different mass-slices of the $K\pi\pi$ system is shown in fig. 7.17. As expected, the parameter A changes quite smoothly across the $K\pi\pi$ spectrum and specially, there is no irregularity noticeable in the K^*_{1320} region. The falling-off of the parameter A with increasing mass of the $K\pi\pi$ system is a reflection of the fact that a large change in mass is likely to be accompanied by a large four-momentum transfer.

$\bar{K}^* \pi N$ systems

It has been seen that the cross-sections for the channels $K^{*-}\pi^+ n$, $K^{*-}\pi^0 P$ and $\bar{K}^{*0}\pi^- P$ in the four-body final states 1, 2 and 3 respectively are of the order of a few hundred μbs. To obtain samples of these events we select on the mass of the $\bar{K}\pi$ system alone, the mass range chosen being 830 - 950 Mev. N^{*+} events contaminate the first two channels ($\sim$10 %) but no attempt to remove the N^{*+} bands has been made since the non-resonant background exceeds the actual resonance present and its removal has an undesirable effect. With low $N\pi$ masses, they belong to a special class of events where the pion tends to follow the nucleon. The channel $\bar{K}^{*0}\pi^- P$ appears in the final state (2) as well but

this channel is dominated by the K^{*-} and it is difficult to isolate them without distorting some angular distributions. In final state (3) this channel is practically free from N^{*0}. The channel $K^{*-}\pi^{+}N$ has also a contamination of $\sim 15\,\%$ from $\bar{K}^{*0}_{1400}$ events.

Fig. 7.20 shows scatter plots of transverse momentum and longitudinal momentum of the particles. There seems to be convincing evidence that the K* and the nucleon more or less follow the directions of the K^{-} and the target proton respectively in the overall centre of mass. The pion, in all cases, seems to be more isotropic. The behaviour suggests a double - peripheralism as described in chapter 5. We replace the particles C, D and E in fig. 5.2 by K*, π and N. To demonstrate the effects of this mechanism we use the multiperipheral angles i.e. the scattering angles (θ) for K -> K* and P_{target} -> N in the K*π and Nπ c.m. respectively. It can be seen in fig.7.21 that the K*(N) is produced with a sharp forward peak with respect to the K(P_{target}) direction in the K*π(Nπ) rest frame. These distributions are very similar in natuee to those calculated by Joseph and Pilkuhn[43].

The decay of the K* gives some information about the particle e_1. The decay angular distributions of the K*s are shown in fig.7.19 with fitted curves. Table 7.3 shows the possible combinations of the particles e_1 and e_2 (we refer back to fig.5.2) and the spin density matrix elements of the K*s. Particles

heavier than the vector mesons have been ignored.

Table 7.3

Channel	e_1	e_2	ρ_{oo}	$\rho_{1,-1}$	$Re\,\rho_{10}$
(a)$K^{*-}n\pi^+$	ρ π,ω	π ρ	.24±.07	.21±.06	.01±.04
(b)$K^{*-}P\pi^o$	π^o ρ^o ω	ρ^o,el.* π^o,ω ρ^o	.58±.06	.08±.04	-.09±.04
(c)$\bar{K}^{*o}P\pi^-$	π ρ	ρ,el. π^o, ω	.56±.05	.01±.04	.00±.03

* el. indicates elastic scattering.

It should be remembered that the values of ρ_{oo} in channels b and c may imply more than 56 or 58% pseudoscalar exchange in the formation of the K*s since absorption is known to alter the value of ρ_{oo}.

The large proportions of pseudoscalar exchange in the case of channels b and c are consistent with a Deck-mechanism process. When ρ^o or ω take the place of e_1, one expects the final state to look like $K^* + P + (\rho^o \text{ or } \omega)$ since elastic scattering of the type $(\rho, \omega) + P \rightarrow (\rho,\omega) + P$ is expected to have a larger cross-section than reactions like $(\rho,\omega) + P \rightarrow \pi + P$. In channel a, however, the large $NN\pi$ coupling compared to $NN\rho$ [46] ($g^2/4\pi = 14.6$ and $\sim .5$ respectively) would favour e_2 to be a pion.

The particle e_1 is then a ρ and we expect the K^{*-} in channel a to show vector exchange characteristics — which indeed it does. The values of .21 for $\rho_{1,-1}$ and .24 for ρ_{00} imply a considerably larger amount of vector exchange than in the other cases even if absorption modifications come into play.

One can feel reasonably confident from the above features that the $\bar{K}^*\pi N$ channels are produced by double peripheral processes. A practical approach to this model has been made by Chan Hong-Mo et. al.[36]. They have considered the general case where all the three particles in the final state are permuted between the three vertices of a double-peripheral diagram. In the case of the $\bar{K}^*\pi N$ states, it is clear from the P_1-P_t plots that the diagrams considered before make by far the largest contributions and we can neglect the others. The amplitude in two-body processes is found to be proportional to e^{at}, a being a constant. Extending the same idea to double-peripheral processes one expects the amplitude to be proportional to

$$e^{a.t_{K\to K^*} + b.t_{P(tgt.)\to N}} .$$

It can be shown that this favours low $\bar{K}^*\pi$ and $N\pi$ mass combinations simultaneously i.e. produces a clustering of events in the high $\bar{K}^*N$ mass corner of the $\bar{K}^*\pi N$ Dalitz plot. The experimental Dalitz plots are shown in fig. 7.22 and the depopulation of the low $\bar{K}^*N$ mass region is quite striking.

Search for new resonances

To look for any $K\pi$ enhancements we combine the $\bar{K}\pi$ mass spectra from all the four-body final states studied (i.e. 1, 2 and 3) and the final state $\bar{K}^{o}\pi^{-}P$. The result is shown in fig. 7.28 and no significant enhancements are observed other than the K^{*}s (890 and 1400). The $\bar{K}^{o}\pi^{+}$ (in channel 1) and the $K^{-}\pi^{-}$ (in channel 3) mass distributions (not shown) do not show any such bumps either which could be attributed to isospin 3/2 $\bar{K}$ states.

The $\bar{K}\pi\pi$ mass spectra definitely do not show any sign of the L ($\sim$1800) resonance reported in ref. 37.

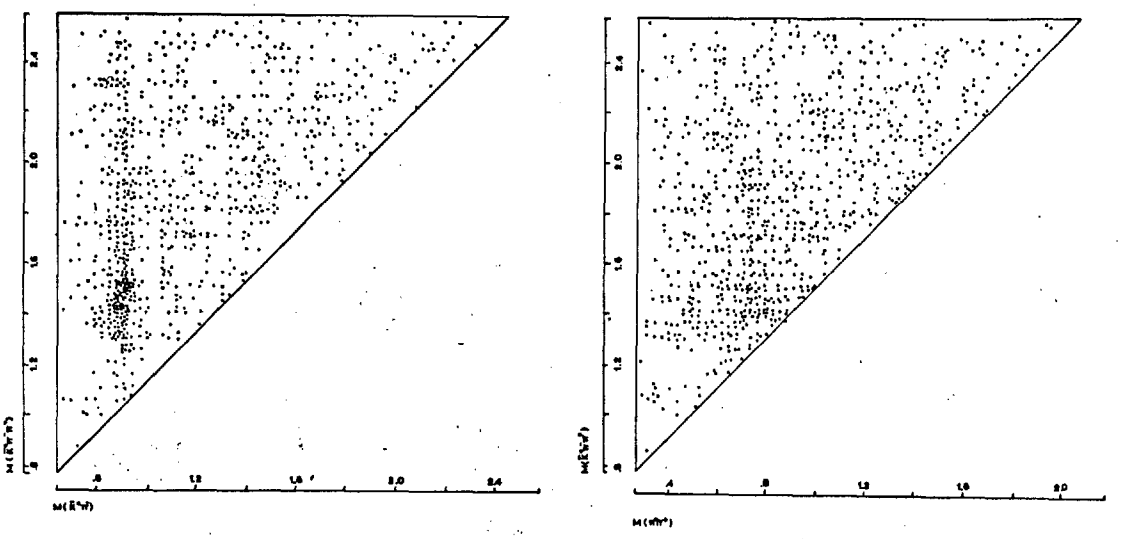

Fig. 7.1

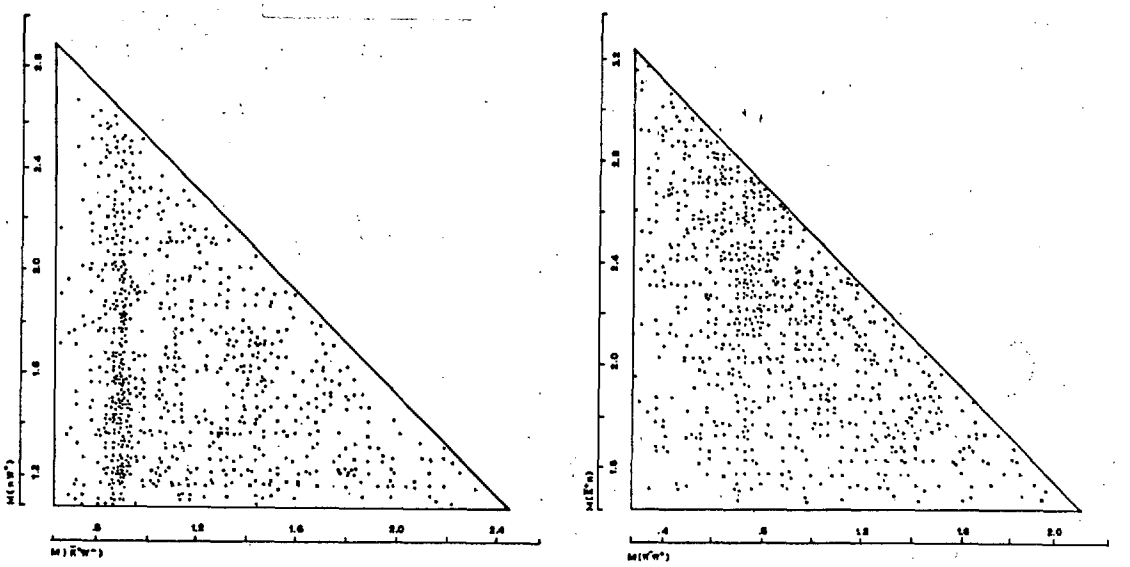

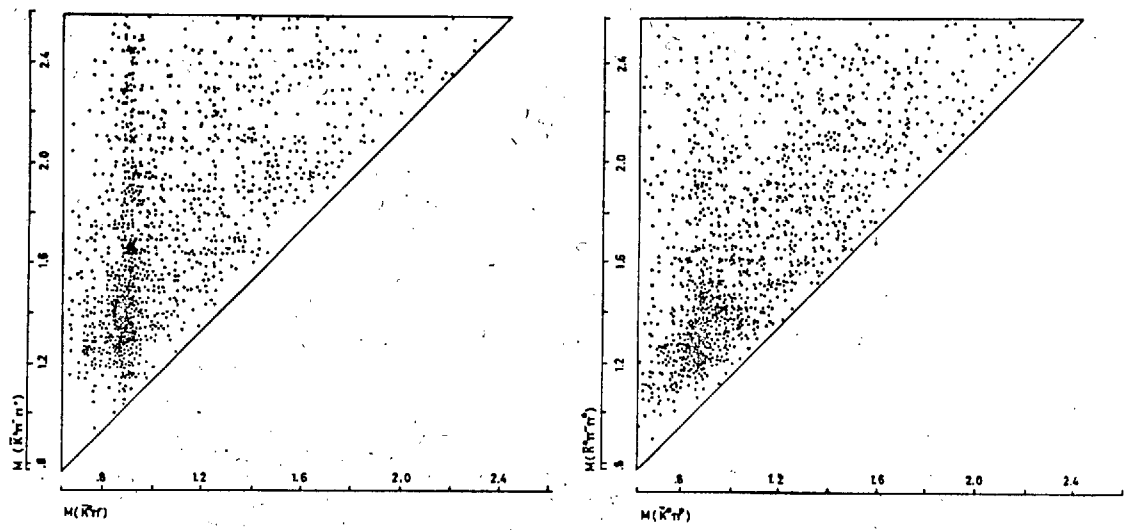

Fig. 7.2

$K^-P \rightarrow \bar{K}^{*0}P\pi^-\pi^{*0}$

(1166 EVENTS)

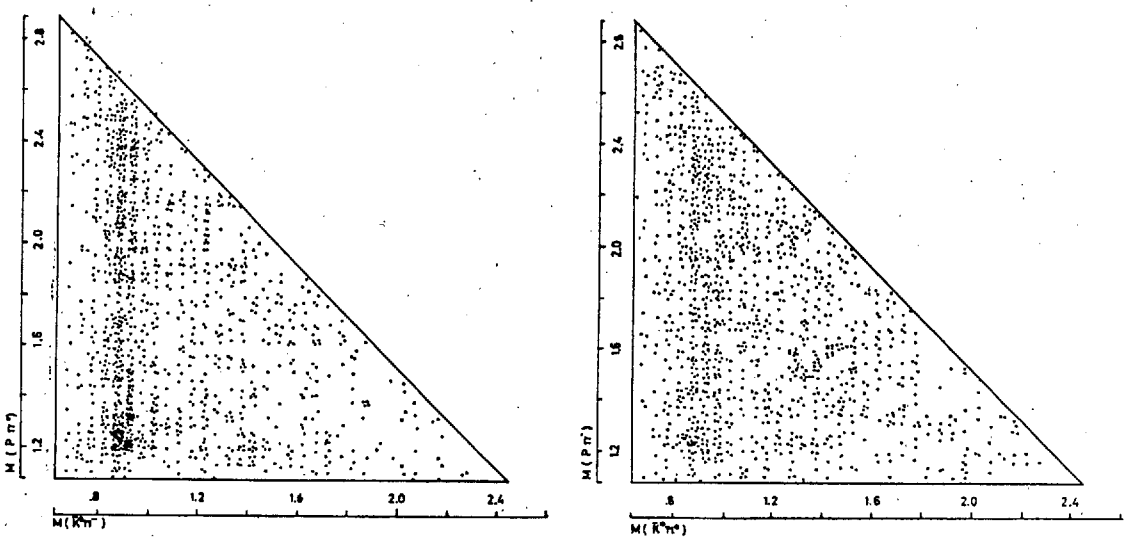

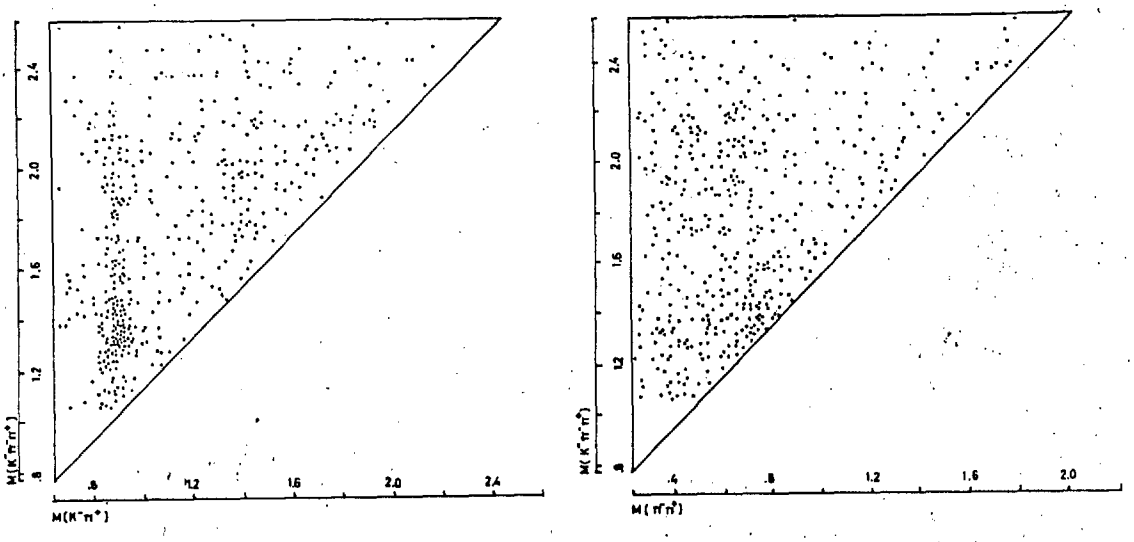

Fig. 7.3

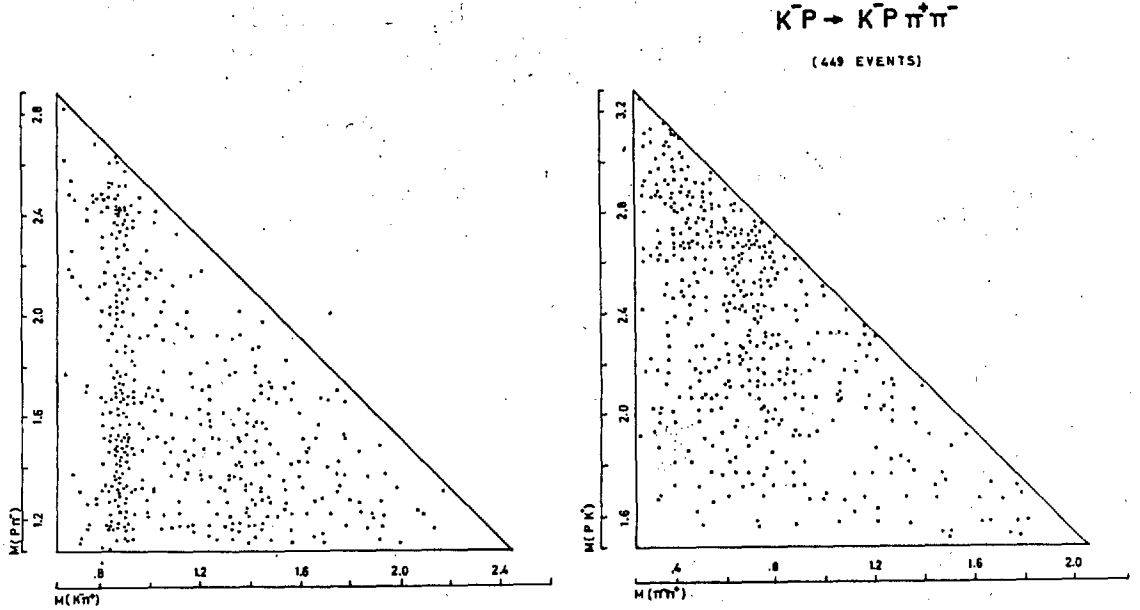

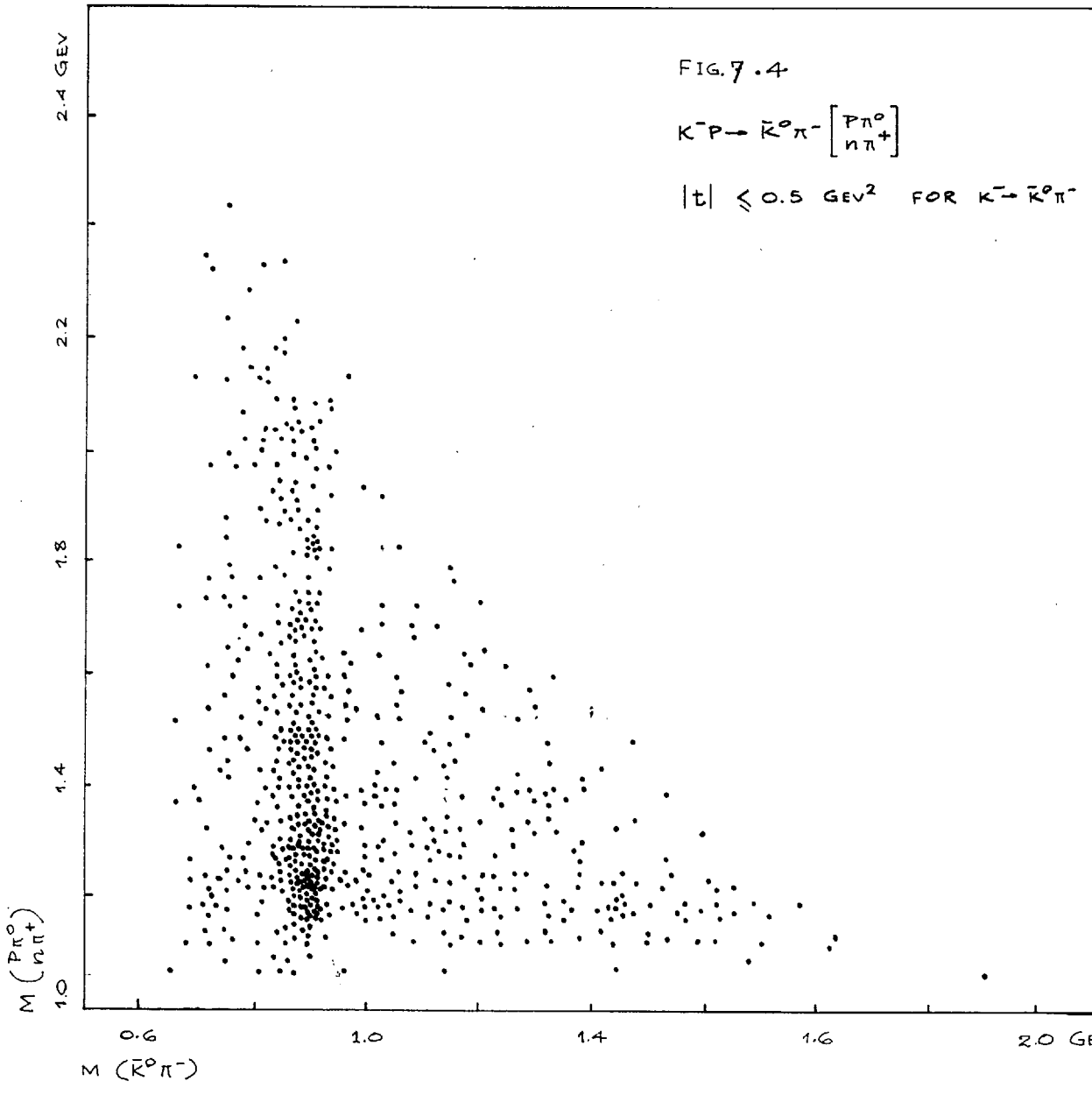
FIG. 7.4
$K^-p \to \bar{K}^0\pi^- \begin{bmatrix} p\pi^0 \\ n\pi^+ \end{bmatrix}$
$|t| \lesssim 0.5$ GEV^2 FOR $K^- \to \bar{K}^0\pi^-$
2.4 GEV
2.2
1.8
1.4
1.0
$M\left(\begin{smallmatrix} p\pi^0 \\ n\pi^+ \end{smallmatrix}\right)$
0.6
1.0
1.4
1.6
2.0 GEV
$M(\bar{K}^0\pi^-)$

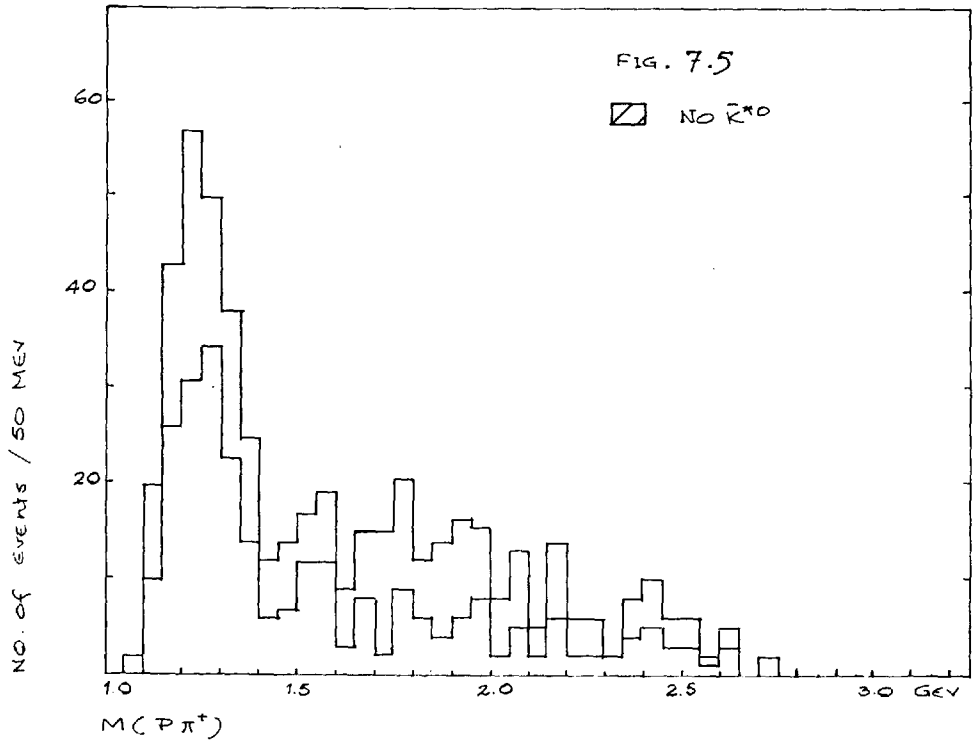
FIG. 7.5
NO $\bar{K}^{*0}$
NO. OF EVENTS / 50 MEV
60
40
20
1.0
1.5
2.0
2.5
3.0 GEV
M(Pπ⁺)

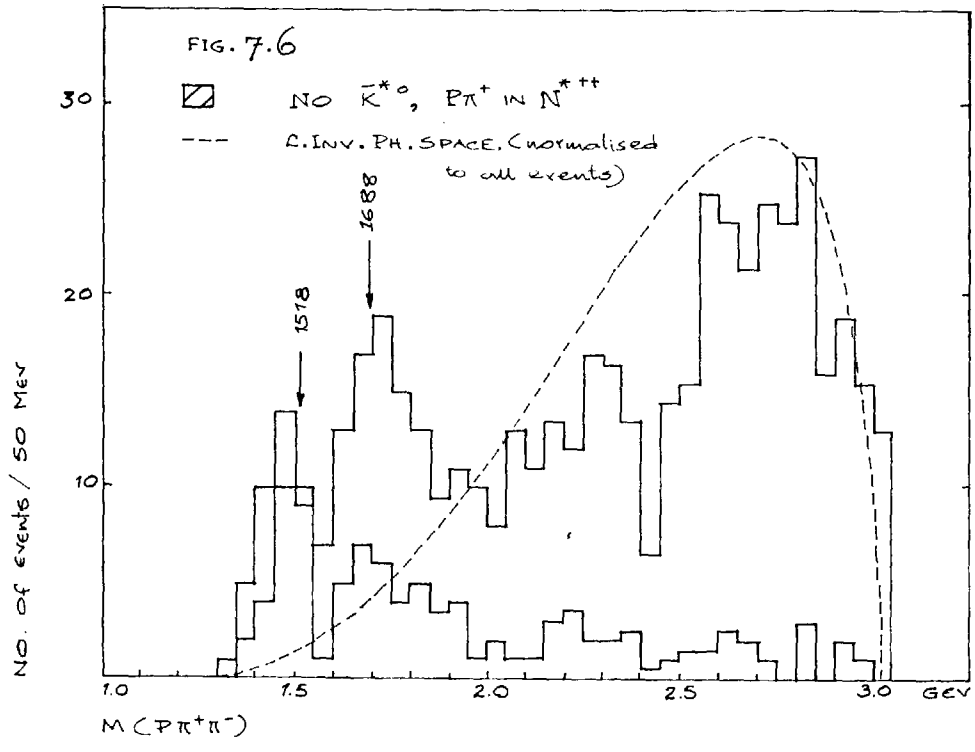
FIG. 7.6
NO $\bar{K}^{*0}$, Pπ⁺ IN N^{*++}
--- L. INV. PH. SPACE. (normalised to all events)
1688
1518
NO. OF EVENTS / 50 MEV
30
20
10
1.0
1.5
2.0
2.5
3.0 GEV
M(Pπ⁺π⁻)

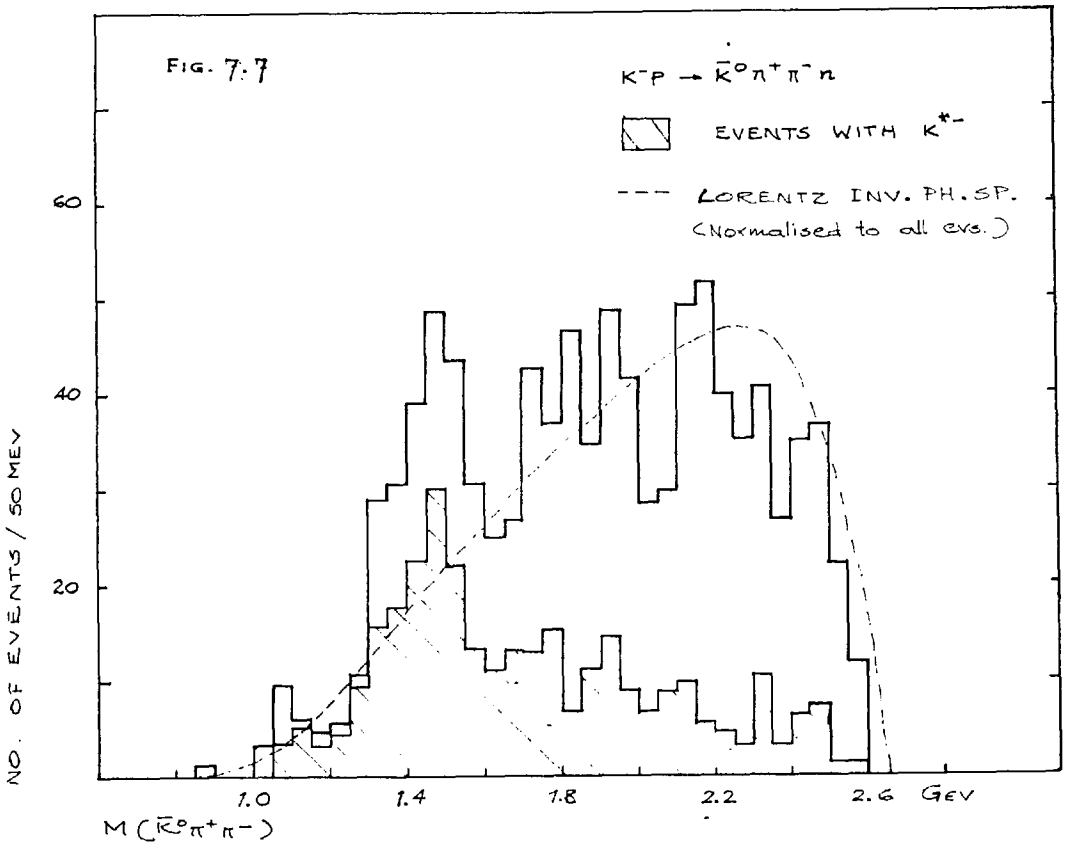

FIG. 7.8

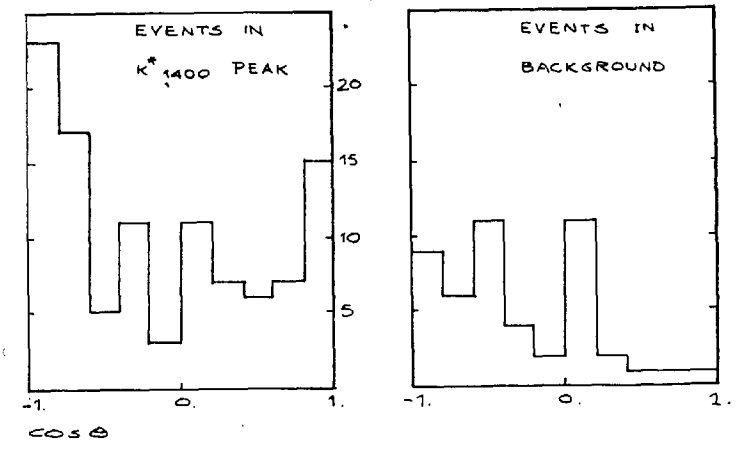

$\bar{K}^{*0}_{1400} \to K^{*-}_{890}\pi^+$

FIG. 7.9

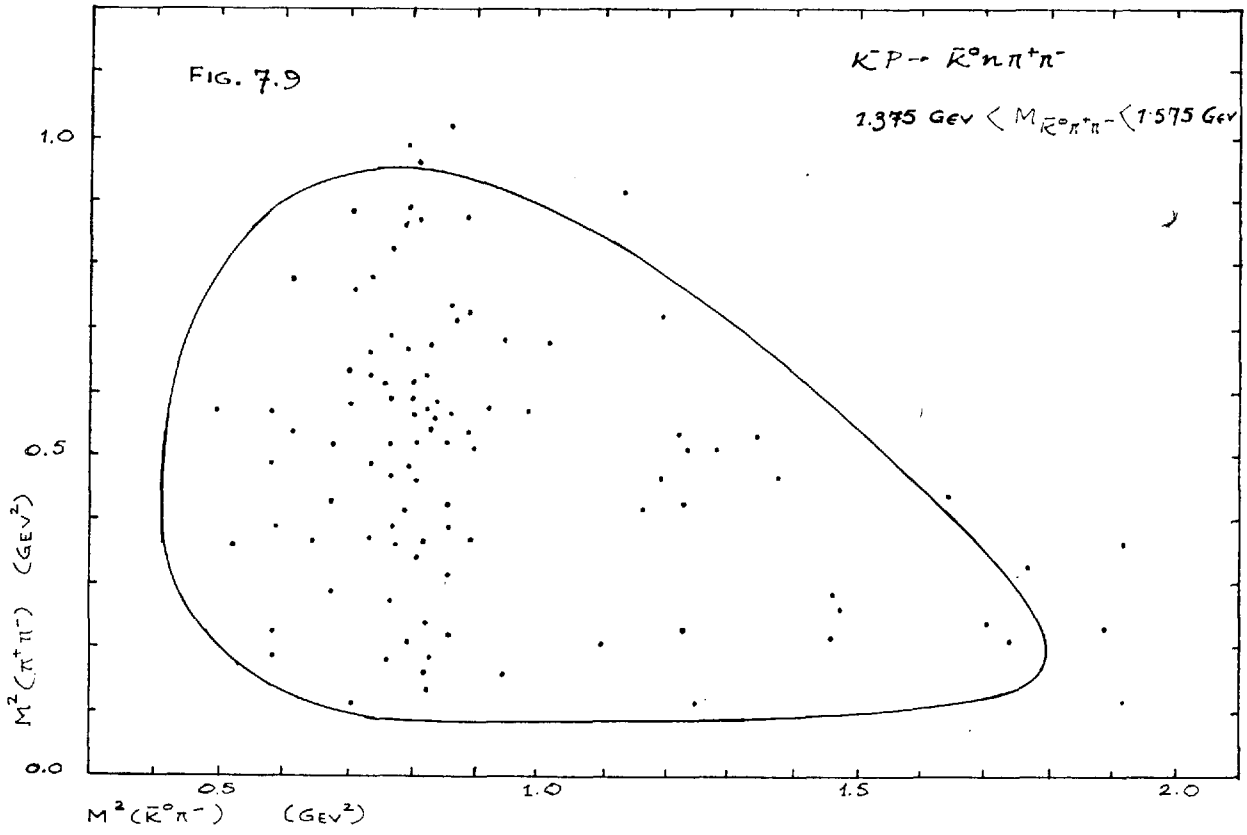

FIG. 7.10

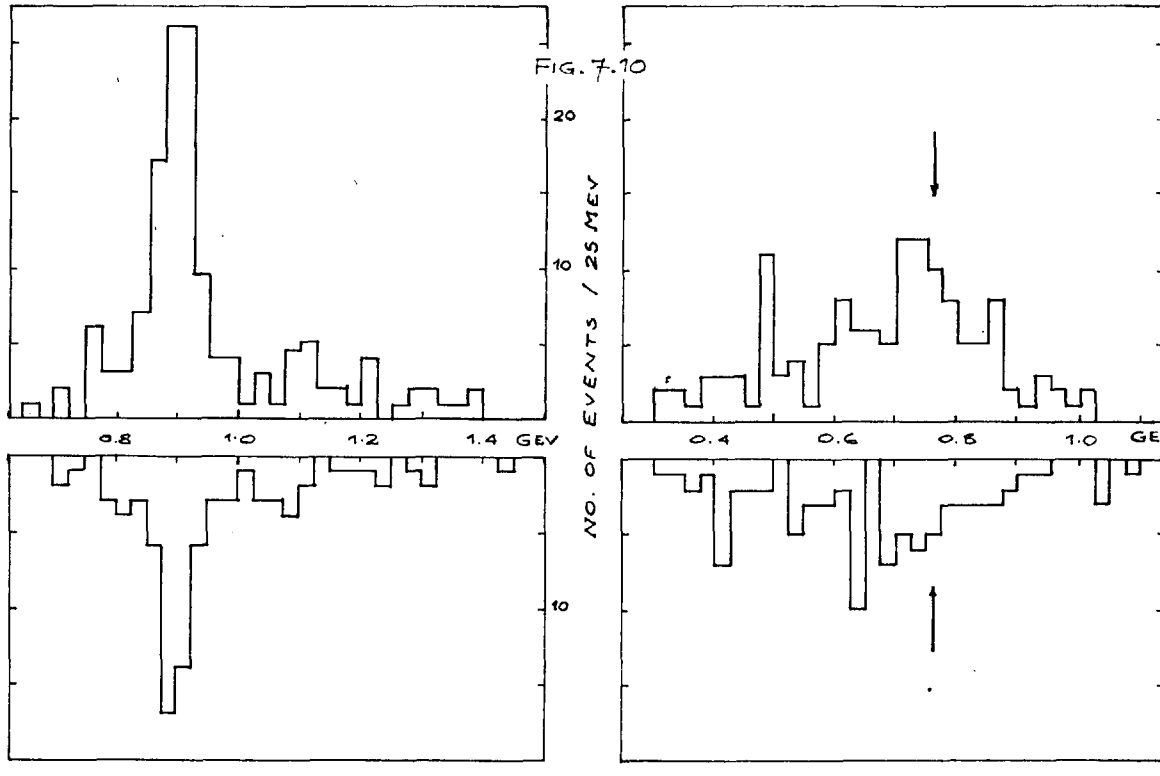

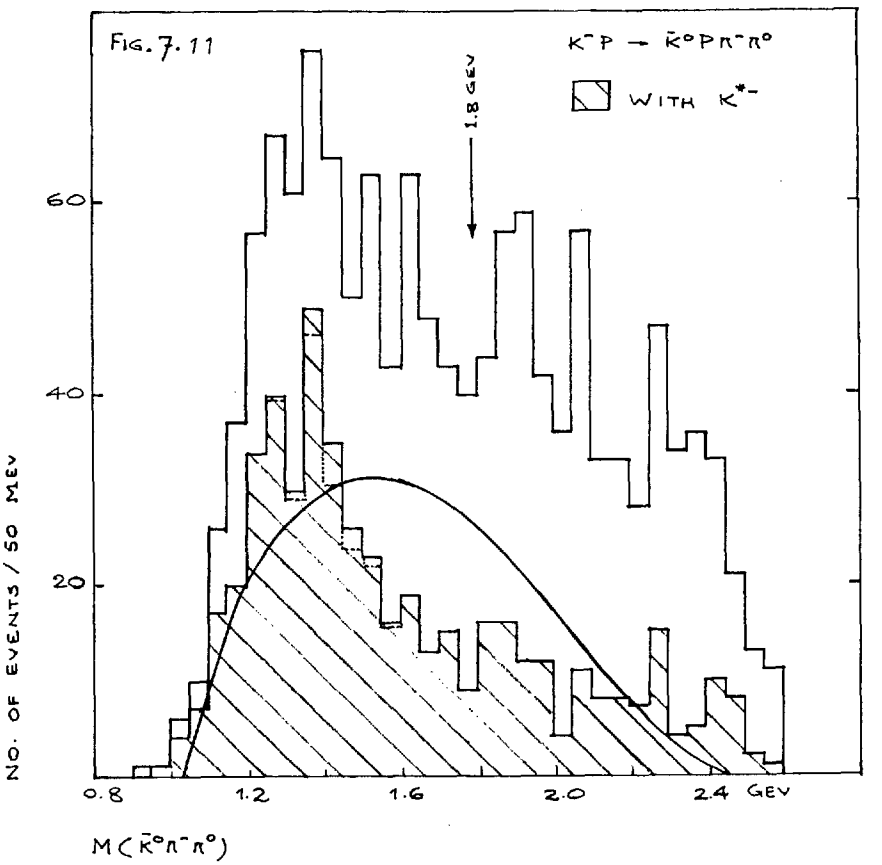
FIG. 7.11
$K^-P \to \bar{K}^0P\pi^-\pi^0$
WITH K^{*-}
1.8 GEV
NO. OF EVENTS / 50 MEV
60
40
20
0.8
1.2
1.6
2.0
2.4 GEV
$M(\bar{K}^0\pi^-\pi^0)$

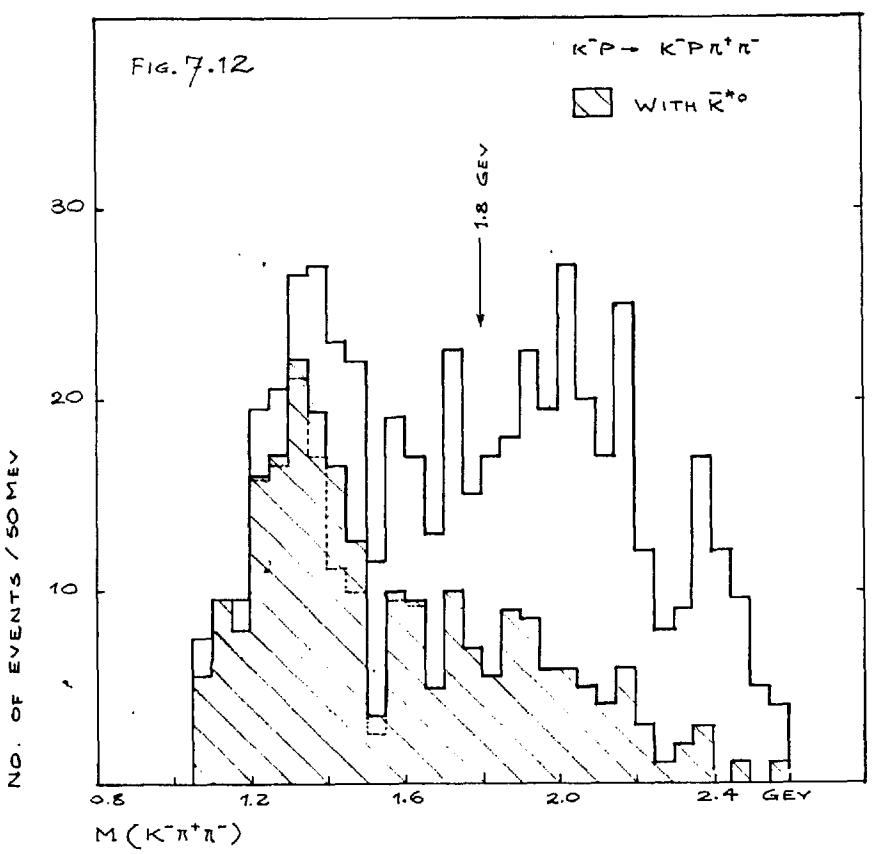
FIG. 7.12
$K^-P \to K^-P\pi^+\pi^-$
WITH $\bar{K}^{*0}$
1.8 GEV
NO. OF EVENTS / 50 MEV
30
20
10
0.8
1.2
1.6
2.0
2.4 GEV
$M(K^-\pi^+\pi^-)$

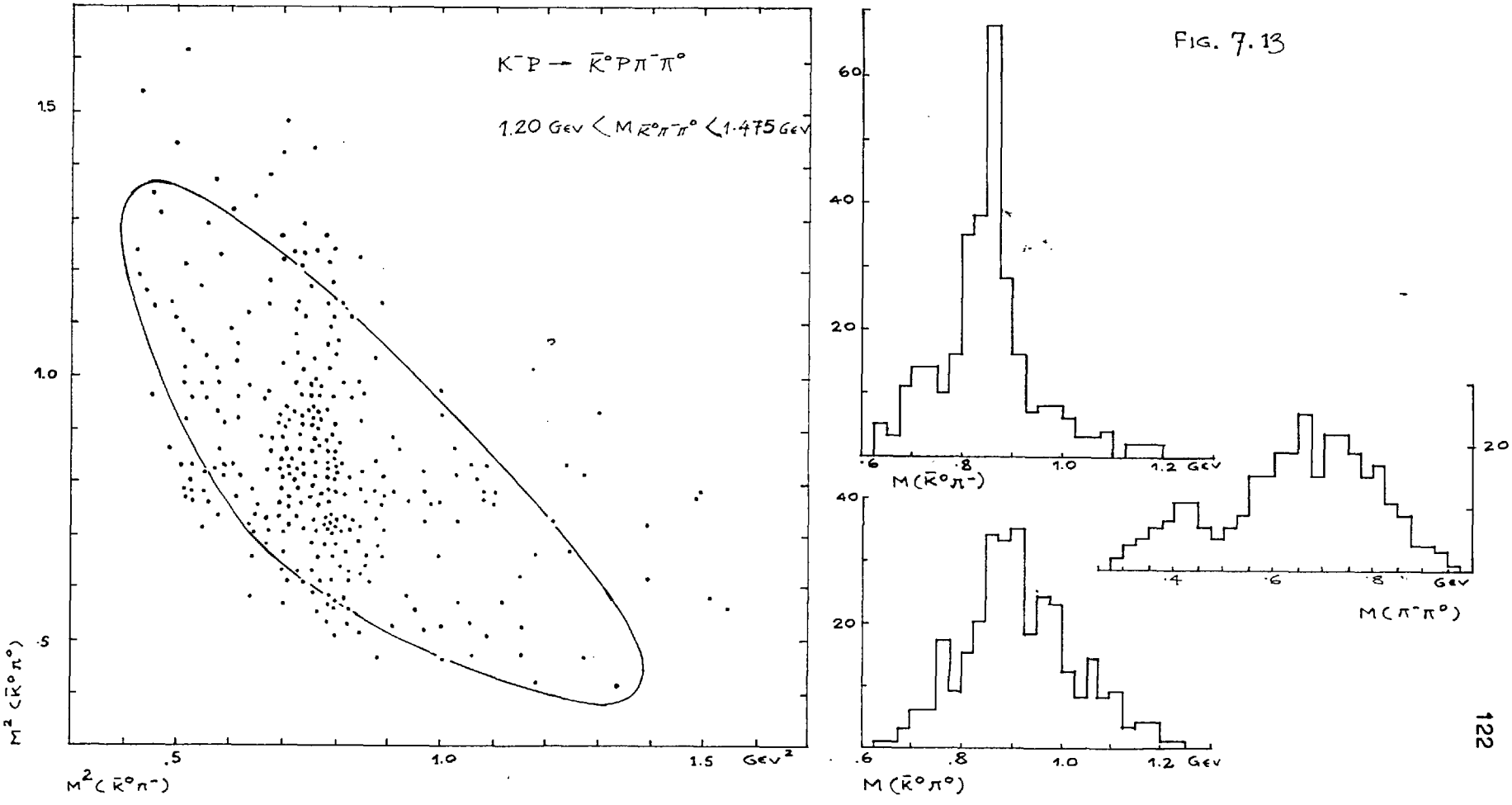
$K^-P \to \bar{K}^0 P \pi^- \pi^0$
1.20 Gev < $M_{\bar{K}^0\pi^-\pi^0}$ < 1.475 Gev
$M^2(\bar{K}^0\pi^-)$
$M^2(\bar{K}^0\pi^0)$
.5
1.0
1.5 Gev^2
1.5
1.0
.5
$M(\bar{K}^0\pi^-)$
$M(\bar{K}^0\pi^0)$
$M(\pi^-\pi^0)$
.6
.8
1.0
1.2 Gev
.4
.6
.8
Gev
20
40
60

FIG. 7.13

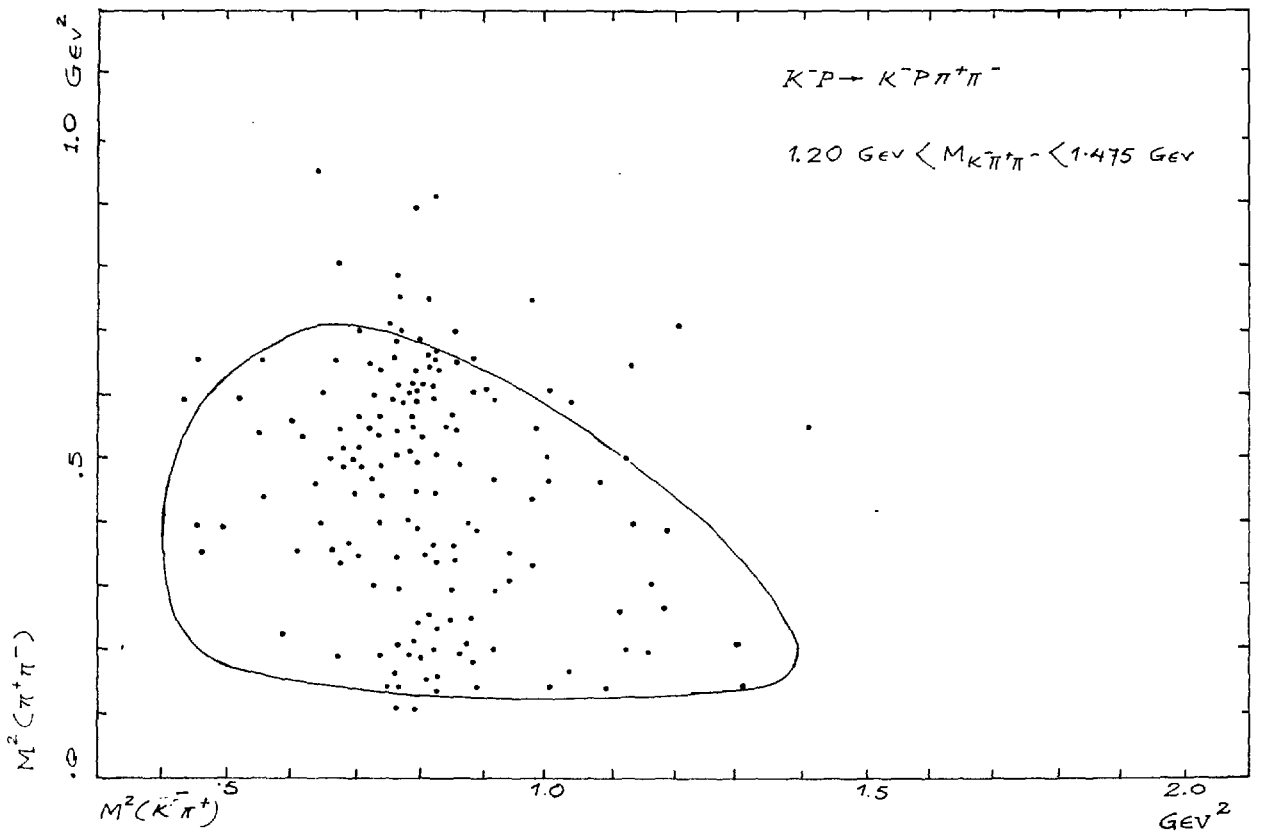
$K^-p \to K^-p\pi^+\pi^-$
1.20 GeV < $M_{K^-\pi^+\pi^-}$ < 1.475 GeV
$M^2(\pi^+\pi^-)$
1.0 GeV^2
.5
0
$M^2(K^-\pi^+)$
.5
1.0
1.5
2.0
GeV^2

FIG. 7.14

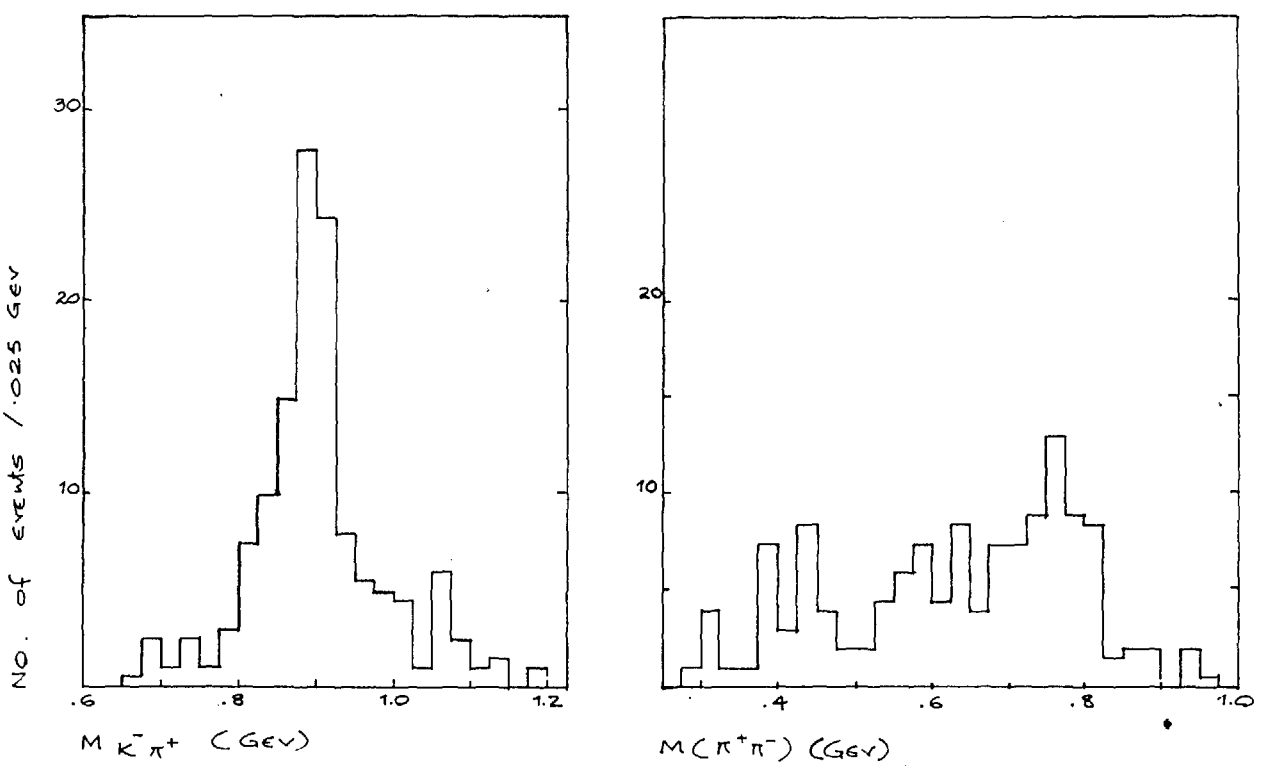
NO. of events / .025 GeV
30
20
10
.6
.8
1.0
1.2
M $K^-\pi^+$ (GeV)
20
10
.4
.6
.8
1.0
M($\pi^+\pi^-$) (GeV)

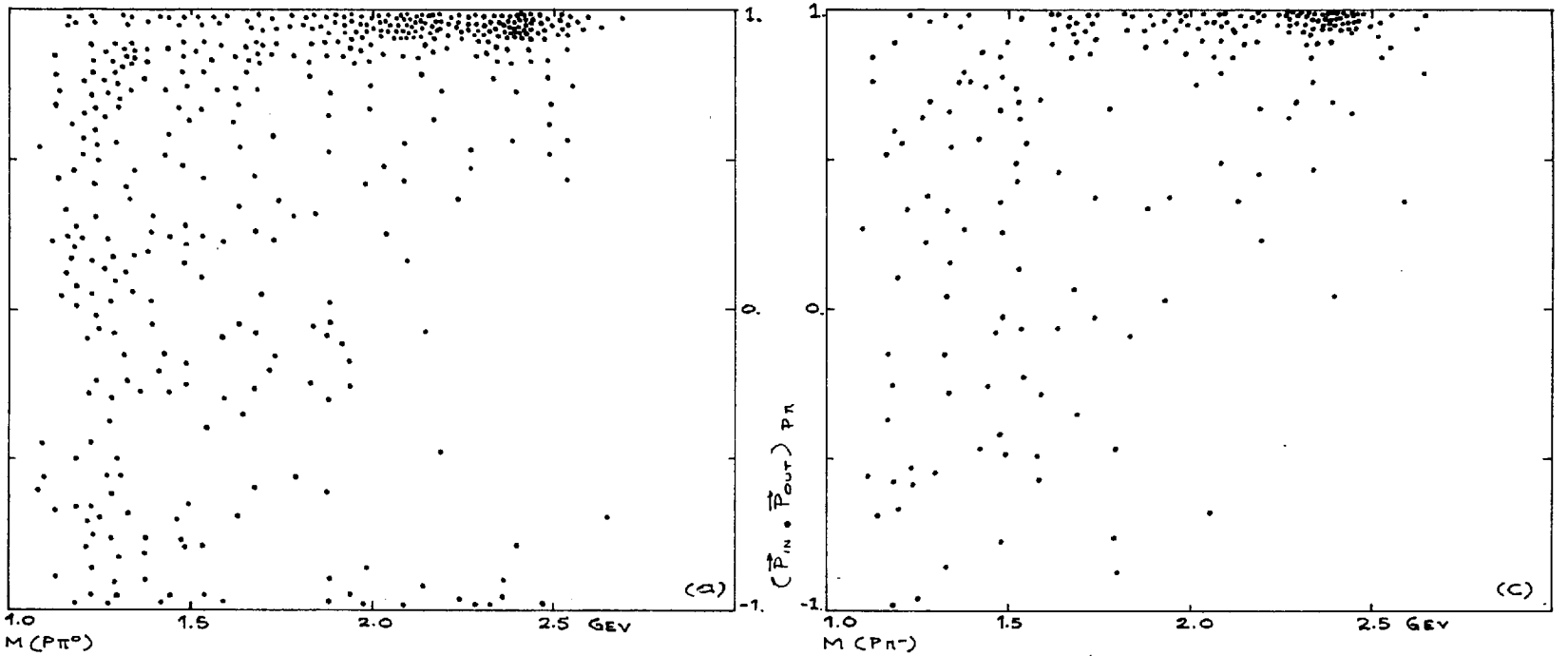
1.
0.
-1.
(a)
1.0
1.5
2.0
2.5 GEV
M (Pπ°)
1
0.
-1
(c)
1.0
1.5
2.0
2.5 GEV
M (Pπ⁻)
(P_in • P_out) Pπ

FIG. 7.15

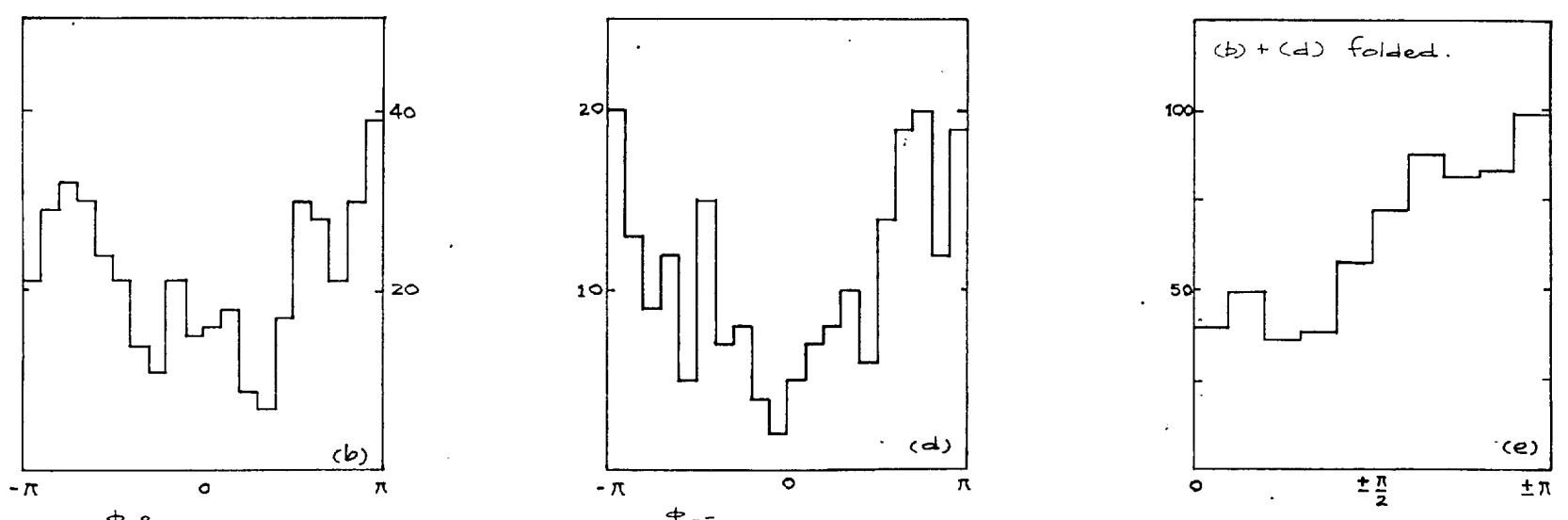
40
20
(b)
-π
0
π
Φπ°
20
10
(d)
-π
0
π
Φπ⁻
(b) + (d) folded.
100
50
(e)
0
±π/2
±π

FIG. 7.16

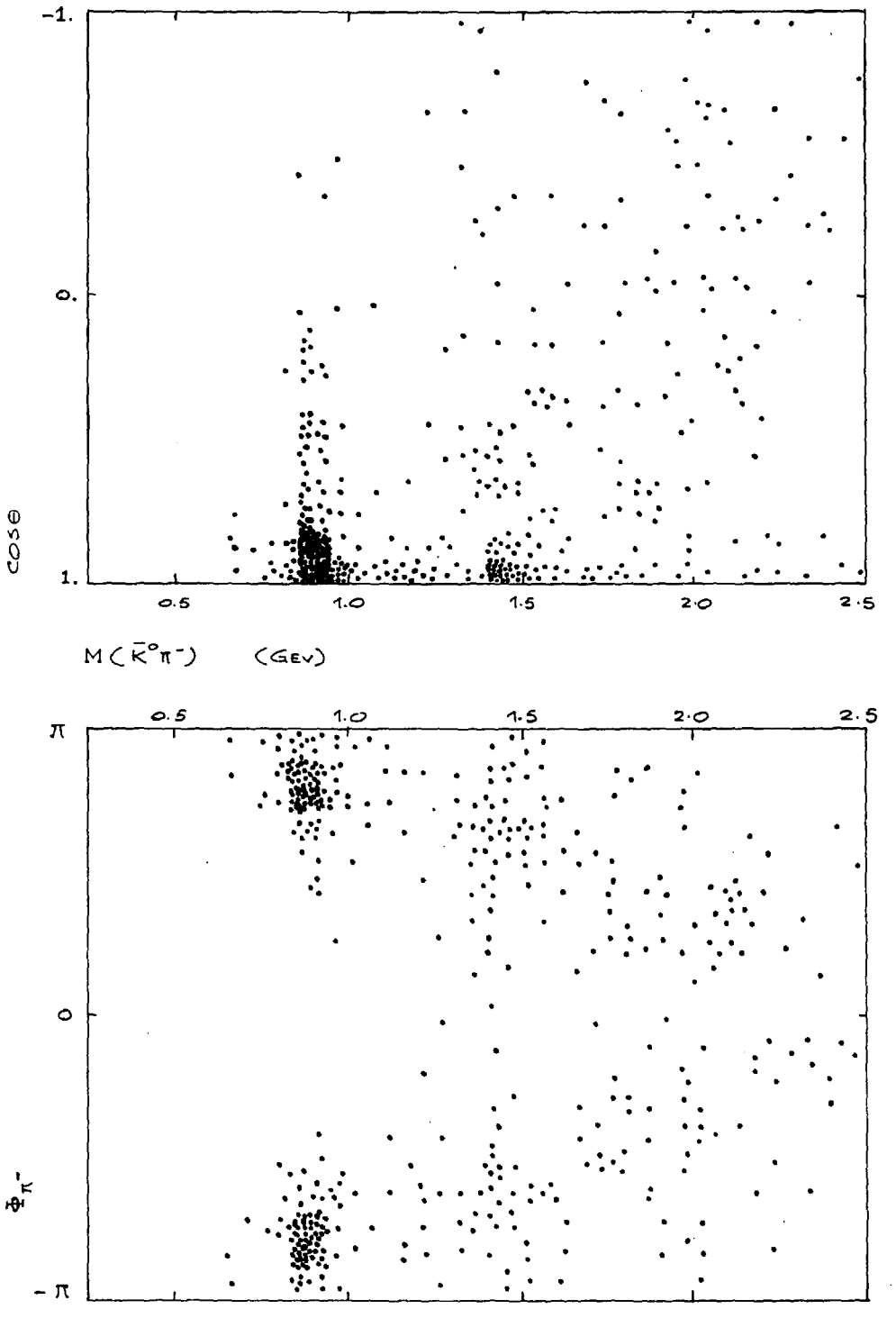

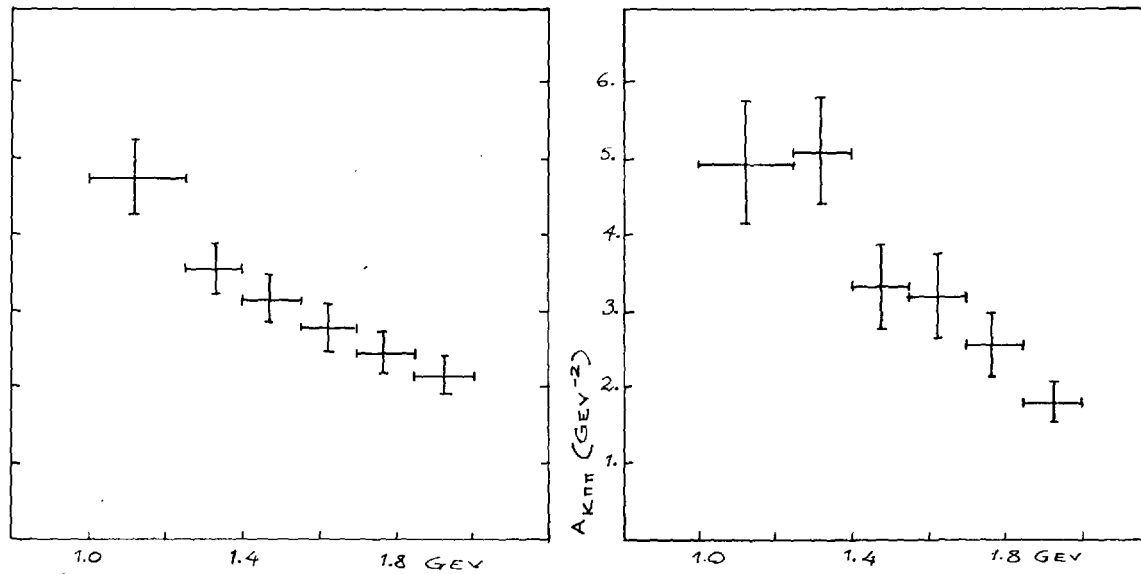

FIG. 7.17

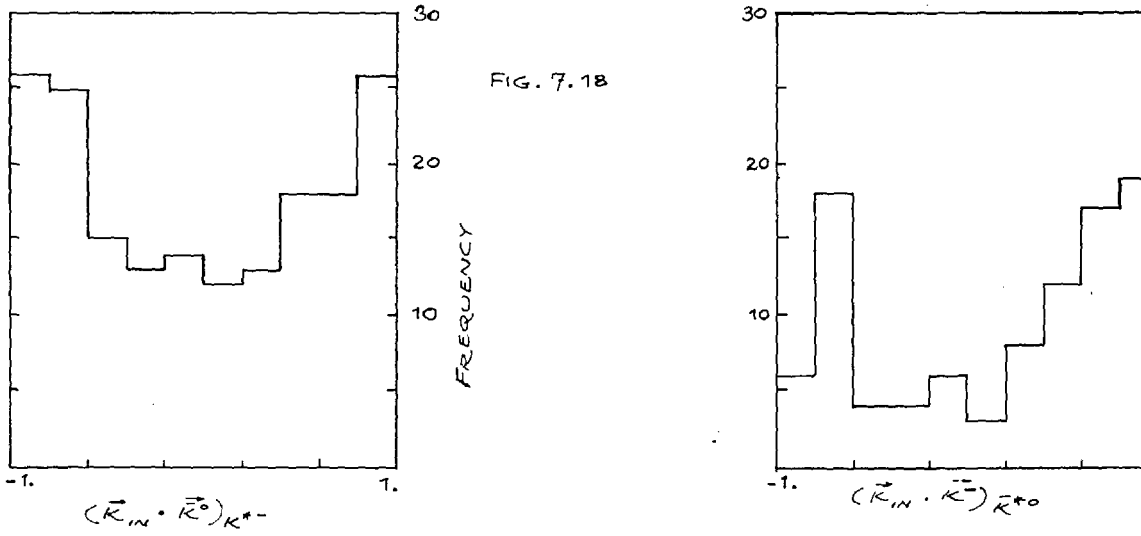

FIG. 7.18

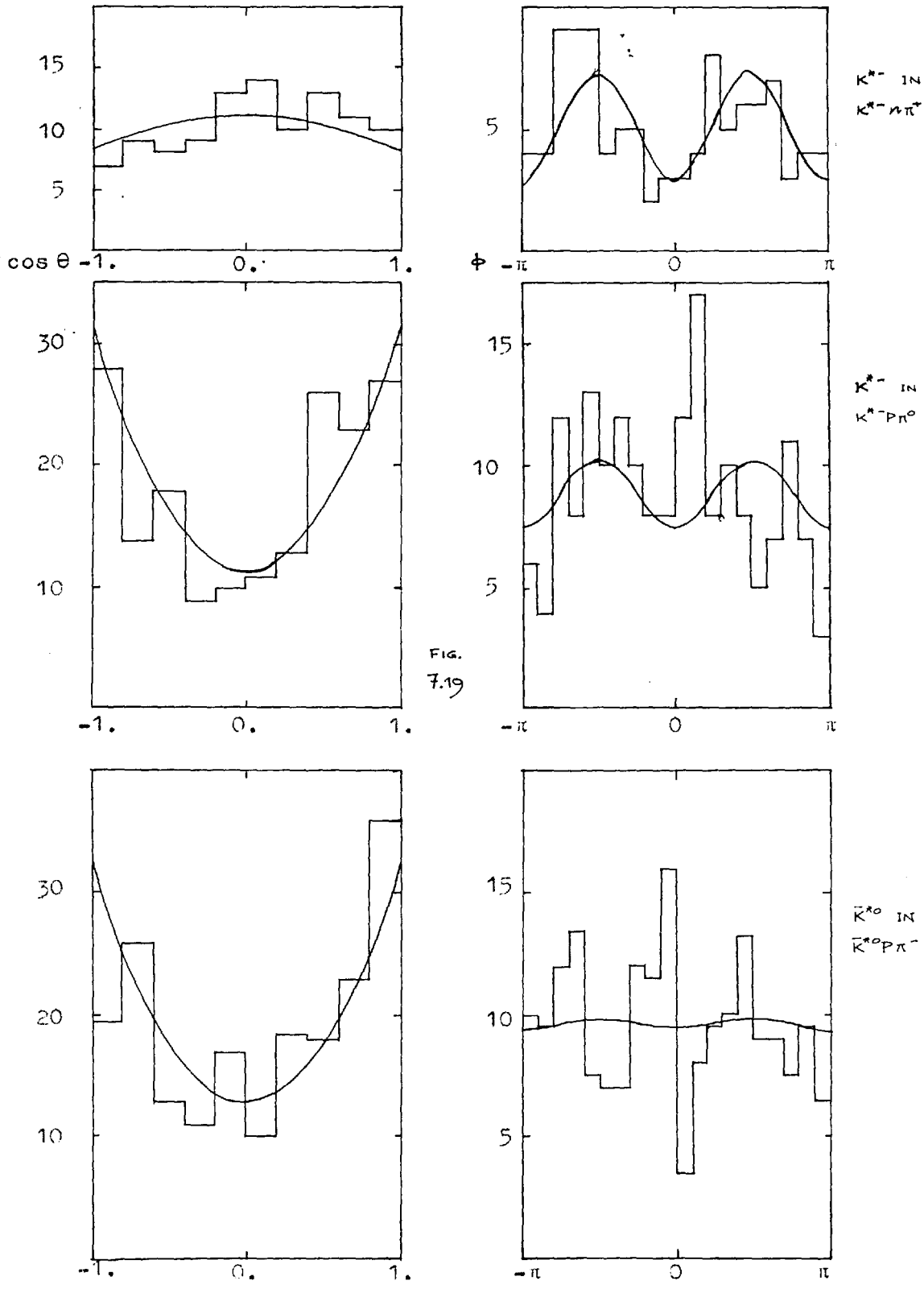
15
10
5
cos θ -1. 0. 1.
5
φ -π 0 π
K*⁻ IN
K*⁻π⁺π⁻
30
20
10
-1. 0. 1.
15
10
5
-π 0 π
K*⁻ IN
K*⁻pπ⁰
30
20
10
-1. 0. 1.
15
10
5
-π 0 π
K̄*⁰ IN
K̄*⁰pπ⁻

FIG. 7.19

Fig. 7.20

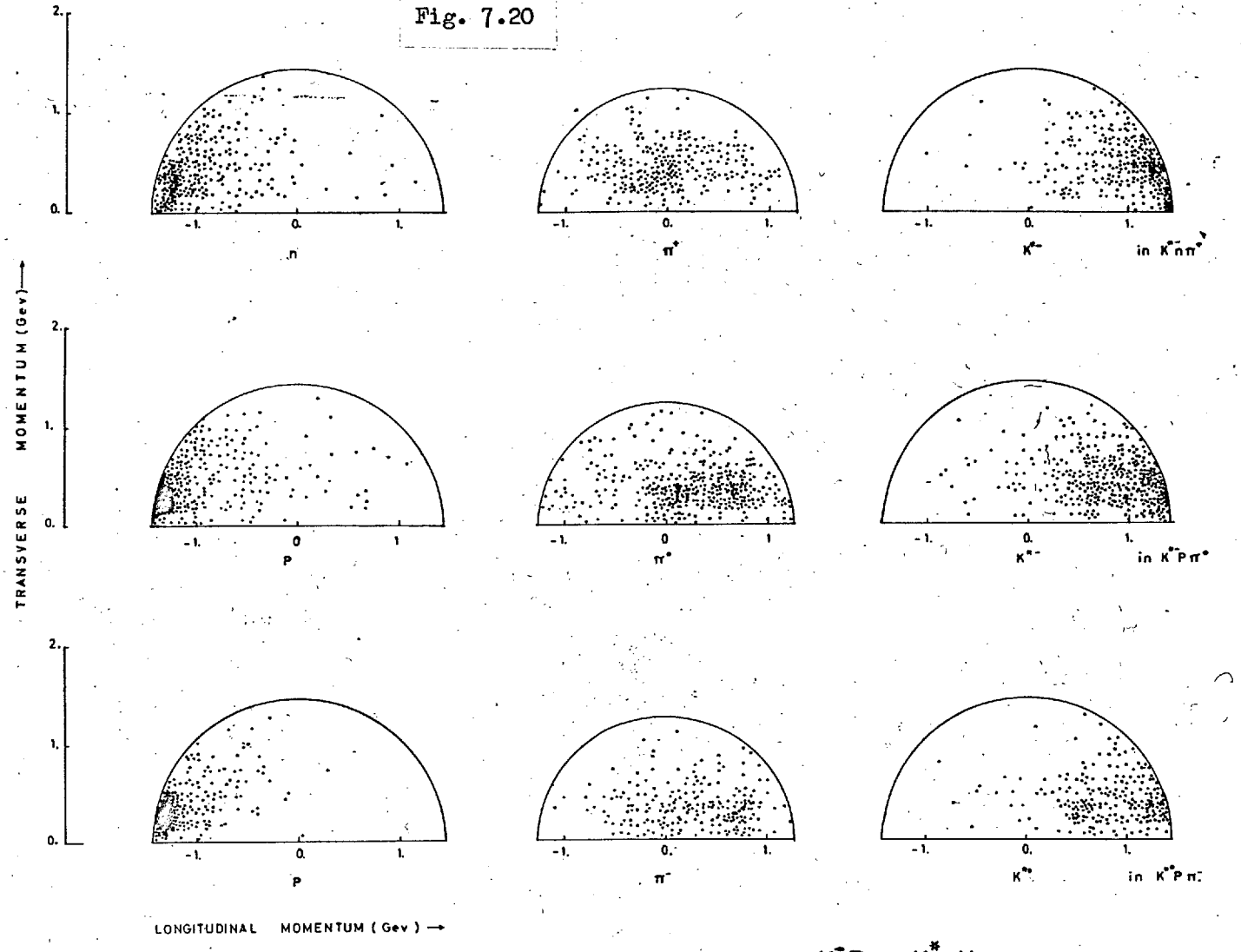

$K^-P \rightarrow K^*\pi N$

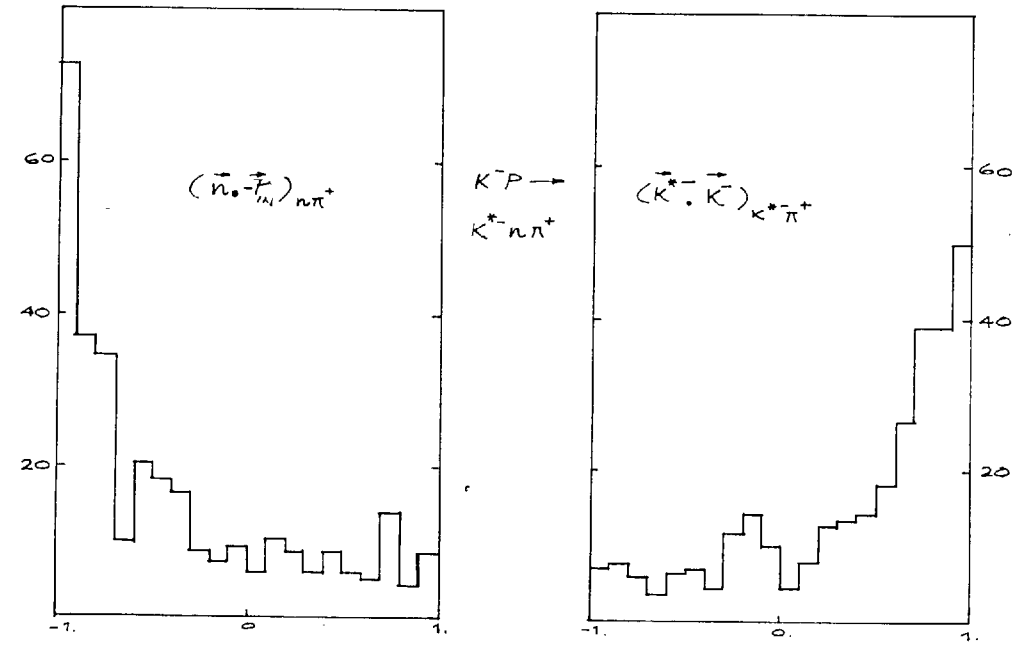
$(\vec{n}_\bullet \cdot \vec{P}_{IN})_{n\pi^+}$
$K^-P \longrightarrow$
$K^{*-}n\pi^+$
$(\vec{K}^{*-} \cdot \vec{K}^-)_{K^{*-}\pi^+}$
60
40
20
-1.
0.
1.

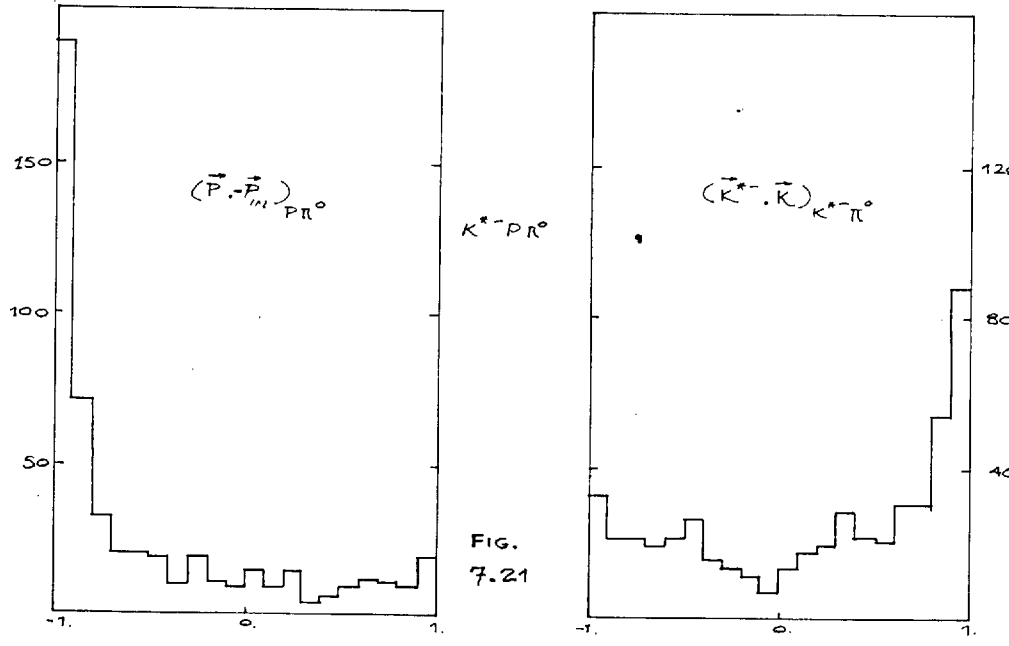
$(\vec{P} \cdot \vec{P}_{IN})_{P\pi^0}$
$K^{*-}P\pi^0$
$(\vec{K}^{*-} \cdot \vec{K})_{K^{*-}\pi^0}$
150
100
50
120
80
40
-1.
0.
1.

FIG. 7.21

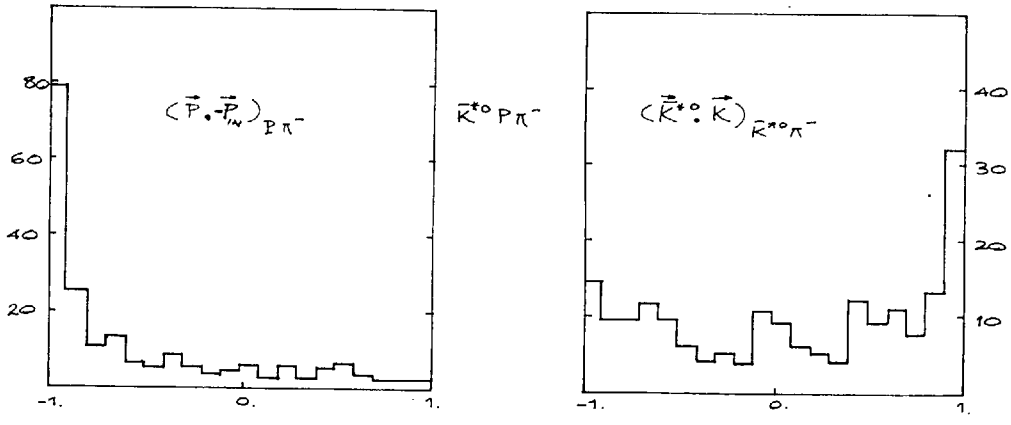
$(\vec{P} \cdot \vec{P}_{IN})_{P\pi^-}$
$\bar{K}^{*0}P\pi^-$
$(\vec{\bar{K}}^{*0} \cdot \vec{K})_{\bar{K}^{*0}\pi^-}$
80
60
40
20
40
30
20
10
-1.
0.
1.

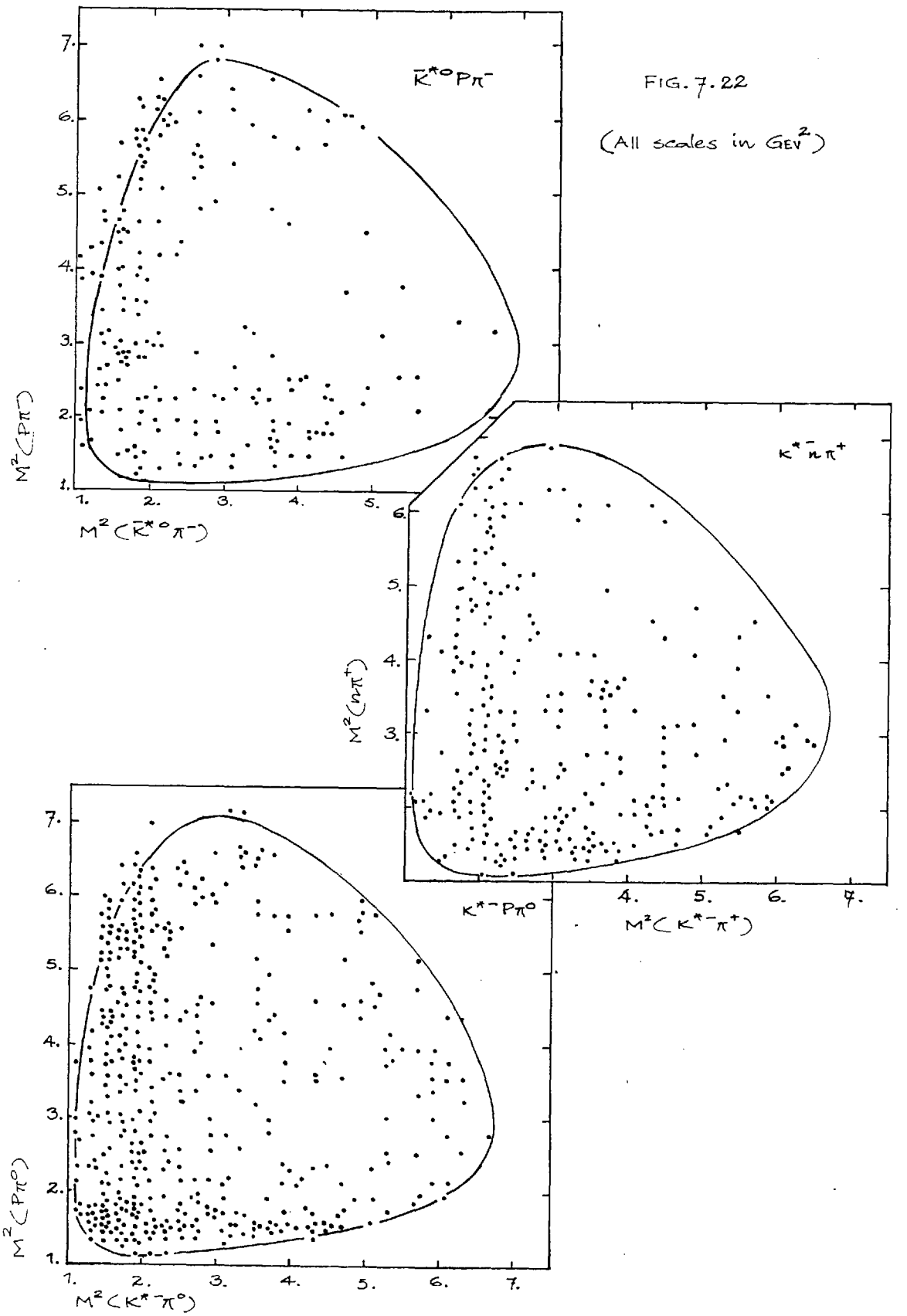

FIG. 7.22

(All scales in GeV^2)

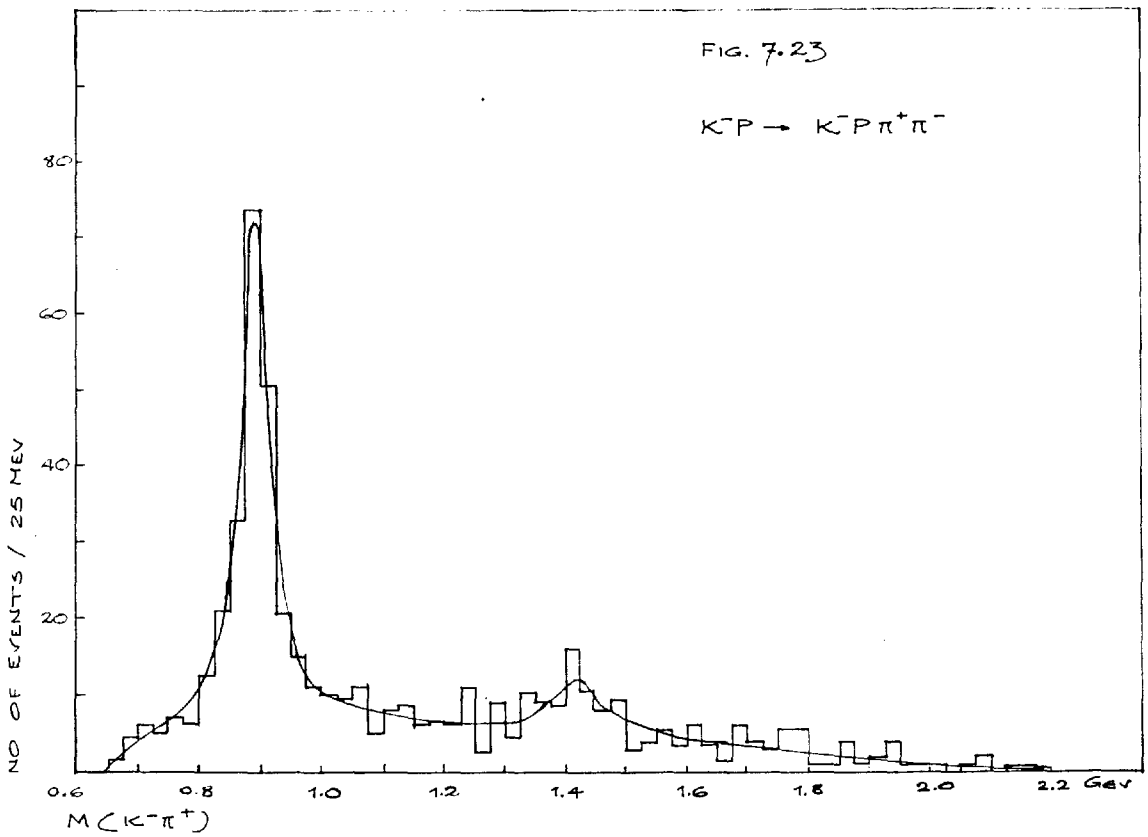
FIG. 7.23
$K^-P \rightarrow K^-P\pi^+\pi^-$
NO OF EVENTS / 25 MEV
80
60
40
20
0.6
0.8
1.0
1.2
1.4
1.6
1.8
2.0
2.2 GEV
$M(K^-\pi^+)$

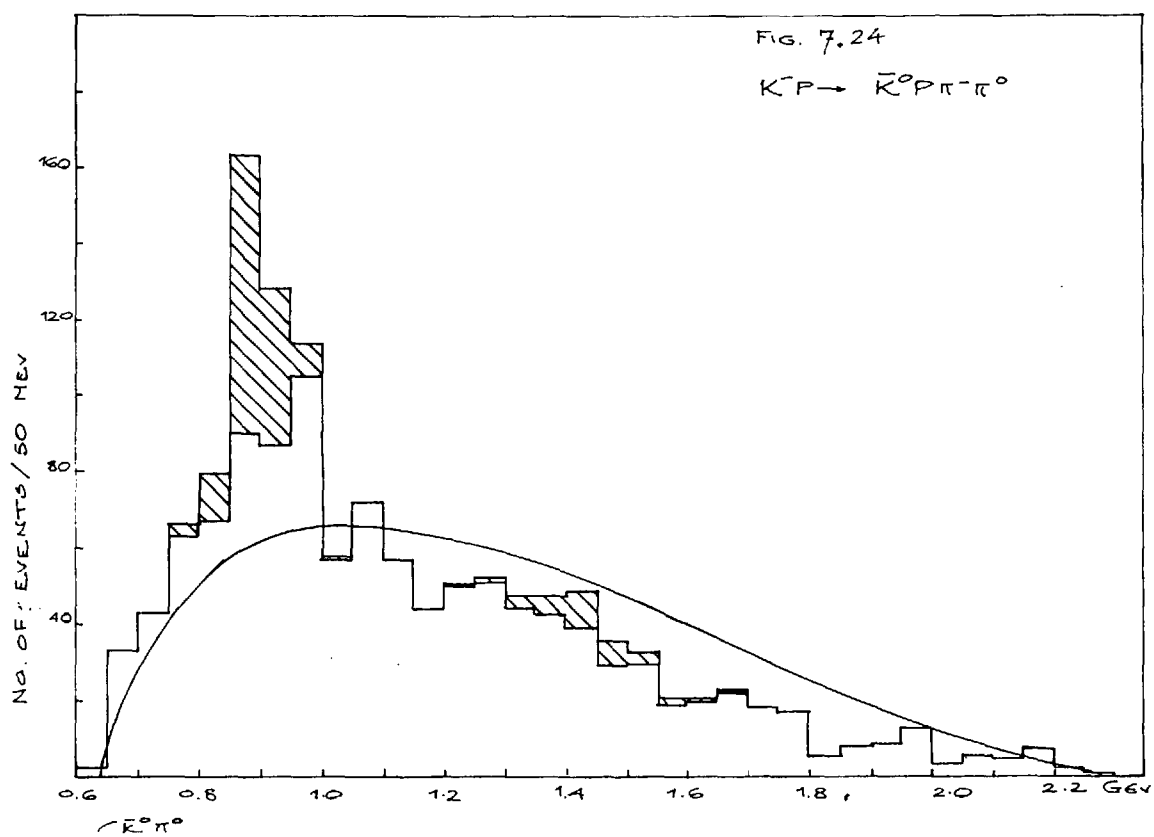
FIG. 7.24
$K^-P \rightarrow \bar{K}^0P\pi^-\pi^0$
NO. OF EVENTS / 50 MEV
160
120
80
40
0.6
0.8
1.0
1.2
1.4
1.6
1.8
2.0
2.2 GEV
$(\bar{K}^0\pi^0)$

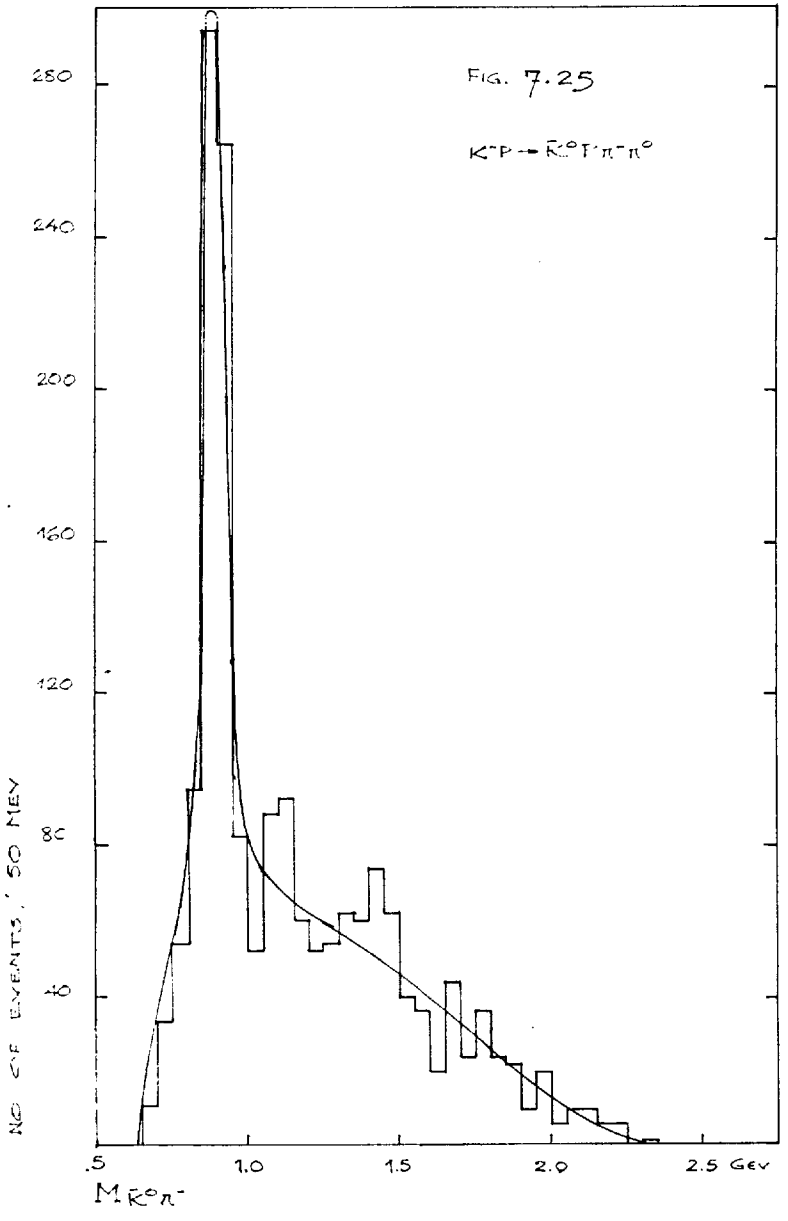

FIG. 7.25

$K^-p \to K^0 p \pi^- \pi^0$

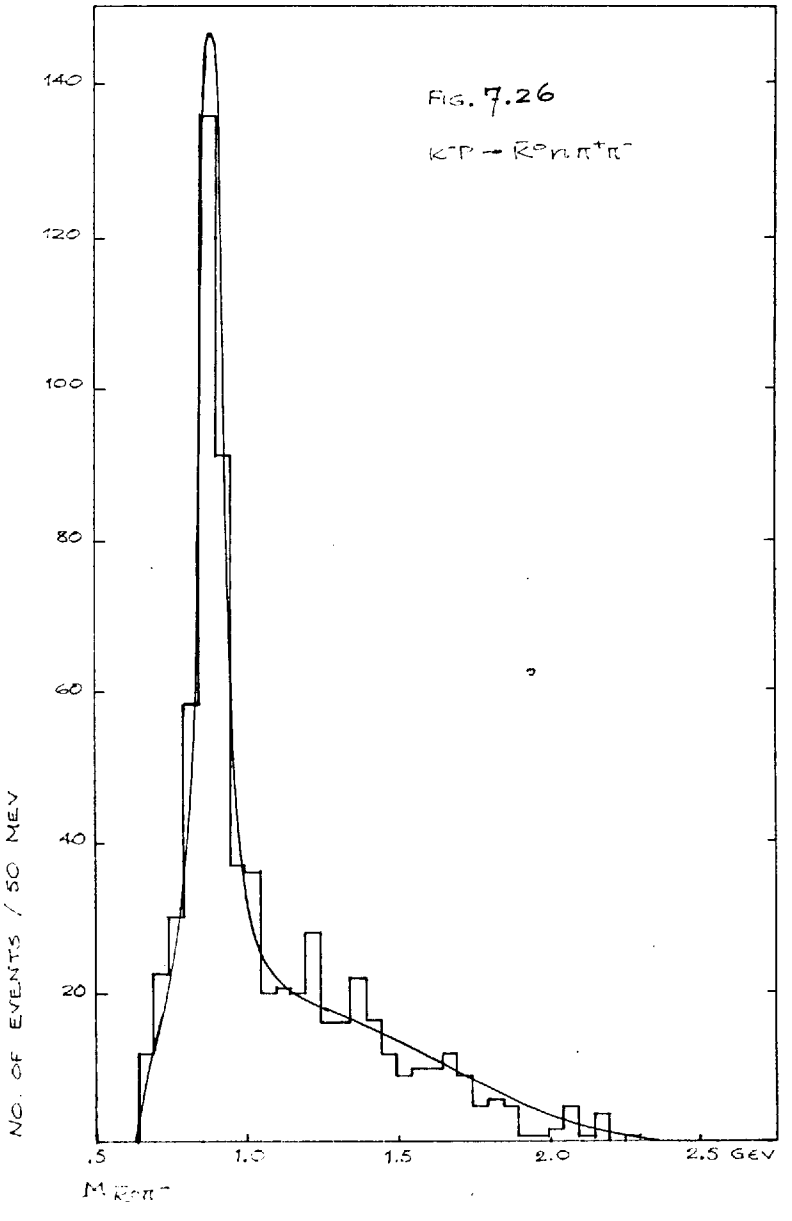

FIG. 7.26

$K^-p \to K^0 n \pi^+ \pi^-$

FIG. 7.27

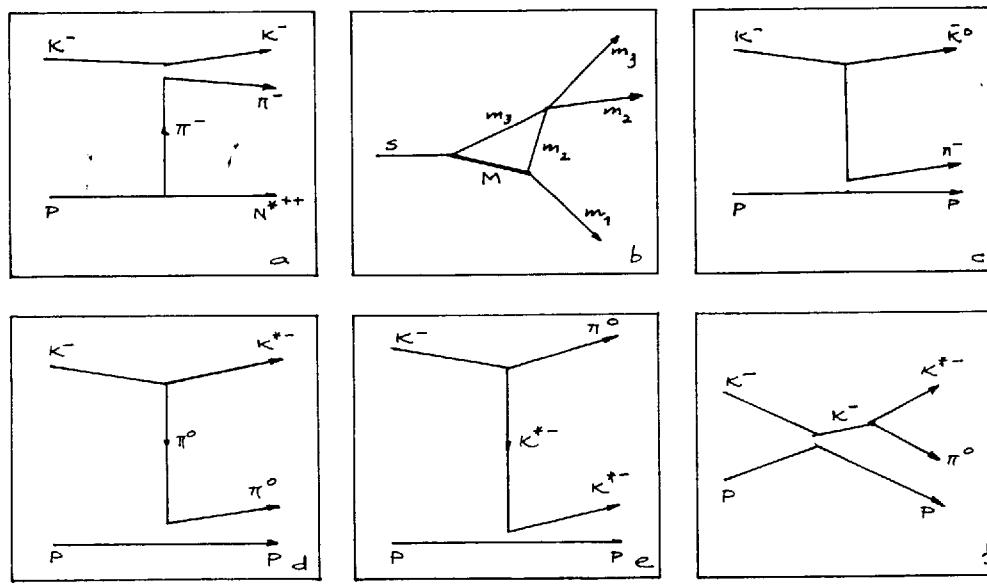

FIG. 7.28

$K^-P \to \bar{K}^0\pi^- P$ $\bar{K}^0\pi^- n\pi^+$
$K^0\pi^- P\pi^0$ $K^-\pi^+ P\pi^-$

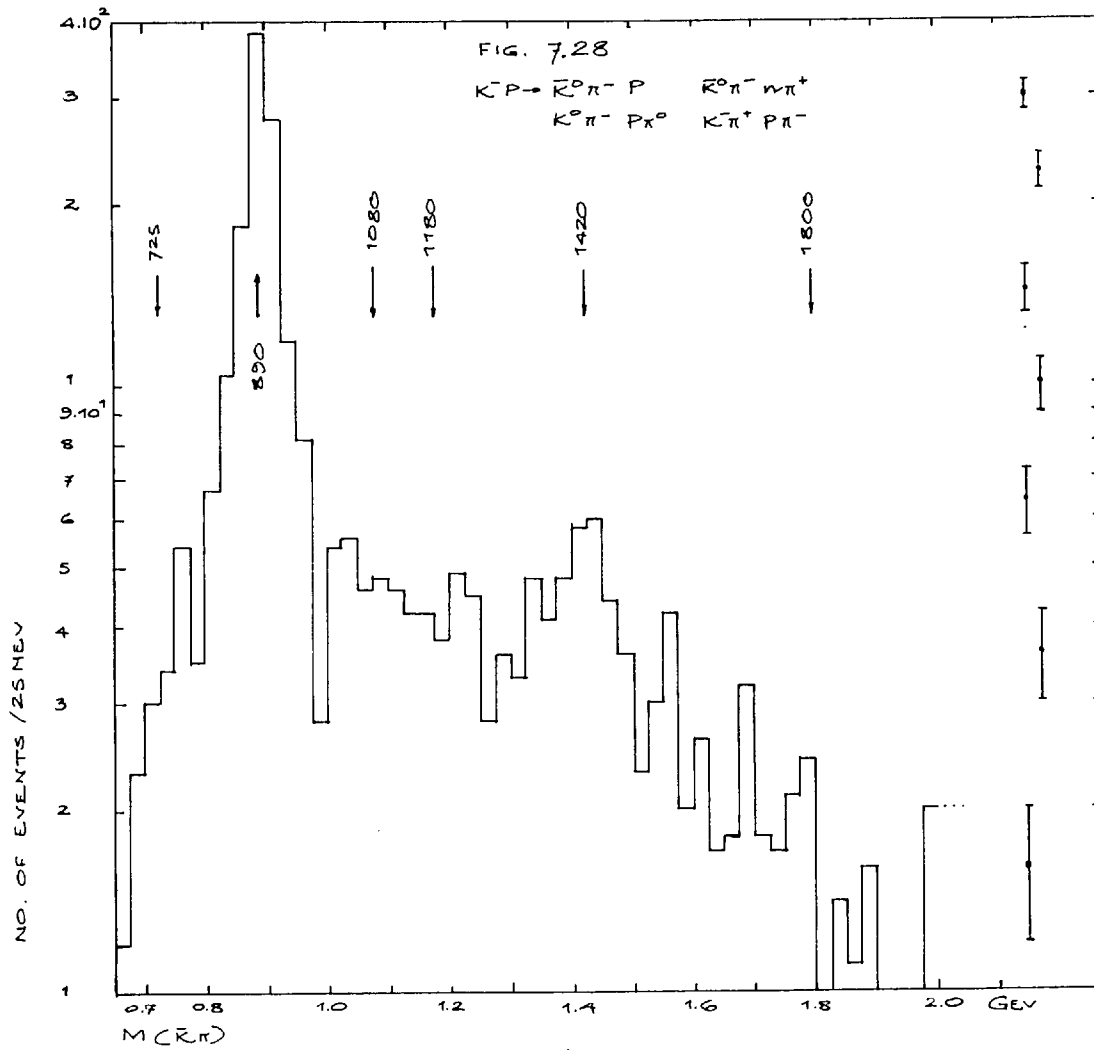

Chapter 8 Conclusions

The analysis of the 6 Gev K^-P data gives the feeling that not much conclusive can be said from the results of this experiment alone. However, it is one of a series of experiments from which some features of high energy elementary particle interactions emerge quite distinctly. This chapter will be devoted to a general discussion of them.

Resonances

The K^*_{890} has been seen very prominently in this experiment but this resonance has been well-established through other experiments and little is left to be said about it as a resonance state. The situation with K^*_{1400} is, however, different. Although it is accepted as a resonance, its spin and parity assignments are still not beyond suspicion. In the works mentioned in ref.(21), the J^P of 1^- has been slightly favoured whereas in this experiment 2^+ and 1^- have been found to about equally likely. The 2^+ assignment would still not be questioned until there is definite evidence against it. The mass of the K^*_{1400} has been observed to be slightly higher in this experiment than currently accepted. However, after the compilation at the Berkeley Conference[38], the weighted mean is definitely higher

than 1400 Mev ($\sim$1410 Mev) so that the mean value of the present experiment (1425±7 Mev) is not too inconsistent.

The controversy about the K^*_{1320} cannot be said to have disappeared. One has to bring in a variety of models to find a complete explanation which again is too complex to be experimentally verified. If it really is the effect of a peripheral background plus several resonances produced through some kind of a diffractive process without charge exchange with the nucleon, it would be difficult to disentangle the effects — even with prospects of better mass resolution and a reasonable amount of optimism.

The absence of the "L meson" in the $(K\pi\pi)^-$ spectra in the channels $(K\pi\pi)^-P$ is striking. It is estimated that to produce an effect of less than $1\sigma_{\Lambda}^{(\text{st.dev.})}$ in the $\bar{K}^o\pi^-\pi^o$ mass spectrum of the channel $\bar{K}^o\pi^-\pi^oP$ the cross section for $K^-P \rightarrow L^-P$, $L^- \rightarrow \bar{K}^o\pi^-\pi^o$ has to be lower than 10 μb. However, the L has been seen in this experiment in the $(K3\pi)^-$ combination in the final state $\bar{K}^oP\pi^-\pi^+\pi^-$ and in the missing mass to identified protons in the 2-prong events in the 5.5 Gev K^-P experiment(ref. 39). This probably suggests that the resonance has dominant decay modes with many particles in the final state e.g. $K^*\rho$.

The resonances $\varkappa(725)$ and $(K\pi)_{1080}$ do not appear in this experiment either. The $\varkappa$ has been noticed not to appear when a large Q-value is available and, therefore, is not

expected in any of the final states analysed. The $K\pi(1080)$ has been seen by De-Baere et. al. [38] in $K^+P \rightarrow K^0\pi^+P$ which differs from the state $\bar{K}^0\pi^-P$ seen in this experiment in that there is strong interference from the channel K^0N^{*++}. The problem of interference does not arise in the present experiment since the N^{*0} is very weak. The situation is therefore much clearer and we are confident that no such enhancement exists in our data.

Two-body reactions

The cross-sections of two-body processes have been observed to fall rapidly at high energies. The processes $K^-P \rightarrow \bar{K}^0n$, $K^{*-}_{890}P$ and $K^{*-}_{1400}P$ have been observed in this experiment and it is clear from figs. 6.1,, 6.9 and 6.12 that one can express $\log\sigma$ approximately as a linear function of log(beam momentum)

$$\text{i.e.} \qquad \sigma \propto P_{in}^{-n}.$$

There has been an attempt by Morrison [40] to explain this behaviour with a Regge-pole picture. The dependence arises from the relation $\frac{d\sigma}{dt} \propto s^{2\alpha-2}$, α being the continuous 'angular momentum' of the exchanged Regge-trajectory. In the processes mentioned, the values of n observed are approximately 2.5, 2.8 and 1.3 respectively. They roughly agree with the values for n expected for exchange of non-strange mesons π, ρ and $\omega(\varphi)$ if the cross-section is assumed to arise mainly

from small values of t. The explanation is not exact and is expected to hold good only qualitatively.

At high energies the t-dependence cannot be explained by any kind of Born-term model. The absorption model has a partial success in the case of the K^{*-}_{890} P final state in the sense that it predicts the density matrix elements and the absolute cross-section more or less correctly with the same set of input parameters. However, it fails badly in the case of charge-exchange scattering, where the final state parameters are better known and pseudoscalar exchange is not allowed. This certainly is a serious drawback.

On the other hand, the 'Regge-bandwagon' has started rolling again. The K^-P charge-exchange scattering has been fitted into the Regge-pole-exchange theory by Phillips and Rarita and Roy (Ch.6.). It appears from the latter's theory that the Regge-pole theory is potentially adequate whereas the formers have shown that with certain assumptions about the residue functions, the t-distributions for K^-P charge-exchange scattering can be completely explained. In the case of other two-body processes various trajectories contribute, some of which are not determined experimentally - the ω as an example. Consequently, not much more than a many-degrees-of-freedom data fitting can be done.

A trend towards total vector exchange has been a noticeable fact in the production of the final state $K^{*-}P$. There is also an indication that ω or φ exchange dominates over ρ and is supported by the idea of A-parity[41]. If A-parity is assumed to be good, one can argue back and rule out φ-exchange since φ has A= +1. However, there are serious difficulties in pursuing the idea of A-parity as illustrated below.

The processes $K^-P \rightarrow \Lambda\omega, \Lambda\varphi$ go via K or K^*_{890} exchange, neglecting K^*_{1400} and considering forward (i.e. meson-exchange) scattering alone. If we take $\sigma(1-\rho_{oo}(\omega,\varphi))$ as a measure of the K* exchange part of the total cross-section, their ratio would be an approximate measure of that between K-K*-ω and K-K*-φ couplings. The numbers for the 6 Gev experiment are[42]:

$$\sigma_{\Lambda\omega} \text{ (vector-exchange only)} = 15\ \mu b$$

$$\sigma_{\Lambda\varphi} \quad " \quad = 14\ \mu b.$$

Obviously there is no proof of the absence of K-K*-φ coupling. If the φ is excluded from the scheme of the A-parity, the whole idea is affected since one of the main features of A-parity was an explanation of the absence of the 3π decay mode of the φ. It has been assumed, however, that the density matrix elements do provide some information about the exchange mechanisms. This may not be true. The absorption model still retains enough faith so that absorption is recognised to be able to modify

the density matrix elements considerably. It is, therefore, difficult to make any strong statements based on the values of observed density matrix elements.

Three-body final states

With the fall of the two-body cross-sections, the three-body final states appear to be the dominating process in the present experiment. It has been shown in chapter 7 that their behaviour agrees nicely with the double-peripheral model. This is what one expects intuitively from the lesson of the two-body processes. The two-body processes are dominated by s-channel poles in the low energy regions. The t-channel poles i.e. exchanged particles come into play as the c.m.energy rises to a few Gev. Any one vertex of the two-body process is still dominated by s-channel poles i.e. a stable particle or a resonance is produced at each of the two vertices. It is quite natural to assume that if the c.m.energy is raised still further, each vertex would start being dominated by exchange processes. In other words, the exchanged particle of the t-pole dominated two-body process would undergo another exchange type reaction with the incoming particle rather than forming a particle with it. This is exactly what the double-peripheral diagram represents. It is a straightforward prediction that

as the energy goes higher up, multiperipheral processes of higher orders would come into the picture. It would, however, be more difficult to assign particles to the vertices of the multiperi - pheral Feynmann diagram. With more particles, there may also be more final state interactions which would make the situation more complex.

Prospects øfor future K^-P experiments

In the field of K physics the interesting points to be pursued are the following:

1. Production mechanism of two-body processes $K^*_{890}N$ and $K^*_{1400}N$.

2. Study of the three-body states, specially the origin of the $K\pi\pi$ bump.

The only experiment done as yet at a beam momentum higher than 6 Gev is the 10 Gev experiment (ABCLV Collab.). There is a difference in the centre of mass momentum of about 1 Gev and and an 8 Gev experiment almost suggests itself. However, there are certain other advantageous features of such an experiment.

It appears that at higher energies the K*s in two-body processes are produced more cleanly i.e. with less background and less interference with N^*_{1238}. On the other hand, because

of the falling cross-sections, a much higher beam momentum would need a much larger amount of film. The three body cross-sections are expected to fall off as well and it is unwise to go to very high energies to test the double peripheral model.

One expects the $K\pi\pi$ bump to appear in this experiment fairly sharply as the background falls in relative intensity. Mass resolution should be improved as much as possible to try to separate the constituent resonances in this bump - assuming of course that to be the correct explanation.

It would be interesting to see if the L-meson appears in this experiment. With enough data it should be possible to find its J^P - although that might start a new unitary multiplet and the search for the missing members.

Quite clearly, any higher energy experiment should aim at a reasonable amount of data. Above 6 Gev the order should be 10^6 frames with $\sim$10 K s per picture and the experiment should be done in a chamber not smaller than the 150 cm. British chamber. It may, however, cease to be a multipurpose experiment in the sense that because of the strangeness exchange required, the data on hyperon production would be rather scanty.

Given enough enterprise and financial support and with a bit of good luck, the physics of $\bar{K}$-mesons probably has a long life to live.

REFERENCES

1. M.Gell Mann, Proc. Int. Conf. on High En. Phys. CERN '62

   Behrends et.al. Rev.Mod. Phys. 34, 1, '62

   Glashow and Sakurai, Nuovo Cimento 25,337,'62

2. L.M.Celnikier (Birm.-Glas.-I.C.-Oxf.-R.H.E.L. Collab.)
   - Ph.D. Thesis

3. E.Keil and W.W.Neale, CERN/TC/02 63-3.

4. Riddiford et.al., Proc. Int. Conf. on High En. accelerators and instrumentation, CERN '59

   150 cm. Hydrogen Bubble Chamber - The Engineer, 8 March '6

5. W.T.Welford, Applied Optics, 2, 981, '63.

6. E.C.Sedman, RHEL/R 111

   Burren and Sparrow, NIRL/R/14

   A.G.Wilson, NIRL/M/38

7. Berge et. al. Review of Scientific instruments 32,5,538

8. An Introduction to the theory of Statistics-
   - Yule and Kendall (pp. 497)

9. W.W.Neale, Private communication

10. Galbraith et.al. , Phys. Rev. 138, B913 , '65

11. Bondar et.al., Nuovo Cimento X, 31,485

    π^-P intns. at 10 Gev with 4 charged secondaries -
    Biswas et.al., Max-Planck Inst.,Munich.

    Cason, Ph. Rev. 148, 4, 1282

12. Jackson et.al. , Ph. Rev. 139, 2B, B428.

13. Gottfried and Jackson, Nuovo Cimento XXXIV, 3, 735

14. Jackson, Rev. Mod. Phys. 37, 3, 484

15. Phillips and Rarita, Ph. Rev. 139, 5B, B1336.

16. Roy, Nuovo Cimento, X, 40, 1212.

17. General Theoretical Situation in High Energy 2 body Reactions - L.Van Hove, CERN 66/569/5

18. J.D.Jackson, Nuovo Cimento, X, 34, 1644

19. N. Schmitz, Proc. '65 Easter School for Physicists, CERN 65 - 24

20. Astbury et. al., CERN 66/1279/5

Do. Physics Letters, 16,3,328

21. Two-body processes in K^-P interactions at 4.1 and 5.5 Gev/c - Davis et.al. (XIIIth. Int. Conf. on High En. Phys. - Berkeley '66)

22. I.C.Group, 10 Gev K^-P expt.(ABCLV Collab.) Private Communication.

23. Keyser, Prog. to calculato absorption model predictions.

24. Foley et. al. Phys. Rev. Let. 11, 503, '63.

25. J.Gordon, Phys. Let. 21, 117, '66

26. Alexander et. al., Nuovo Cimento X, 40, 839

27. M. Month, Phys. Let. 18, 357.(1.9.65)

28. R.T.Deck, Phys. Rev. Let. 13,169,'64

29. Maor and O'Halloran, Phys. Let. 15, 281, '65.

30. Fraser and Roberts, ICTP/66/18 (To be published in Nuovo Cimento)

31. Glashow and Socolow - Phys. Rev. Let. 15, 7, '65

32. D.R.O. Morrison - Phys. Let. 22, 226, '66.

33. Mesons - A.H.Rosenfeld, Oxf. Conf. on Elementary particles, 1965.

34. De Baere et. al., CERN/TC/Physics 66-19

35. Good and Walker - Phys. Rev. , 120, 1857, '60

36. Chan Hong-Mo et.al. , CERN 66/845/5 - TH.679

" CERN 66/1260/5 - TH.719

37. Bartsch et.al., Phys, Let. 22, 3, '66.

38. Boson Resonances - G. Goldhaber, XIIIth Int. Conf. on High Energy Physics, 1966, Berkeley.

39. The K*(1400) and other K* states - Schweingruber et.al., Berkeley Conf.

40. D.R.O.Morrison - Phys. Let., 22, 4, '66.

41. Bronzan and Low - Phys. Rev. Let. 12, 522, '64

42. K.Paler and L.K.Sisterson - Ph.D. Theses, (Univ. of London) '67.

43. Joseph and Pilkuhn - Nuovo Cimento, X, 33, 1407

44. Amati, Fubini and Stanghellini - Nuovo Cimento,26,896,'62.

45. Jackson and Pilkuhn - Nuovo Cimento 33, 906, '64

46. J. J.Sakurai - Proc.Int.Conf. on H.E.N.Physics, CERN '62.

ACKNOWLEDGEMENTS

It is a pleasure to thank Prof. C.C.Butler for the opportunity of carrying out research in the H.E.N.P. Group of Imperial College and Dr.S.J.Goldsack for invaluable guidance and constant interest in the present work.

I deeply appreciate the assistance and co - operation of my colleagues, specially Dr. A. W. Eskreys, Mr. K. Paler, Dr. M.Saeed and Mr. L.K.Sisterson and thank Dr. S.L.Baker for many useful discussions and criticisms.

I would like to thank Mrs.S.Hulbert and Miss A. Tomlin for their diligent housekeeping and the members of the scanning, measuring and technical staff for their indispensable contribution in this experiment.

I am grateful to the Govt. of West Bengal(India) for providing a State Scholarship during 1963-67 which made this work possible.